

Organization of chemical reactions by phase separation

Dissertation
zur Erlangung des akademischen Grades
Doctor rerum naturalium

vorgelegt

der Fakultät Physik
Bereich Mathematik und Naturwissenschaften
der Technischen Universität Dresden

von

Jonathan Bauermann
geboren am 26.12.1992
in Regensburg

erstellt am

Max-Planck-Institut für Physik komplexer Systeme
Dresden, 2022



unter der Betreuung von

Prof. Dr. Frank Jülicher

Gutachter:

Prof. Dr. Frank Jülicher

Prof. Dr. Benjamin Friedrich

Prof. Dr. Samuel Safran

Acknowledgments

First of all, I want to thank Frank Jülicher and Christoph Weber. Frank, your scientific rigor and curiosity motivated and challenged me all the time. I learned a lot in these years, and I am thoroughly grateful that you gave me the opportunity to work with you. Christoph, I thank you for countless discussions and for always bringing up creative approaches for solving problems and bringing me back to the main questions when I got lost in the details.

I thank all the former and current members of the Biological Physics community here at the Max Planck Institute for the Physics of Complex Systems. Especially the members of our weekly PhD-Seminar, namely¹ Kathrin, Christian, Omar, Giacomo, Sudarshana, Jonas, Martin, Johanna, Rabea, Felix, and Alex. Furthermore, I want to thank Joris, Charlie, Sherry, Aboutaleb, Lars, Patrick, and Stefano. I am grateful for all the discussions about science, politics, the current state of affairs, riddles, and books during lunches, hikes, and retreats. My time at the PKS would not have been the same without all of you and I always enjoyed coming to the institute. Furthermore, I thank all the people keeping this place running. Especially, I thank Hubert and Thomas from the IT department, Ulrike and Frau Richter.

I want to thank all the friends around Nolle27. Especially I thank Johannes, Tali, Ali, Nora, Rick, and Makan for always having an open door. Finally, I am deeply grateful to my parents, my siblings, Johannes and Judith, together with David, Gustav, and Lasse. Lena, I count myself very lucky that you have walked the last years with me.

¹Ordered by the physical distance between their desks and mine.

Abstract

All living things are driven by chemical reactions. Reactions provide energy and transform matter. Thus, maintaining the system out of equilibrium. However, these chemical reactions have to be organized in space. One way for this spatial organization is via the process of phase separation. Motivated by the recent discovery of liquid-like droplets in cells, this thesis studies the organization of chemical reactions in phase-separated systems, with and without broken detailed balance.

After introducing the underlying thermodynamic principles, we generalize mass-action kinetics to systems with homogeneous compartments formed by phase separation. Here, we discuss the constraints resulting from phase equilibrium on chemical reactions. We study the relaxation kinetics towards thermodynamic equilibrium and investigate non-equilibrium states that arise when detailed balance is broken in the rates of reactions such that phase and chemical equilibria contradict each other. We then turn to spatially continuous systems with spatial gradients within formed compartments. We derive thermodynamic consistent dynamical equations for reactions and diffusion processes in such systems. Again, we study the relaxation kinetics towards equilibrium and discuss non-equilibrium states. We investigate the dynamics of droplets in the presence of reactions with broken detailed balance. Furthermore, we introduce active droplet systems maintained away from equilibrium via a coupling to reservoirs at their boundaries and organizing reactions solely within droplets. Here, detailed balance is only broken at the boundaries. Nevertheless, stationary chemically active droplets exist in open systems, and droplets can divide.

To quantitatively study chemically active droplet systems in multi-component mixtures, we introduce an effective description. Therefore, we couple linearized reaction-diffusion equations via a moving interface within a sharp interface limit. At the interface, the boundary conditions are set by a local phase equilibrium and the continuity of fluxes.

Equipped with these tools, we introduce and study protocell models of chemically active droplets. We explicitly model these protocells' nutrient and waste dynamics, leading to simple models of their metabolism. Next, we study the energetics of these droplets and identify processes responsible for growth or shrinkage and maintaining the system out of equilibrium. Furthermore, we discuss the energy balance leading to the heating and cooling of droplets.

Finally, we show why chemically active droplets do not spontaneously divide in two-dimensional systems with bulk-driven reactions. Here, droplets can elongate but do not pinch off. To have a minimal two-dimensional model with droplet division, we introduce additional reactions. When these reactions are localized at the interface and dependent on its mean curvature, droplets robustly divide in 2D.

In summary, this thesis contributes to the theoretical understanding of how the existence of droplets changes the kinetics of reactions and, vice versa, how chemical reactions can alter droplet dynamics.

Zusammenfassung

Alle Lebewesen sind angetrieben von chemischen Reaktionen, die Energie liefern und Materie umwandeln können, wodurch diese Systeme aus dem Gleichgewicht gehalten werden. Diese chemischen Reaktionen müssen jedoch räumlich organisiert sein. Eine Möglichkeit räumlicher Organisation ist der Prozess der Phasentrennung. Angeregt durch die jüngste Entdeckung flüssiger Tröpfchen in Zellen untersucht diese Arbeit die Organisation chemischer Reaktionen in phasentrennten Systemen mit und ohne gebrochener detaillierter Bilanz.

Nach der Einführung der zugrunde liegenden thermodynamischen Prinzipien verallgemeinern wir die Massenwirkungskinetik auf Systeme mit, durch Phasentrennung gebildeten, homogenen Kompartimenten. Hier diskutieren wir die aus dem Phasengleichgewicht resultierende Einschränkung für chemische Reaktionen. Anschließend untersuchen wir die Relaxationskinetik hin zu dem thermodynamischen Gleichgewicht. Darüber hinaus untersuchen wir stationäre Nichtgleichgewichtszustände. Diese entstehen, wenn die detaillierte Bilanz in den Raten der Reaktionen derartig gebrochen sind, sodass Phasengleichgewicht und das Gleichgewicht chemischer Reaktion zueinander im Widerspruch stehen.

Anschließend wenden wir uns räumlich kontinuierlichen Systemen zu, in welchen Gradienten auch innerhalb der Kompartimente existieren können. Wir leiten thermodynamisch konsistente dynamische Gleichungen für die Reaktionen- und Diffusionsprozesse in solchen Systemen her. Erneut untersuchen wir die Relaxationskinetik in Richtung des Gleichgewichts und diskutieren Nichtgleichgewichtszustände und die Dynamik von Tröpfchen in Gegenwart von Reaktionen mit gebrochener detaillierter Bilanz. Darüber hinaus führen wir aktive Tropfensysteme ein, die durch eine Kopplung an Reservoirs an ihren Systemgrenzen aus dem Gleichgewicht gehalten werden und bei denen Reaktionen nur innerhalb der Tröpfchen geschehen. Obwohl hier die detaillierte Bilanz nur an den Systemgrenzen gebrochen ist, gibt es dennoch stationäre chemisch aktive Tröpfchen in offenen Systemen und Tröpfchen können sich teilen.

Um aktive Tropfensysteme in Mehrkomponentenmischungen quantitativ untersuchen, zu können führen wir eine effektive Beschreibung ein. Unter der Annahme einer unendlich scharfen Grenzfläche kann die Dynamik derartiger Systeme approximiert werden. Anstelle der nichtlinearen Differentialgleichungen, werden in den jeweiligen Phasen linearisierte Reaktions-Diffusionsgleichungen über eine bewegliche Grenzfläche gekoppelt. Die Randbedingungen dieser Grenzfläche sind festgelegt durch ein lokales Phasengleichgewicht und die Kontinuität der Ströme.

Mit Hilfe dieser Konzepte, führen wir ein Protozellmodell von chemisch aktiven

Tropfen ein. Wir modellieren explizit die Nährstoff- und Abfalldynamik dieser Protoplasten, was zu einfachen Modellen ihres Metabolismus führt. Anschließend untersuchen wir die Energetik dieser Tröpfchen und identifizieren Prozesse, die verantwortlich für Wachstum oder Schrumpfung und die Aufrechterhaltung des Nichtgleichgewichtszustandes sind. Schließlich erörtern wir die Energiebilanz, die Aufschluss über das Erwärmen oder die Abkühlung dieser Tropfen gibt.

Abschließend erörtern wir, warum sich aktive Tröpfchen, getrieben von Nichtgleichgewichtsreaktionen, in zweidimensionalen Systemen nicht spontan teilen. Sie können sich ausdehnen und verformen, aber es kommt zu keiner Teilung. Um ein minimales zweidimensionales Modell zu haben, das die Teilung von Tröpfchen zeigt, führen wir zusätzliche chemische Reaktionen ein. Wenn diese Reaktionen an der Tropfengrenzfläche lokalisiert sind und von dessen mittleren Krümmung abhängen, teilen sich die Tröpfchen robust in 2D.

In ihrer Gesamtheit trägt diese Arbeit zum theoretischen Verständnis der Frage bei, wie die Existenz von Tröpfchen die Reaktionskinetik verändern kann und umgekehrt, wie chemische Reaktionen die Tröpfchendynamik beeinflussen.

Contents

1	Introduction	1
1.1	Thermodynamics of phase separation	2
1.1.1	Phase equilibrium in the thermodynamic limit	3
1.1.2	Relaxation dynamics towards equilibrium	6
1.1.3	Local stability of homogeneous phases	7
1.2	Thermodynamics of chemical reactions in homogenous mixtures . . .	9
1.2.1	Conserved densities and reaction extents	9
1.2.2	Equilibrium of chemical reactions	11
1.2.3	Mass-action kinetics towards equilibrium	12
1.3	Simultaneous equilibrium of chemical reactions and phase separation	14
1.4	Chemical reactions maintained away from equilibrium	18
1.5	Structure of this thesis	19
2	Chemical reactions in compartmentalized systems	21
2.1	Mass-action kinetics for compartments built by phase separation . . .	21
2.1.1	Dynamical equations for densities and phase volumes	22
2.1.2	Relaxation kinetics in a simple example	24
2.2	Driven chemical reactions in compartmentalized systems	26
2.2.1	Non-equilibrium steady states at phase equilibrium	27
2.2.2	The tie line selecting manifold	28
2.3	Discussion	30
3	Dynamics of concentration fields in phase-separating systems with chemical reactions	31
3.1	Reaction-diffusion equations for phase separating systems	32
3.2	Relaxation towards thermodynamic equilibrium in spatial systems . .	33
3.2.1	Relaxation kinetics and fast diffusion	33
3.2.2	Relaxation kinetics with spatial gradients	35
3.3	Driven chemical reactions in phase-separating systems	37
3.3.1	Driven chemical reaction and fast diffusion	38
3.3.2	Non-equilibrium steady states and spatial gradients	39
3.3.3	Droplets growth and ripening with driven chemical reactions .	41
3.4	Boundary driven chemically active droplets	47
3.4.1	Droplets in open systems	48

3.4.2	Non-equilibrium steady droplets and shape instabilities	48
3.5	Discussion	51
4	Chemically active droplets in the sharp interface limit	53
4.1	Droplet dynamics via reaction-diffusion equations coupled by a moving interface	53
4.2	Stationary interface positions in spherical symmetry	54
4.2.1	Interface conditions in closed systems	55
4.2.2	Interface conditions in open systems	58
4.3	Shape instabilities of spherical droplets	64
4.4	Discussion	67
5	Models of protocells and their metabolism as chemically active droplets	68
5.1	Breaking detailed balance in protocell models	68
5.1.1	Boundary driven protocell models	69
5.1.2	Bulk driven protocell models	69
5.2	Protocell dynamics	70
5.2.1	Steady states droplets	70
5.2.2	Shape stability of spherical symmetric droplets	73
5.3	Energetics of protocells	74
5.3.1	Mass conservation and droplet growth or shrinkage	74
5.3.2	Energy conservation and droplet heating or cooling	75
5.4	Discussion	77
6	The role of dimensionality on droplet division	79
6.1	Stability of chemically active droplets in 2D vs. 3D	80
6.1.1	Stationary droplets in 1D, 2D and 3D	82
6.1.2	Elongation instability	83
6.1.3	Pinch-off instability	85
6.2	Pinch-off in 2D via curvature-dependent chemical reactions	88
6.2.1	Determining the mean curvature of the droplet interface	88
6.2.2	Chemical reactions at the interface	89
6.3	Discussion	91
7	Conclusion and Outlook	93
A	Free energy considerations	97
B	Surface tension in multi-component mixtures	98
C	Figure details	102
	Bibliography	107

Chapter 1

Introduction

The discovery of liquid-like droplets in cells [1] has nucleated a fast-growing field of biological research [2, 3]. Now, the existence of droplets, mainly formed by proteins, inside the cytoplasm has been reported in many different studies. For a review, see [4]. These droplets form membrane-less organelles and can structure the cytoplasm. However, a key challenge up to now is to identify the full functional consequence of droplets and their distinct biological relevance [5, 6]. One of the proposed functions of these condensates is to structure and localize chemical reactions inside cells [5, 7]. From a statistical physics point of view, the interplay of chemical reactions and phase separation in active environments like cells is an interesting question on its own. However, systems with chemical reactions and phase separation are much less studied than chemical reactions in homogeneous or spatially continuous systems with diffusion following Fick's law. In the first case, the time evolution of concentrations follows classical mass-action dynamics, and non-equilibrium steady states can occur when detailed balance is broken, see [8, 9]. The second case is usually studied within the framework of reaction-diffusion equations, see, e.g., [9, 10]. Here, interesting patterns can emerge from the interplay of active chemical reactions and spatial transport via classical diffusion [11]. Another example of these spatial systems with active chemical reactions is the so-called Model A in the classification of Hohenberg and Halperin [12]. Here, the time evolution of the concentration field is given by the so-called Allen-Cahn equation [13, 14].

Phase separation dynamics is mainly studied theoretically in binary mixtures. The typical example is the so-called Model B in the same classification of Hohenberg and Halperin [12]. Here, the dynamical equation of the concentration field of one of the components follows the so-called Cahn-Hilliard equation [15, 14].

As mentioned above, the interplay of phase separation and chemical reactions is much less studied. Chemical active droplets had been studied conceptionally, without a direct link to the driving free energy, already 90 years ago [16, 17]. Only recently, active chemically reactions in spatial models of binary mixtures have been studied by [18, 19, 20]. In most of these studies, however, the chemical reactions are considered far from equilibrium, in the sense that the chemical reaction rates are not connected to the free energy that drives phase separation. This thesis starts from

equilibrium considerations of multi-component phase-separating mixtures and makes the breaking of detailed balance explicit, thus driving the system out of equilibrium. In spatially organized systems, the driving of chemical reactions in the bulk or the breaking of detailed balance at the system boundaries can lead to droplet dynamics not observed in equilibrium situations.

In this introduction, we introduce all concepts of phase separation and chemical reactions in equilibrium systems that are used in this work and give a short review of how systems are usually made active via driven chemical reactions. At the end of this introduction, we will briefly outline the goals and structure of this thesis.

1.1 Thermodynamics of phase separation

Phase separation occurs in mixtures of at least two non-dilute components when molecules interact. Instead of homogeneous, well-mixed states, these systems demix and build phases of different compositions. Arguably, the most common example is the spontaneous demixing of oil and water. The interactions between hydrophobic oil molecules and water lead to the formation of droplets. However, this phenomenon is general and occurs in many different circumstances [21].

In this work, we focus on phase separation in incompressible fluids. To describe the composition of a mixture with several components $i = 0, \dots, M$, we define the volume fractions $\phi_i = \nu_i N_i / V$. Here, ν_i is the mean volume occupied by one molecule of species i , called molecular volume in the following, N_i is the number of molecules of species i , and V is the system volume. Furthermore, we can express the volume fraction of one component in terms of all others. We write $\phi_0 = 1 - \sum_{i=1}^M \phi_i$ and call this component solvent S in the following. In this thesis, we will use mean-field theories. The main assumption is that we can define useful mean values of ϕ_i in local volumes. Instead of summing over all possible microscopical states, and deriving the free energy from the partition function, we assume, therefore, an effective free energy

$$F(\{\phi_i\}) = \int dV \left[f(\{\phi_i\}) + \sum_{i=0}^M \frac{\kappa_i}{2\nu_i} (\nabla\phi_i)^2 \right] , \quad (1.1)$$

for the total system. For a more detailed discussion about the mean-field assumption, see, e.g., [22, 23]. The terms proportional to $(\nabla\phi_i)^2$ are equivalent to the density gradient term¹ introduced already 1873 by van der Waals (see [24] for an English translation and a more detailed discussion) and put in their modern form by Cahn and Hilliard [15]. These terms penalize spatial gradients and ensure smooth changes of ϕ_i between different local volumes, even when the system phase separates. However, the free energy density has to have non-convex regions for phase separation to occur. In the literature, the most common example is the Ginzburg-Landau free energy density for binary mixtures, see, e.g., [25]. Here, combining a

¹Here, we neglect terms of the form $|\nabla\phi_i \nabla\phi_j|$ which are of the same order but do not change the effects qualitatively.

quadratic term and a biquadratic term generates a concave interval in the free energy density. However, in the main² part of this thesis, we will use versions of the so-called Flory-Huggins free energy density [26, 27]. For the latter, the ideal limit of non-interacting particles becomes simple and it can be easily generalized for multi-component mixtures.

Given a free energy such as Eq. 1.1, we can define, via the functional derivative, the exchange chemical potential as $\bar{\mu}_i = \nu_i \delta F / \delta \phi_i$, for $i = 1, \dots, M$. Due to incompressibility, changing the particle number N_i but keeping the volume constant is only possible by exchanging particles. As a convention, we always exchange with solvent particles³. We can write these exchange chemical potentials as

$$\bar{\mu}_i = k_B T \log(\bar{\gamma}_i \phi_i) + \bar{\omega}_i - \kappa_i \nabla^2 \phi_i \quad , \quad (1.2)$$

where $\bar{\gamma}_i$ is the exchange activity coefficient and $\bar{\gamma}_i \phi_i$ the exchange activity. Furthermore, we have introduced composition-independent reference chemical potentials $\bar{\omega}_i$ of exchanges, the Boltzmann constant k_B and the system temperature T . For mean-field models up to the second virial coefficients, the exchange activity coefficient has the form

$$\bar{\gamma}_i = \frac{1}{\phi_0} \exp \left(\nu_i \frac{\sum_{j=1}^M (\chi_{ij} - \chi_{i0} - \chi_{j0}) \phi_j}{k_B T} \right) \quad , \quad (1.3)$$

where χ_{ij} are the so-called Flory-Huggins interaction parameters. These parameters result from the molecular interactions between the components. Without loss of generality, only $M(M+1)/2$ interaction parameters χ_{ij} can be chosen independently. Thus, we can represent them in a symmetric matrix with $\chi_{ii} = 0$. Other choices can always be rewritten into this form. This also shows that the specific energetic cost of molecular interactions between components (in total, there can be $(M+1)(M+2)/2$ different pairs of interactions) cannot be inferred fully from the interaction parameters. These specifics have been lost during the process of coarse-graining.

1.1.1 Phase equilibrium in the thermodynamic limit

To perform the thermodynamic limit, we make the system size V large while keeping the mean volume fractions $\bar{\phi}_i = \nu_i N_i / V$ constant. Therefore, we can expand the total free energy of the system into bulk contributions, scaling with the system volume, and surface contributions, scaling with the surface area A of the system. We write

$$F = f_b V + \gamma A + \mathcal{O}(L^{d-2}) \quad , \quad (1.4)$$

where d is the dimensionality of the system, γ the surface tension, A the surface area of the system, and L is the system size, thus $L \propto V^{1/d}$. The bulk free energy density f_b is defined via $f_b = \lim_{V \rightarrow \infty} F/V$. For a system of two coexisting phases, we split

²Except Section 6.1. There, we use to the Ginzburg-Landau free energy.

³The exchange chemical potentials are related to the chemical potential in the compressible case via $\bar{\mu}_i = \mu_i - \nu_i / \nu_0 \mu_0$.

this free energy density into two contributions coming from the two homogeneous phases and write

$$f_b = \frac{V^I}{V} f^I + \frac{V^{II}}{V} f^{II} \quad , \quad (1.5)$$

where we introduced the phase volumes $V^{I/II}$. The gradient terms in Eq. 1.1 do not contribute to the bulk free energy when L becomes large compared to the length scales over which gradients occur in the system. Therefore, we can assume $f^{I/II} = f(\{\phi_i^{I/II}\})$, with f being the free energy density from Eq. 1.1. However, these gradient terms are relevant for the interface between the two phases. The surface free energy, also called surface tension in liquids, is defined by $\gamma = \lim_{A \rightarrow \infty} (F - f_B V) / A$. In addition to the system boundaries, the interphase between the phases also gives rise to surface contributions of the free energy for phase separating systems. A more detailed discussion about the connection between the gradient terms in Eq. 1.1 and the surface tension is given in App. B. A more detailed discussion about the thermodynamic limit, in general, can be found in [28].

The minimum of the free energy defines the phase equilibrium for finite systems with system size V . This minimization, however, is constrained. First, the conservation of particles requires $V \bar{\phi}_i = V^I \phi_i^I + V^{II} \phi_i^{II}$, for every component $i = 1, \dots, M$. Second, the phase volumes build up the system volume, thus $V = V^I + V^{II}$. These constraints reduce the $2M + 2$ variables in Eq. 1.5, $\phi_i^{I/II}$ for $i = 1, \dots, M$ and $V^{I/II}$, to only $M + 1$ degrees of freedom. Furthermore, we assume spherical droplets with radius R of phase I in 3D and neglect surface contributions from the systems boundaries. Knowing the average volume fractions $\bar{\phi}_i$ in a system, we can derive the $2M$ volume fractions for the minimum of F by solving ⁴:

$$\begin{aligned} & \bullet \text{ chem. pot. balance between phases: } \bar{\mu}_i^I = \bar{\mu}_i^{II}, & M \\ & \bullet \text{ pressure condition: } f^I - f^{II} = \sum_{i=1}^M \frac{\bar{\mu}_i^{I/II}}{\nu_i} (\phi_i^I - \phi_i^{II}) - \frac{2\gamma}{R}, & 1 \\ & \bullet \text{ conservation laws: } \frac{\bar{\phi}_i - \phi_i^{II}}{\phi_i^I - \phi_i^{II}} = \frac{\bar{\phi}_j - \phi_j^{II}}{\phi_j^I - \phi_j^{II}}, \quad i, j = 1, \dots, M & M - 1 \\ & & \frac{2M}{(1.6)} \end{aligned}$$

where we named the constraints on the left hand side and count the number of independent equations on the right hand side. Furthermore, we have defined the

⁴ **Minimization of the free energy:**

We consider ϕ_i^I for $i = 1, \dots, M$, and V^I as independent degrees of freedom. Using the constraints, we can express

$$V^{II} = V - V^I, \quad \phi_i^{II} = \frac{V \bar{\phi}_i - V^I \phi_i^I}{V - V^I}$$

and find

$$\frac{\partial V^{II}}{\partial \phi_i^I} = 0, \quad \frac{\partial V^{II}}{\partial V^I} = -1, \quad \frac{\partial \phi_i^{II}}{\partial \phi_j^I} = -\frac{V^I}{V^{II}} \delta_{ij}, \quad \frac{\partial \phi_i^{II}}{\partial V^I} = \frac{\phi_i^{II} - \phi_i^I}{V^{II}} \quad .$$

bulk exchange chemical potentials⁵ $\bar{\mu}_i^{I/\Pi} = \nu_i \partial f(\{\phi_i^{I/\Pi}\}) / \partial \phi_i$.

The first $M + 1$ constraints follow from the minimization⁴ of F . The remaining $M - 1$ conservation laws follow directly when considering

$$\frac{V^I}{V} = \frac{\bar{\phi}_i - \phi_i^\Pi}{\phi_i^I - \phi_i^\Pi} \quad , \quad (1.7)$$

and $V^\Pi/V = 1 - V^I/V$. In the thermodynamic limit, the system size goes to infinity, but these relative phase volumes are well defined. Furthermore, the droplet radius R diverges, and the surface contribution becomes negligible compared to the bulk contribution. We find that phase equilibrium is independent of the reference chemical potentials ω_i . These terms stem from linear contributions proportional to $\omega_i \phi_i$ in f . The structure of Eq. 1.6 is such that all these terms cancel.

For a binary system ($M = 1$), the composition is defined by just one volume fraction ϕ . In the thermodynamic limit, the condition of phase equilibrium, stated in Eq. 1.6, can be geometrically understood as finding two volume fractions $\phi^{I/\Pi}$ (red dots in FIG. 1.1(a)), where $f(\phi^{I/\Pi})$ has the same tangent (black line in FIG. 1.1(a)). This is known as the "common tangent" construction. Therefore, the bulk exchange chemical potentials $\bar{\mu}^{I/\Pi}$ are identical (red dots in FIG. 1.1(b)). For finite systems, the interface contribution leads to deviations. The equilibrium volume fractions $\phi^{I/\Pi}$ (orange dots in FIG. 1.1(a)), do not have the same tangent, but an offset $\propto 2\gamma/R$ between them (grey lines in FIG. 1.1(a)). The bulk exchange chemical potentials $\bar{\mu}^{I/\Pi}$ are still the same (orange dots in FIG. 1.1(b)).

In the binary case ($M = 1$), however, the equilibrium volume fractions $\phi^{I/\Pi}$ are unique in the sense that they are independent of the average volume fraction $\bar{\phi}$ in the thermodynamic limit. Here, already the first two conditions of Eq. 1.6 are sufficient to define these values. As a result, all systems with $\bar{\phi}$ values which lie within the phase separating area have the same equilibrium volume fractions $\phi^{I/\Pi}$. Only the relative phase volumes $V^{I/\Pi}/V$ differ between these systems.

For all systems with $M > 1$, the equilibrium volume fractions $\phi_i^{I/\Pi}$ depend on $\bar{\phi}_i$.

From the assumption of a spherical droplets of phase I, we conclude

$$\frac{\partial A}{\partial \phi_i^I} = 0, \quad \frac{\partial A}{\partial V^I} = \frac{2}{R} \quad .$$

Therefore, we can express the free energy in Eq. 1.4 as $F(\{\phi_i^I\}, V^I) = V^I f^I + V^\Pi f^\Pi + \gamma A$, thus its minimum reads

$$\frac{\partial F}{\partial \phi_i^I} = 0 \quad \Rightarrow \quad \frac{\partial f^I}{\partial \phi_i^I} = \frac{\partial f^\Pi}{\partial \phi_i^\Pi} \quad ,$$

for $i = 1, \dots, M$ and

$$\frac{\partial F}{\partial V^I} = 0 \quad \Rightarrow \quad f^I - f^\Pi = \frac{\partial f^\Pi}{\partial \phi_i^\Pi} (\phi_i^I - \phi_i^\Pi) - \frac{2\gamma}{R} \quad ,$$

where we have used chain rules and the aforementioned partial derivatives. The first constraints balance the exchange chemical potentials between the phases, while the last constraint balances the so-called osmotic pressures $\Pi^{I/\Pi} = -\partial F / \partial V^{I/\Pi}$ and the additional Laplace pressure coming from the interface between the phases.

⁵In the following, we do not distinguish strictly between the bulk exchange chemical potentials and the exchange chemical potentials defined in Eq. 1.2. Whenever spatial systems with fields of volume fractions are considered, we refer to Eq. 1.2, while in systems of homogeneous phases, we refer to the bulk exchange chemical potentials defined here.

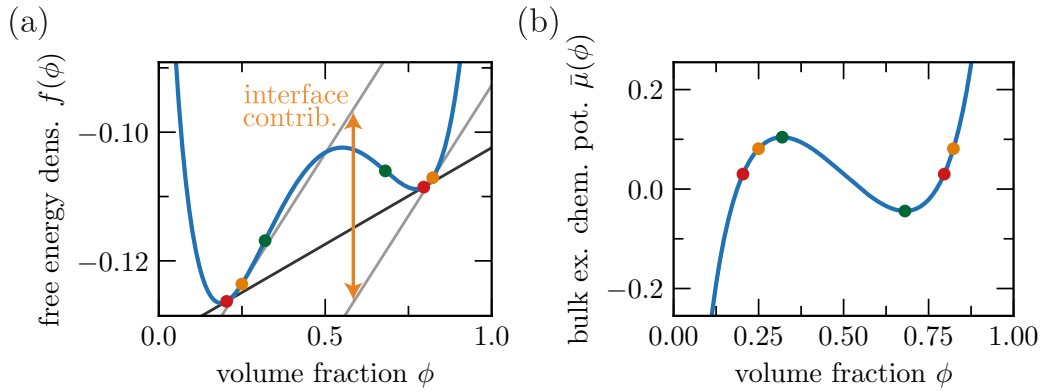


FIGURE 1.1: "**Common tangent**" construction for a binary ($M=1$) mixture: An exemplary free energy density of a binary mixture (a), and the corresponding exchange chemical potential $\bar{\mu}$ (b) as a function of ϕ are shown. The equilibrium values in the thermodynamic limit (red dots) are defined by the common tangent (black line in (a)), while the tangents at the equilibrium values in finite systems have an identical slope but are shifted due to the Laplace pressure (grey lines in (a)). The spinodal points (see Section 1.1.3) are indicated with green dots. For the specific parameters, see App. C.

In FIG. 1.3(a) we show the phase diagram of a ternary mixture with molecules of type A , B , and the solvent S . It shows the equilibrium volume fractions in the composition space. All systems with average compositions $\bar{\phi}_B$ and $\bar{\phi}_A$ lying within the binodal (thick green line) phase separate. The equilibrium volume fractions $\phi_i^{I/II}$ lie at the end of the corresponding tie lines (thin green lines). These tie lines are the graphical representation of the conservation laws in Eq. 1.6. Furthermore, the ratio of the phase volumes V^I/V^{II} can be identified by the ratio of the distance from $\bar{\phi}_i$ to ϕ_i^{II} and the distance from $\bar{\phi}_i$ to ϕ_i^I along the tie lines, see, e.g., [29].

The equilibrium values for finite and infinite systems, determined in this section, are reached far away from the interface connecting the two phases. In general, it is not possible to derive the spatial profiles that correspond to the minimum of Eq. 1.1. For further discussion, see App. B.

1.1.2 Relaxation dynamics towards equilibrium

In the previous section, we studied the equilibrium values for large systems and minimized the expanded free energy F given in Eq. 1.4. To derive the dynamics of the volume fractions fields, we minimize the free energy given in Eq. 1.1 directly. Locally, the conservation of material has to hold, and we can use the continuity equation

$$\partial_t \phi_i = -\nabla \cdot \mathbf{j}_i \quad , \quad (1.8)$$

where \mathbf{j}_i is the diffusive flux density of volume fraction. In linear theory, we can assume

$$\mathbf{j}_i = -\nu_i \sum_{j=1}^M \Gamma_{ij} \nabla \bar{\mu}_j \quad , \quad (1.9)$$

where Γ_{ij} are the mobility coefficients. In this work, we choose, whenever nothing else is specified, a non-diagonal mobility matrix

$$\Gamma_{ij} = \Gamma\phi_i(\delta_{ij} - \phi_j) \quad , \quad (1.10)$$

where Γ can be related to an exchange rate of particles. This choice of the mobility matrix is motivated by the fact that the diffusion matrix, defined by

$$D_{ij} = \nu_i \sum_{k=1}^M \Gamma_{ik} \frac{\partial \bar{\mu}_k}{\partial \phi_j} \quad , \quad (1.11)$$

becomes diagonal $D_{ij} = \nu_i k_B T \gamma \delta_{ij}$ in the absence of molecular interactions⁶ and all molecular volumes being equal. With this, we restore Fick's law of diffusion (see Appendix of [30, 31]).

In general, Eq. 1.8 is a non-linear fourth-order partial differential equation. In the special case of a binary mixture and a Ginzburg-Landau free energy density, this equation simplifies to linear fourth-order terms and non-linear quadratic terms. Under these circumstances it is known as Cahn-Hilliard equation [15, 32].

1.1.3 Local stability of homogeneous phases

Even when the system has average volume fractions corresponding to a phase-separated equilibrium situation, the system does not necessarily spontaneously demix [33]. In this section, we study the stability of homogeneous states. Therefore, we linearise the dynamics of Eq. 1.8 around the homogeneous state $\hat{\phi}_i$ of interest and study the relaxation of small perturbations $\delta\phi_i$. The linearized dynamics follow

$$\partial_t \delta\phi_i = \sum_{j=1}^M (\hat{D}_{ij} - \hat{\Gamma}_{ij} \nabla^2) \nabla^2 \delta\phi_j \quad , \quad (1.12)$$

where we use the diffusion coefficients $\hat{D}_{ij} = D_{ij}(\{\hat{\phi}_i\})$ as defined in Eq. 1.11 and evaluated at $\hat{\phi}_i$, and $\hat{\Gamma}_{ij} = \nu_i \kappa_j \Gamma_{ij}(\{\hat{\phi}_i\})$. To study the stability of small perturbations, we use periodic functions

$$\delta\phi_j = \epsilon_j \exp(\tau t + i q x) \quad , \quad (1.13)$$

⁶In the absence of molecular interactions, the volume fractions fields become more and more homogeneous and the gradient terms proportional to κ_i in Eq. 1.1 become negligible.

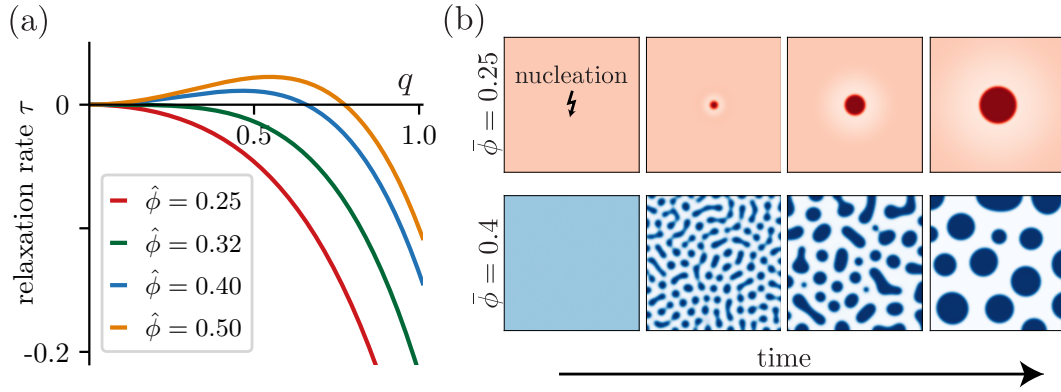


FIGURE 1.2: **Nucleation-and-growth regime vs. spinodal decomposition:** (a): The relaxation rates τ as functions of the perturbation wavelength q are shown at four different homogeneous volume fraction values $\bar{\phi}$. (b): Snapshots of the volume fraction fields in 2D systems over time are shown, in the upper row, a system in the nucleation-and-growth regime, of locally stable homogeneous mixtures, in the lower row in the spinodal regime. The chosen colormaps for the two examples match the corresponding color of the stability analysis in (a) with same average composition. For details and parameters, see App. C.

with wavenumber q , and relaxation time τ . Here, i is the imaginary unit, and ϵ_j are the perturbation amplitudes. These amplitudes have to be necessarily component-specific coefficients, for solving the non-diagonal problem. We can derive the dispersion relations⁷ $\tau_k(q)$ in linear response. They are obtained by solving the M equations

$$\tau \epsilon_i = -q^2 \sum_{j=1}^M (\hat{D}_{ij} \epsilon_j + \hat{\Gamma}_{ij} \epsilon_j q^2) \quad , \quad (1.14)$$

simultaneously for $\epsilon_j, j = 2, \dots, M$ and τ . Due to the scaling of the overall amplitude, we can always assume $\epsilon_1 = \text{const.}$ without loss of generality. Therefore, choosing a perturbation with a specific wavenumber q determines the relaxation rates τ_k 's. Whenever such a perturbation has one $\tau_k > 0$, this perturbation is unstable and will grow exponentially. Hence the mixture demixes. This instability is called spinodal decomposition. Whenever all $\tau_k < 0$, only large perturbations can trigger phase separation. In this regime, droplets grow after being nucleated larger than a critical radius. This critical radius can be defined as

$$R_{crit} = \frac{2\gamma}{f^I - f^{II} - \sum_{i=1}^M \frac{\mu_i}{\nu_i} (\phi_i^I - \phi_i^{II})} \quad , \quad (1.15)$$

by inverting the pressure condition of Eq. 1.6 [34]. The manifold in composition space which splits these two regimes is called spinodal and always lies within the binodal area. Only at the critical point, it touches the binodal (see for example FIG. 3.1(a)). For binary mixtures, we obtain just two volume fractions at which the stability changes. The green dots in FIG. 1.1 depict these points for the free energy chosen in this example. We show the dispersion relation of the same system in FIG. 1.2(a). The instability occurs at $\bar{\phi} \approx 0.32$ (green line). This value is the inflection

⁷For multi-component mixtures, we obtain degenerated solutions, thus several τ 's for one q

point of the free energy in FIG. 1.1(a). In general, the stability can also be determined directly by the curvature of the free energy density [34, 22]. Furthermore, we show snapshots in time of numerical simulations with homogeneous initial conditions of average composition $\bar{\phi} = 0.25$ (blue) and $\bar{\phi} = 0.4$ (red) in FIG. 1.1(b). As predicted from the dispersion relation shown in FIG. 1.2(a) (in the corresponding colors), phase separation occurs only after a nucleation event in the first case. In the second case, the mixture spontaneously demixes. After the spinodal decomposition, however, big droplets grow at the cost of small ones. This process is called Ostwald ripening [35].

1.2 Thermodynamics of chemical reactions in homogenous mixtures

While phase separation minimizes the free energy by organizing particles in space, chemical reactions minimize the free energy by converting particles of different types into each other. In general, chemical reactions can be written in the form

$$\sum_{i=0}^M \sigma_{i\alpha}^+ C_i \rightleftharpoons \sum_{i=0}^M \sigma_{i\alpha}^- C_i \quad , \quad (1.16)$$

where the $\sigma_{i\alpha}^\pm$ are stoichiometric coefficients, and C_i denote the chemical species, see [36, 37]. The stoichiometric coefficients $\sigma_{i\alpha}^\pm$ indicate how many particles of species i are degraded (reactants: +) or produced (products: -) when the chemical reaction α runs from the left to the right side. These coefficients define the so-called stoichiometric matrix

$$\sigma_{i\alpha} = \sigma_{i\alpha}^- - \sigma_{i\alpha}^+ \quad , \quad (1.17)$$

which represents therefore a specific reaction scheme of multiple reactions $\alpha = 1, \dots, L$. In this work, we restrict ourself to incompressible mixtures. Therefore, only volume conserving chemical reactions, fulfilling

$$\sum_{i=0}^M \sigma_{i\alpha} \nu_i = 0 \quad , \quad (1.18)$$

can occur. Otherwise, the system becomes compressible due to the fact, that it can shrink in size via a change in composition when pressure is applied to the system.

1.2.1 Conserved densities and reaction extents

The volume fractions ϕ_i are not conserved individually, due the chemical reactions. In general, there are $L' \leq M$ linearly independent chemical reactions. Therefore, there remain $C = M - L'$ conserved densities in addition to the conserved volume,

see for example [38, 39]. These conserved densities can be expressed as linear combination of volume fractions. We write the conserved densities as

$$\psi_j = \sum_{i=0}^M A_{ji} \phi_i \quad , \quad (1.19)$$

where $j = 0, 1, \dots, C$. Here, the matrix A obeys the relation $\sum_{i=0}^M A_{ji} \nu_i \sigma_{i\alpha} = 0$, i. e. the rows of the matrix A are linearly independent null-vectors of the matrix $\nu_i \sigma_{i\alpha}$. The conservation law Eq. 1.18 corresponds to $j = 0$ with $A_{0i} = 1/\nu_0$, which also clarifies that units of ψ_j is inverse volume⁸. We can also define the $L' = M - C$ non-conserved densities

$$\xi_\alpha = \sum_{i=1}^M B_{\alpha i} \phi_i \quad , \quad (1.20)$$

where $\alpha = 1, \dots, L'$, which are the reaction extents. These ξ_α measure the cumulative number of reaction events that have occurred per volume. While the conserved densities stay constant in time, in homogeneous mixtures the densities of the reaction extents are the only dynamical variables. For the matrix B , we use the pseudo-inverse of the volumetric stoichiometric matrix $\nu_i \sigma_{i\alpha}$. Explicitly, the matrices A and B define the matrix elements of an invertible square matrix

$$U = \begin{pmatrix} A_{00} & \cdots & A_{0i} & \cdots & A_{0M} \\ & & \cdots & A_{ji} & \cdots \\ A_{C0} & \cdots & A_{Ci} & \cdots & A_{CM} \\ B_{1i} & \cdots & B_{1i} & \cdots & B_{1M} \\ & & \cdots & B_{\alpha i} & \cdots \\ B_{L'0} & \cdots & B_{L'i} & \cdots & B_{L'M} \end{pmatrix} \quad . \quad (1.21)$$

A property of the inverse matrix U^{-1} is $U_{i\alpha}^{-1} = \nu_i \sigma_{i\alpha}$. The matrix A and the conserved densities ψ_j are not unique. Indeed, any linear combination of conserved densities is also a conserved density. A choice of linearly independent conserved densities specifies the matrix A uniquely. Similarly, the matrix B is also not unique, because each reaction extent is defined with respect to a reference value.

From the conserved densities ψ_j and the reaction extents ξ_α , we can obtain the volume fractions as

$$\phi_i = \sum_{j=0}^C U_{ij}^{-1} \psi_j + \sum_{\alpha=1}^{L'} \nu_i \sigma_{i\alpha} \xi_\alpha \quad . \quad (1.22)$$

To illustrate this, we consider, for example, a quaternary ($M = 3$) mixture of components A, B, C , and the solvent S . Their molecular volumes follow $\nu_S = \nu_A$, $\nu_B = 2\nu_A$ and $\nu_C = 6\nu_A$. Furthermore, the chemical reactions $2A + B \rightleftharpoons C$ ($\alpha = 1$) and $4A \rightleftharpoons B$

⁸For simplicity, we will suppress this molecular volume in all systems in this thesis when all components have identical molecular volumes. We speak then about conserved or non-conserved quantities.

($\alpha = 2$) can occur, thus the stoichiometric matrix is given by

$$\underline{\sigma} = \begin{array}{cc} & \alpha = 1 & \alpha = 2 & & \\ \begin{pmatrix} 0 & 0 \\ -2 & -4 \\ -1 & 1 \\ 1 & 0 \end{pmatrix} & & & \begin{matrix} S \\ A \\ B \\ C \end{matrix} & . \end{array} \quad (1.23)$$

The volume stoichiometric matrix $\tilde{\underline{\sigma}}$ can be expressed as

$$\tilde{\underline{\sigma}} = \nu_A \begin{pmatrix} 0 & 0 \\ -2 & -4 \\ -4 & 4 \\ 6 & 0 \end{pmatrix} . \quad (1.24)$$

Its left nullspace is two-dimensional and we can use the row vectors $v_0 = (1, 1, 1, 1)$ (which is the conservation of volume) and $v_1 = (0, 1, 1, 1)$ as a basis of this nullspace. The remaining non-trivial conserved density is thus given by $\psi_1 = (\phi_A + \phi_B + \phi_C)/\nu_A$. With this, we can construct the non-conserved quantities via

$$U = \nu_A^{-1} \begin{pmatrix} 1 & 1 & 1 & 1 \\ 0 & 1 & 1 & 1 \\ B_{00} & B_{01} & B_{02} & B_{03} \\ B_{10} & B_{11} & B_{12} & B_{13} \end{pmatrix}, \quad \text{and } U^{-1} = \nu_A \begin{pmatrix} A_{00}^{-1} & A_{01}^{-1} & \left| \begin{array}{cc} 0 & 0 \end{array} \right. \\ A_{10}^{-1} & A_{11}^{-1} & \left| \begin{array}{cc} -2 & -4 \end{array} \right. \\ A_{20}^{-1} & A_{21}^{-1} & \left| \begin{array}{cc} -4 & 4 \end{array} \right. \\ A_{30}^{-1} & A_{31}^{-1} & \left| \begin{array}{cc} 6 & 0 \end{array} \right. \end{pmatrix}, \quad (1.25)$$

where A^{-1} is the pseudo-inverse of A , when solving for $U \cdot U^{-1} = 1$. For this example, the last equation is satisfied when

$$B_{11} = B_{12} \quad , \quad (1.26)$$

$$B_{13} = 1/6(1 + 6B_{11}) \quad , \quad (1.27)$$

$$B_{22} = 1/4(1 + 4B_{21}) \quad , \quad (1.28)$$

$$B_{23} = 1/6(1 + 6B_{21}) \quad , \quad (1.29)$$

thus we can choose for example the reaction extents $\xi_1 = (-1/12\phi_A - 1/12\phi_B + 1/12\phi_C)/\nu_A$ and $\xi_2 = (-1/6\phi_A + 1/12\phi_B)/\nu_A$.

1.2.2 Equilibrium of chemical reactions

To identify the chemical equilibrium of any given reaction scheme in the form of Eq. 1.16, we can define the forward and the backward chemical reaction free energy as

$$\mu_{\alpha}^{\pm} = \sum_{i=1}^M \sigma_{i\alpha}^{\pm} \bar{\mu}_i \quad . \quad (1.30)$$

Their difference, the so-called reaction free energy,

$$\Delta\mu_\alpha = \sum_{i=1}^M \sigma_{i\alpha} \bar{\mu}_i \quad , \quad (1.31)$$

quantifies the release of free energy when this chemical reaction runs once from the left to the right side. At chemical equilibrium of reaction α , both sides are balanced and thus

$$\Delta\mu_\alpha = 0 \quad . \quad (1.32)$$

Therefore, given a well-mixed system of $M + 1$ components, we can compute the volume fractions at chemical equilibrium via:

$$\begin{aligned} \bullet \text{ chemical equilibrium: } \Delta\mu_\alpha &= 0, & L' \\ \bullet \text{ conservation laws: } \psi_j & & \frac{M - L'}{M} \end{aligned} \quad (1.33)$$

These conditions determine the M volume fractions. The solvent volume fraction follows again from $\phi_0 = 1 - \sum_{i=1}^M \phi_i$. Any closed system, without additional driving relaxes towards this chemical equilibrium in the long time limit.

1.2.3 Mass-action kinetics towards equilibrium

The decomposition of ϕ_i in Eq. 1.22 reveals that in homogeneous systems, the only temporal evolution of ϕ_i stems from the dynamics of the reaction extents ξ_α because the conserved densities ψ_j stay constant in time. However, the reaction extent ξ_α evolves in time, with

$$\frac{d\xi_\alpha}{dt} = r_\alpha \quad , \quad (1.34)$$

when there is a net reaction rate $r_\alpha = r_\alpha^+ - r_\alpha^-$ of reaction α . The latter is the difference between the forward and backward chemical reaction rates r_α^\pm . Detailed balance of the rates requires that the ratio of these reaction rates follows

$$\frac{r_\alpha^+}{r_\alpha^-} = \exp\left(-\frac{\Delta\mu_\alpha}{k_B T}\right) \quad , \quad (1.35)$$

see, e.g., [40, 41, 42] for a general discussion. Therefore, we can write

$$r_\alpha^\pm = k_\alpha \exp\left(\frac{\mu_\alpha^\pm}{k_B T}\right) \quad , \quad (1.36)$$

where we have introduced the kinetic coefficients k_α . These coefficients are positive numbers, but can depend on composition. This dependency we utilize later to

localize the reactions within one phase⁹. With this, the net reaction rate is given by

$$r_\alpha = k_\alpha \left[\exp\left(\frac{\mu_\alpha^+}{k_B T}\right) - \exp\left(\frac{\mu_\alpha^-}{k_B T}\right) \right] , \quad (1.37)$$

which vanishes at chemical equilibrium.

According to Eq. 1.22, the temporal evolution of the volume fractions is given by

$$\frac{d\phi_i}{dt} = r_i , \quad (1.38)$$

$$r_i = \sum_{\alpha=1}^{L'} \nu_i \sigma_{i\alpha} r_\alpha , \quad (1.39)$$

where r_i is a sink or source of component i stemming from all chemical reactions in which the component is involved, $\sigma_{i\alpha} \neq 0$.

Dilute limit or no interactions

When no molecular interactions between molecules occur, or the volume fractions of all components except the solvent are dilute, the exchange activity coefficients $\bar{\gamma}_i$ can only be dependent on the solvent volume fraction. For volume conserving reactions, it holds that $\prod_{i=1}^M \bar{\gamma}_i^{\sigma_{i\alpha}^+} \propto \prod_{i=1}^M \bar{\gamma}_i^{\sigma_{i\alpha}^-}$. We can define, therefore, the so-called equilibrium coefficient

$$K_\alpha = \prod_{i=1}^M \bar{\gamma}_i^{-\sigma_{i\alpha}} \exp\left(-\frac{\sigma_{i\alpha} \omega_i}{k_B T}\right) , \quad (1.40)$$

for the chemical reaction α , which is independent of composition for dilute mixtures. Furthermore, we can define $K_\alpha^\pm = \prod_{i=1}^M \bar{\gamma}_i^{\sigma_{i\alpha}^\pm} \exp\left(\frac{\sigma_{i\alpha}^\pm \omega_i}{k_B T}\right)$, such that $K_\alpha = K_\alpha^+ / K_\alpha^-$ and write for the kinetical equations

$$\frac{d\phi_i}{dt} = \sum_{\alpha=1}^L \nu_i \sigma_{i\alpha} k_\alpha \left(K_\alpha^+ \prod_{j=1}^M \phi_j^{\sigma_{j\alpha}^+} - K_\alpha^- \prod_{j=1}^M \phi_j^{\sigma_{j\alpha}^-} \right) . \quad (1.41)$$

Any composition dependency left in K_α^\pm can be compensated by the kinetic coefficient k_α . Therefore, reaction fluxes can be proportional only to the volume fractions to the power of the stoichiometric matrices, in the simplest case. In the long time limit, the chemical equilibrium is reached, and for each chemical reaction, it holds that

$$K_\alpha = \prod_{i=1}^M \phi_i^{\sigma_{i\alpha}} , \quad (1.42)$$

see, e.g., [43]. Using Eq. 1.40 and Eq. 1.42 together we obtain again $\Delta\mu_\alpha = 0$, which is the general condition for chemical equilibrium. The dilute regime is characterized, therefore, by the condition that K_α is composition independent. For systems with

⁹In general, also different choices of Eq. 1.36 are possible when introducing k_α^\pm , such that Eq. 1.35 still holds. However, due to simplicity, we choose the symmetric version stated in Eq. 1.35.

interactions and non-dilute concentrations, the equilibrium constants K_α have to be composition-dependent. This, we show in the following.

1.3 Simultaneous equilibrium of chemical reactions and phase separation

The thermodynamic equilibrium of phase separating mixtures in the presence of chemical reactions is reached when the conditions of phase equilibrium, stated in Eq. 1.6, and the requirements of chemical equilibrium, stated in Eq. 1.33, are satisfied simultaneously. Chemical equilibrium can be reached in all phases simultaneously, because, as Landau and Lifshitz [44] write “[...] the condition (chem. equilibrium) retains its form even when the reacting substances are distributed in the form of solutes in two different phases in contact. This follows from the fact that in equilibrium the chemical potentials of each substance in either phase must be equal, in accordance with the conditions for phase equilibrium.” In our framework, we summarize the condition for a two-phases coexistence in a system with $M + 1$ components and $L' < M + 1$ linearly independent reactions by

$$\begin{aligned}
 & \bullet \text{ chem. pot. balance between phases: } \bar{\mu}_i^{\text{I}} = \bar{\mu}_i^{\text{II}}, & M \\
 & \bullet \text{ pressure condition: } f^{\text{I}} - f^{\text{II}} = \sum_{i=1}^M \frac{\bar{\mu}_i^{\text{I/II}}}{\nu_i} (\phi_i^{\text{I}} - \phi_i^{\text{II}}) - \frac{2\gamma}{R}, & 1 \\
 & \bullet \text{ chemical equilibrium: } \Delta\mu_\alpha^{\text{I/II}} = 0, & L' \\
 & \bullet \text{ conservation laws: } \frac{\bar{\psi}_i - \psi_i^{\text{II}}}{\psi_i^{\text{I}} - \psi_i^{\text{II}}} = \frac{\bar{\psi}_j - \psi_j^{\text{II}}}{\psi_j^{\text{I}} - \psi_j^{\text{II}}}, & M - L' - 1 \\
 & & \hline
 & & 2M \quad (1.43)
 \end{aligned}$$

which determines the $2M$ volume fractions at equilibrium. The volume of phase I follows again, similar to Eq. 1.7, from

$$\frac{V^{\text{I}}}{V} = \frac{\bar{\psi}_i - \psi_i^{\text{II}}}{\psi_i^{\text{I}} - \psi_i^{\text{II}}}, \quad (1.44)$$

while $V^{\text{II}} = 1 - V^{\text{I}}$.

From Eq. 1.43, we can immediately show why, in general, the equilibrium constants K_α , as defined in Eq. 1.40, can not be composition-independent when a system phase separates. From the condition of identical chemical potentials follows the identity of activities between the phases, thus $\bar{\gamma}_i^{\text{I}}\phi_i^{\text{I}} = \bar{\gamma}_i^{\text{II}}\phi_i^{\text{II}}$. Thus, the partition factor, defined by the ratio of the volume fractions $P_i = \phi_i^{\text{I}}/\phi_i^{\text{II}}$, fulfils $P_i = \bar{\gamma}_i^{\text{II}}/\bar{\gamma}_i^{\text{I}}$ at phase equilibrium. Furthermore, when writing down the equilibrium constants $K_\alpha^{\text{I/II}}$, which follow from chemical equilibrium, we need a phase index I/II due to composition dependency of $\bar{\gamma}_i$. The partition coefficient of phase separation and the

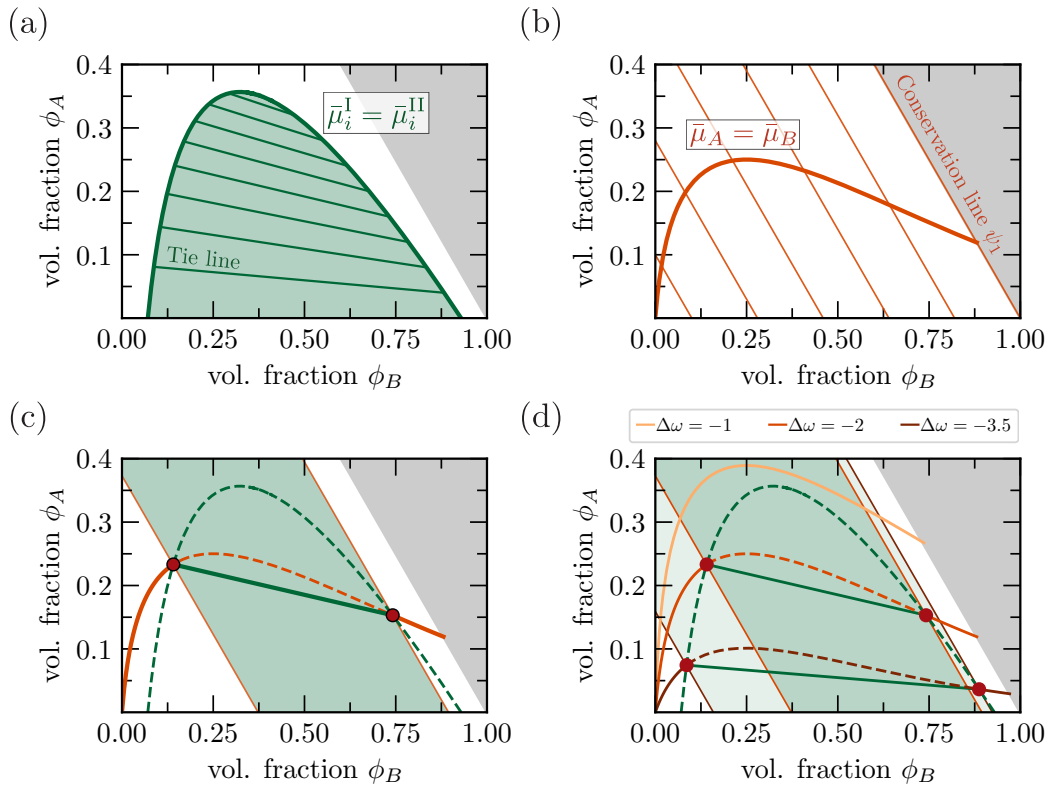


FIGURE 1.3: **Partial and thermodynamic equilibrium in a ternary mixtures:** (a): A phase diagram of a ternary mixture ($M = 2$) with components A , B , and S is shown. Phase equilibrium is established at the binodal line (thick green line). Systems with average compositions within the binodal area (green) have coexisting phases at equilibrium, determined by the corresponding tie line (thin green lines). (b): The graphical representation of the chemical equilibrium of the reaction $A \rightleftharpoons B$ is shown ($L' = 1$). The thick orange line is the line at which the reaction free energy $\Delta\mu$ vanishes. However, chemical reactions cannot alter $\psi = \phi_A + \phi_B$, leading to the conservation lines (thin orange). (c): The thermodynamic equilibrium for this system is visualized. In the white domains, it is reached at homogeneous systems at the chemical equilibrium line (orange). In the green domain, the equilibrium is dictated by the green tie line obtained by the intersections of the binodal (dashed green) and the chemical equilibrium line. (d): Different thermodynamic equilibria for three parameter choices of reference chemical potentials ω_i , leading to different $\Delta\omega = \omega_B - \omega_A$, are shown. While the binodal stays constant under these parameter changes, the chemical equilibrium line gets shifted. For more details and parameters, see App. C.

chemical equilibrium coefficient are connected via

$$\frac{K_\alpha^I}{K_\alpha^{II}} = \prod_{i=1}^M P_i^{\sigma_{i\alpha}} \quad . \quad (1.45)$$

As we will show later, this also has direct consequences on the dynamics. Using mass-action kinetics suitable for dilute systems will most likely break the assumption of detailed balance of the rates and make the chemical reactions active.

We continue by illustrating the conditions Eq. 1.43, first, for a ternary ($M = 2$) mixture with one chemical reaction. In FIG. 1.3, we consider a ternary mixture where B can phase separate from the solvent. Furthermore, we allow the chemical reaction

$A \rightleftharpoons B$. The phase diagram is shown in FIG. 1.3(a). It is the graphical representation of Eq. 1.6 for this system. The thick green line denotes the binodal line at which $\bar{\mu}_i^I = \bar{\mu}_i^{II}$. Furthermore, we show a set of tie-lines (thin green lines). These lines are the graphical expression of the conservation laws denoted in Eq. 1.6. They represent the linear relationship how $\bar{\phi}_A$ and $\bar{\phi}_B$ have to be altered such that the same equilibrium volume fractions are reached, but only the phase volumes differ. Inside the binodal area (green), the system's equilibrium without chemical reactions would be a phase-separated state. Furthermore, the system can never be in the grey area where $\nu_S \psi_1 = \phi_A + \phi_B > 1$.

In FIG. 1.3(b), we show the graphical representation of Eq. 1.33 for this system. Here, the line of vanishing reaction free energy, thus $\bar{\mu}_A = \bar{\mu}_B$ for this chemical reaction, is shown by the thick orange line. Furthermore, we show a set of lines of different values of the conserved quantity $\psi = \phi_A + \phi_B$ (thin orange lines). Only along these lines, the chemical reaction can alter $\bar{\phi}_A$ and $\bar{\phi}_B$.

The thermodynamic equilibrium, thus the graphical representation of Eq. 1.43, is shown in FIG. 1.3(c). The thermodynamic equilibrium of all the systems with average composition within the green area is given by a coexistence of two phases with volume fraction values denoted by the red dots. These points are the intersection of the binodal with the chemical equilibrium line. Due to the structure of Eq. 1.43, it is guaranteed that these intersection points are always connected via a tie line. The system within the green area can only differ in sizes of the two phases $V^{I/II}$. Their ratio is given by the intersection of the line of conserved quantity with the unique tie line. All the systems with average composition outside the green area, will have a well-mixed equilibrium state given by the intersection of the line of conserved quantity with the chemical equilibrium line.

The equilibrium conditions for phase equilibrium are invariant under changing the reference chemical potentials ω_i . However, these values strongly affect the chemical equilibrium. We illustrate this in FIG. 1.3(d). While the binodal is always the same, the chemical equilibrium line changes for different values of $\Delta\omega = \omega_A - \omega_B$. However, whenever there are intersections between these two lines, they are always connected via a tie line.

To illustrate how this generalizes for systems with more components and several reactions, we briefly discuss the case of a quaternary system ($M = 3$) with one or two reactions. In FIG. 1.4(a), we show a binodal manifold (green) of a system with components A, B, C and S , where only C can phase separate on its own from the solvent S . In addition, here we consider the chemical reaction $A + B \rightleftharpoons C$. The corresponding chemical equilibrium manifold is shown in orange. These two manifolds intersect in a closed line, shown in FIG. 1.4(b) as a green-orange dashed line. A new manifold is spanned when all the points at this line are connected via their tie lines. The thermodynamical equilibrium of any system can now be constructed when knowing the values of the average conserved quantities. Here, we have chosen $\psi_1 = \phi_A + \phi_B + \phi_C$ and $\psi_2 = \phi_A - \phi_B$. The latter can be represented here by planes in composition space (two exemplary ones are shown in grey and blue).

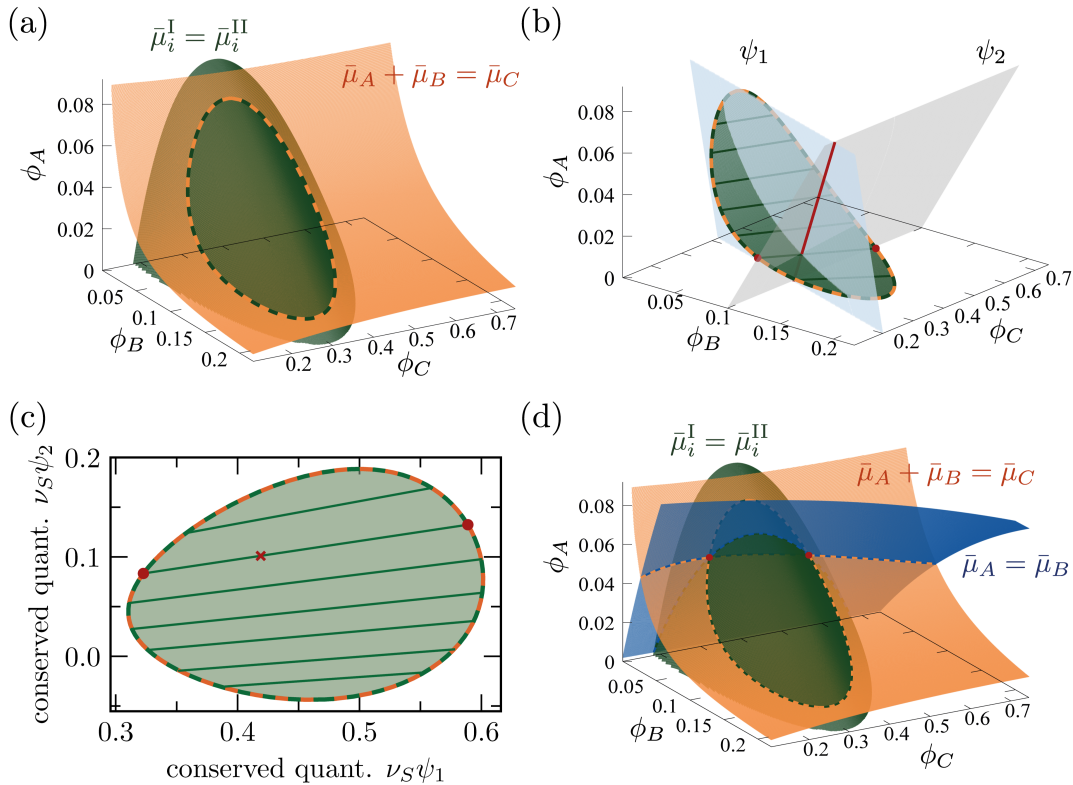


FIGURE 1.4: **Thermodynamic equilibrium for quaternary mixtures:** (a): The binodal manifold (green) for a quaternary system ($M = 3$) with components A , B , C , and S , and the chemical equilibrium manifold (orange) for the chemical reaction $A + B \rightleftharpoons C$ ($L' = 1$). (b): The intersection of the two manifolds forms a circle (green-orange dashed). The tie lines along the circle (thin green lines) span a plane. The chemical reaction conservers $\psi_1 = \phi_A + \phi_B + \phi_C$ and $\psi_2 = \phi_A - \phi_B$. These conserved quantities can be represented by planes (grey and blue). Two phases coexist at equilibrium whenever these planes intersect within the closed circle. (c): We show the phase diagram in the composition space of the two conserved quantities. The binodal and chemical equilibrium line is shown with the green-orange dashed, and the thin green lines are tie lines. (d): When the additional reaction $A \rightleftharpoons B$ is allowed ($L' = 2$), a second chemical equilibrium manifold can be constructed, leading again to a unique thermodynamic equilibrium where all of the manifolds intersect (red dots). For the parameters, see App. C.

Whenever the line, lying on both planes of the conserved quantities (red line for this example), intersects the manifold constructed via the tie lines, two phases coexist at thermodynamic equilibrium. Their volume fractions are given by the corresponding tie line (red dots). Alternatively, we show the phase diagram in the composition space of the conserved quantities in FIG. 1.4(c). The dimensionality of this space is reduced by one due to the condition of chemical equilibrium.

Furthermore, when allowing additionally the chemical reaction $A \rightleftharpoons B$, we obtain a second chemical equilibrium manifold, shown in blue in FIG. 1.4(d). With two reactions, just ψ_1 is still a conserved quantity, while $\phi_A - \phi_B$ is no longer conserved. Thus, the thermodynamic equilibrium is determined by the intersection of the two chemical equilibrium manifolds (blue-orange dashed line). However, when this line enters the binodal area, again, just one distinct phase equilibrium is selected. Changing the

conserved quantity within the binodal area just leads to differently sized phase volumes.

1.4 Chemical reactions maintained away from equilibrium

So far, we have discussed the thermodynamic equilibrium state and the relaxation kinetics toward this equilibrium. However, many systems and every biological system are driven out of equilibrium. The literature on so-called active matter is rich and many different ways exist how detailed balance can be broken. Examples are given by noise terms in the dynamics which do not satisfy the fluctuation-dissipation theorem, see, e.g., [45], or breaking the symmetry or reciprocal relations of Onsager coefficients, see, e.g., [46]. However, many transition processes in biology are driven away from equilibrium by the supply of chemical fuels, e.g. ATP in cells. Two examples are given by channels and pores, which pump ions against concentration gradients, and electrical potentials across membranes [47], or molecular motors that generate mechanical forces [48]. Under the consumption of these fuel molecules, chemical reactions run in the opposite direction than they would normally do in the absence of fuel. Instead of taking the fuel dynamics into account, these processes can be modeled by additional chemical energy, in this thesis, we will refer to it as $\Delta\tilde{\mu}$, which breaks the detailed balance condition [49]. This is motivated by the idea that these 'hidden' processes are faster than the modeled processes, e.g., fast ATP diffusion inside cells.

For driven chemical reactions, this additional chemical energy $\Delta\tilde{\mu}$ can therefore be interpreted as the chemical potential from 'hidden' chemical species that are involved in the corresponding chemical reaction. However, these species are always in excess and constantly supplied or removed. Therefore, we break the detailed balance condition in Eq. 1.35 by additional terms in the forward and backward chemical reaction energies $\tilde{\mu}_\alpha^\pm$. Instead of Eq. 1.30, we write

$$\mu_\alpha^\pm = \sum_{i=1}^M \sigma_{i\alpha}^\pm \bar{\mu}_i + \tilde{\mu}_\alpha^\pm \quad , \quad (1.46)$$

when the chemical reaction α is driven. Thus the total reaction free energy is given by

$$\Delta\mu_\alpha = \sum_{i=1}^M \sigma_{i\alpha} \bar{\mu}_i + \Delta\tilde{\mu}_\alpha \quad , \quad (1.47)$$

with $\Delta\tilde{\mu}_\alpha = \tilde{\mu}_\alpha^+ - \tilde{\mu}_\alpha^-$. Due to this driving, such systems do not relax towards equilibrium.

However, even when chemical reactions are driven, some systems can be described by an effective equilibrium system when these additional chemical energies can be recast in the chemical potentials of the species $i = 1, \dots, M$. Thus, defining an effective free energy. In general, this cannot be achieved. For cyclic reaction networks,

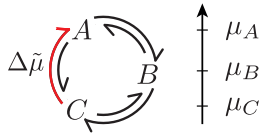


FIGURE 1.5

driving specific chemical reactions by a supply of chemical energy $\Delta\tilde{\mu}_\alpha$ leads to a system for which no equilibrium description can be found. By redefining the chemical potentials of species involved in this reaction α , also their chemical potentials for the other chemical reactions would change. Thus, such a system is active, and any stationary state is a non-equilibrium one. However, we need at least three components and three chemical reactions for building a cycle.

In FIG. 1.5 we sketch such a cyclic system with components A , B , and C and chemical reactions $A \rightleftharpoons B$ ($\alpha = 1$), $B \rightleftharpoons C$ ($\alpha = 2$), and $C \rightleftharpoons A$ ($\alpha = 3$). The latter is driven towards the forward directions, via an external energy supply $\Delta\tilde{\mu}_\alpha$. The dynamics of each component are affected by the two chemical reactions it is involved in, e. g., $d_t\phi_A = \nu_A(r_3 - r_1)$. When $\Delta\tilde{\mu}_\alpha \neq 0$, no effective chemical potentials can be found for which the detailed balance conditions could be written without any active driving. Thus, no volume fractions can be found, for which the individual r_α vanish simultaneously. However, a stationary state can be found when all chemical reactions occur with the same non-vanishing rate $r_\alpha = r$. A detailed discussion of driven chemical reaction in cyclic biochemical networks is given in [8].

1.5 Structure of this thesis

In this thesis, we study how chemical reactions can be organized by phase separation. Starting from the thermodynamic description given in this chapter, we show how systems can relax towards their equilibrium, defined by simultaneous phase and chemical equilibrium. Furthermore, we show two ways how these systems can be maintained away from equilibrium. First, when chemical reactions are driven differently in phases, chemical and phase equilibrium cannot be reached at the same time. Second, by allowing chemical reactions only in one phase, chemically active droplets of this phase can be driven out of equilibrium by controlling the concentrations at the system boundaries. The remaining chapters of this thesis are organized as follows.

Chapter 2 generalizes mass-action kinetics to systems where phase separation has led to homogeneous compartments. Here, we consider fast diffusive processes compared to chemical reactions rates on the relevant length scales. With this, we discuss the relaxation kinetics towards equilibrium and show the existence of non-equilibrium steady states in systems with driven chemical reactions. In Chapter 3, we introduce the dynamical equations of chemical reactions and phase separation in spatially continuous systems of multi-component mixtures. Again, we study the relaxation dynamics and out-of-equilibrium situations, either by driving chemical reactions or by coupling the system to reservoirs at the system boundaries. Solving these equations numerically reveals that the droplet can stop ripening, elongate and even divide in out-of-equilibrium situations. For studying the dynamics

of chemically active droplets quantitatively, we introduce an effective description of chemically active droplets in multi-component mixtures in Chapter 4. In the limit of a sharp interface, we can describe their dynamics by two sets of linear reaction-diffusion equations coupled via a moving interface. In Chapter 5, we introduce a protocell model of chemically active droplets. Here, we take the nutrient and waste dynamics explicitly into account. Thus, we obtain a minimal model of metabolic processes in these protocells. We discuss two different forms of driving for maintaining these chemically active droplets away from equilibrium, boundary driven and bulk driven. In Chapter 6, we show why chemically active droplets with driven chemical reactions in the bulk do not divide in 2D. However, for building minimal models of chemically active droplets showing division, we introduce chemical reactions at the interface of droplets. When these chemical reactions depend on the mean curvature of the interface, chemically active droplets can divide robustly in 2D. Finally, we conclude the main results of this thesis and point out possible directions for future research in Chapter 7.

Chapter 2

Chemical reactions in compartmentalized systems

This chapter studies chemical reactions in compartments formed by phase separation. These compartments are homogeneous phases that are at phase equilibrium at all times. This setting occurs in systems where chemical reactions are much slower than diffusion on the relevant length scales. As a result, we obtain homogeneous coexisting phases. For simplicity, we focus on two-phase coexistence, phases I and II, in this chapter. Each phase is characterized by its phase volume $V^{I/II}$ and M composition variables. However, the generalization to multi-phase coexistence is straightforward.

To investigate their dynamics, we generalize the mass-action kinetics of homogeneous systems for chemical reactions that take place in compartmentalized systems. With this, we study the relaxation kinetics in passive systems towards thermodynamic equilibrium when initialized away from chemical equilibrium. During this relaxation kinetics, however, phase equilibrium is fulfilled at all times. The second part of this chapter studies driven chemical reactions in compartmentalized systems. In homogeneous mixtures, driven situations with non-vanishing fluxes can only occur with driven chemical reactions in cyclic reaction networks, see Section 1.4. However, no effective equilibrium situation can be found in compartmentalized systems when chemical reactions are driven differently in the compartments. Nevertheless, in the limit of infinite fast diffusion, phase equilibrium is always maintained, while chemical reactions are driven out of equilibrium. We show the conditions for non-equilibrium steady states and introduce a method to visualize the selected phase equilibrium when chemical reactions are driven. This chapter was the result of a cooperation with Sudarshana Laha and Patrick McCall.

2.1 Mass-action kinetics for compartments built by phase separation

We have introduced the exchange chemical potentials $\bar{\mu}_i$ for $i = 1, \dots, M$ in Eq. 1.2, and stated the conditions of phase equilibrium in Eq. 1.6. We found that all the

exchange chemical potentials of the M non-solvent species and the osmotic pressure must be balanced. However, in this chapter, it is more convenient to use chemical potentials instead of the exchange chemical potentials. When considering the Gibbs free energy G , they are defined by $\mu_i = \partial G / \partial N_i = \partial g / \partial n_i + \nu_i (g - \sum_{k=0}^M n_k \partial g / \partial n_k)$, for $i = 0, \dots, M$, where $n_i = N_i / V$ is the concentration of component i , see [50]. Analogously to Eq. 1.2, these chemical potentials can be written as

$$\mu_i = k_B T \log(\gamma_i \phi_i) + \omega_i \quad , \quad (2.1)$$

where ω_i a reference chemical potential and γ_i is the activity coefficient. With these coefficients, we can define the activity of each component i as $\gamma_i \phi_i$. Phase equilibrium requires the equality of these $M + 1$ chemical potentials between phases. It is this symmetric form of the phase equilibrium condition which simplifies our expressions in this chapter. However, for an incompressible system, thus constant molecular volumes, the equality of the $M + 1$ chemical potentials is identical to the equality of M exchange chemical potentials and the Osmotic pressure condition, when the energetic cost of the interface is negligible.

2.1.1 Dynamical equations for densities and phase volumes

Section 1.2.3 studies the volume fraction dynamics for systems with chemical reactions in homogenous mixtures with dilute reactants, leading to the classical mass-action kinetics. However, in systems with coexisting phases, the volume fractions in each phase¹ $\phi_i^{I/\Pi} = \nu_i N_i^{I/\Pi} / V^{I/\Pi}$ become dynamic variables. Their time evolution is affected by changes in particle numbers $N_i^{I/\Pi}$ in the phases and changes in the phase volumes $V^{I/\Pi}$.

While in homogeneous mixtures, reaction rates are the only contributions to particle numbers changes, particle exchanges across the phase boundary can also change their numbers in systems with coexisting phases. The volume fraction dynamics for systems with coexisting phases read, therefore

$$\frac{d\phi_i^{I/\Pi}}{dt} = r_i^{I/\Pi} - j_i^{I/\Pi} - \frac{\phi_i^{I/\Pi}}{V^{I/\Pi}} \frac{dV^{I/\Pi}}{dt} \quad , \quad (2.2)$$

where $r_i^{I/\Pi}$ are sinks or sources of component i due to chemical reactions, and $j_i^{I/\Pi}$ are the diffusive exchange rates between phases per phase volume $V^{I/\Pi}$. Note that only in this chapter do diffusive exchange rates have the units of volume fraction per time. Furthermore, the volume fraction of particles also changes when the particle number $N^{I/\Pi}$ stays constant but the respective volume $V^{I/\Pi}$ changes. The last term in Eq. 2.2 captures this effect and couples the dynamics of all components i .

The volume of each phase is built up by all particles, $V^{I/\Pi} = \sum_{i=0}^M \nu_i N_i^{I/\Pi}$. Therefore, changes in particle numbers, thus volume fractions, are directly coupled to changes

¹Here, we consider the molecular volumes to be constant. However, this framework can be easily generalized to the more complicated scenario of compressible systems. For simplicity and consistency in this work, we focus on these incompressible cases. A more general discussion can be found [51].

in phase volume. Their time evolution follows therefore

$$\frac{dV^{I/II}}{dt} = V^{I/II} \left(\sum_{i=0} r_i^{I/II} - j_i^{I/II} \right) . \quad (2.3)$$

The total system size $V = V^I + V^{II}$, however, must stay constant in an incompressible system, due to Eq. 1.18. The conservation of particle numbers under the diffusive exchange obeys

$$V^I j_i^I = -V^{II} j_i^{II} . \quad (2.4)$$

Furthermore, this conservation causes that the temporal evolution of the average volume fractions $\bar{\phi}_i = (V^I \phi_i^I + V^{II} \phi_i^{II}) / (V^I + V^{II})$ follows

$$\frac{d\bar{\phi}_i}{dt} = \frac{V^I r_i^I + V^{II} r_i^{II}}{V^I + V^{II}} , \quad (2.5)$$

which is independent of the diffusive exchanges.

Diffusive exchange fluxes maintain phase equilibrium

As mentioned above, in the Gibbs Ensemble, phase equilibrium requires the equality of chemical potentials between phases. This condition is equivalent to the equality of all activities, thus $\gamma_i^I \phi_i^I = \gamma_i^{II} \phi_i^{II}$. Therefore, maintaining phase equilibrium along the time evolution constrains the volume fractions dynamics via $d_t(\gamma_i^I \phi_i^I) = d_t(\gamma_i^{II} \phi_i^{II})$. Using a simple product rule, this can be rewritten as

$$\gamma_i^I \frac{d\phi_i^I}{dt} + \phi_i^I \sum_{k=0}^M \frac{\partial \gamma_i^I}{\partial \phi_k^I} \frac{d\phi_k^I}{dt} = \gamma_i^{II} \frac{d\phi_i^{II}}{dt} + \phi_i^{II} \sum_{k=0}^M \frac{\partial \gamma_i^{II}}{\partial \phi_k^{II}} \frac{d\phi_k^{II}}{dt} \quad (2.6)$$

It is important to note that while applying Eq. 2.2 and Eq. 2.3, Equation 2.6 remains linear in $j_i^{I/II}$. Therefore, Equations 2.4 and Eq. 2.6 define a system of $2(M+1)$ linear equations that can be inverted, leading to maybe lengthy, but closed-form expression of $j_i^{I/II}$ ($\{r_k^I, r_k^{II}, V^I, V^{II}\}$). These so constructed diffusive exchange fluxes ensure phase equilibrium between phases, while chemical reaction fluxes can change the volume fractions in phases. The numerical power of this approach becomes apparent when reminded that, in general, constructing the binodal manifold of a multi-component phase diagram requires looping over transcendental equations. Here, after initializing the system at one point on the binodal manifold, only closed-form expressions must be obeyed to stay on the binodal manifold along with the evolution in time.

Chemical reaction rates at phase equilibrium

In Section 1.2.3, we introduced the reaction rates in homogenous systems. There, differences in the forward and backward chemical reaction free energy μ_α^\pm drive the chemical reaction α with a net rate r_α . When component i participates in reaction α , thus $\sigma_{i\alpha} \neq 0$, this net reaction rate causes the a sink or source term r_i for species

i. The same holds true for homogenous compartments, when phase specific source and sink terms $r_i^{I/II}$ are considered. We find²,

$$r_i^{I/II} = \sum_{\alpha=1}^L k_{\alpha}^{I/II} \sigma_{i\alpha} \nu_i \left[\exp\left(\frac{\mu_{\alpha}^{\dagger}}{k_B T}\right) - \exp\left(\frac{\mu_{\alpha}^{-}}{k_B T}\right) \right] . \quad (2.7)$$

However, for coexisting phases at phase equilibrium $\mu_i^I = \mu_i^{II}$. Thus, the forward and backward reaction free energies μ_{α}^{\pm} are equal between the phases, and the bracket in Eq. 2.7 loses its phase dependency. The only phase dependency of $r_i^{I/II}$ can stem from a composition dependency of the kinetic coefficients k_{α} . Therefore, the increased concentration of a reacting solute by phase separation does not necessarily increase the reaction rates in which it is involved. However, composition-dependent kinetic coefficients can affect the dynamics strongly.

2.1.2 Relaxation kinetics in a simple example

A consequence of phase separation is that the reaction rates r_{α} can, in general³, not be linear in volume fraction when the system can relax towards equilibrium, even for unimolecular reactions. In the following, we study a unimolecular reaction in a ternary mixture to illustrate these effects and study the consequence of compartment-dependent kinetic coefficients k_{α} . However, the framework introduced above is general and can be applied to more complicated systems with multiple components and reactions.

In Section 1.3, the thermodynamic equilibrium for a ternary mixture, composed out of components A , B and S , with the chemical reaction $A \rightleftharpoons B$ was discussed. Here, we study the relaxation kinetics towards this equilibrium in compartmentalized systems. Therefore, we solve the governing Eq. 2.2 and Eq. 2.3 numerically. The resulting kinetics leads to a trajectory in composition space, constrained by conservation laws. We illustrate this trajectory in the phase diagram in FIG. 2.1(a) for two different initial conditions. Initial condition 1 starts in the homogeneous area of the phase diagram. When the trajectory hits the area of coexisting phases, the system phase separates and follows the binodal line. Initial condition 2 starts already in the separated area. Therefore, the volume fractions $\phi_{A/B}^{I/II}$ have to be initialized on the binodal line, which the trajectory follows from thereon. Both initial conditions reach the same thermodynamical equilibrium. The convergence in volume fraction ϕ_B is shown in FIG. 2.1(b).

Composition-dependent kinetic coefficients alter the kinetics, see FIG. 2.1(c)-(d). For simplicity, we choose a composition dependency affecting phase I uniformly⁴. For initial condition 1, the early time evolution in the homogeneous area is identical for

²Please note, in the rest of the thesis, we use exchange chemical potentials and the Helmholtz ensemble. Here, we use the Gibbs ensemble. For incompressible mixtures, this leads only to a different definition of k_{α} for the symmetric choice of Eq. 1.36 and shows the ambiguity of the kinetic coefficient.

³They can only be linear for a specific choice of identical molecular interactions for reacting species.

⁴A dependency of such kind could read for example $k = k^{II} + (k^I - k^{II})\text{sig}(\phi_B - \phi_B^{\text{crit}})$.

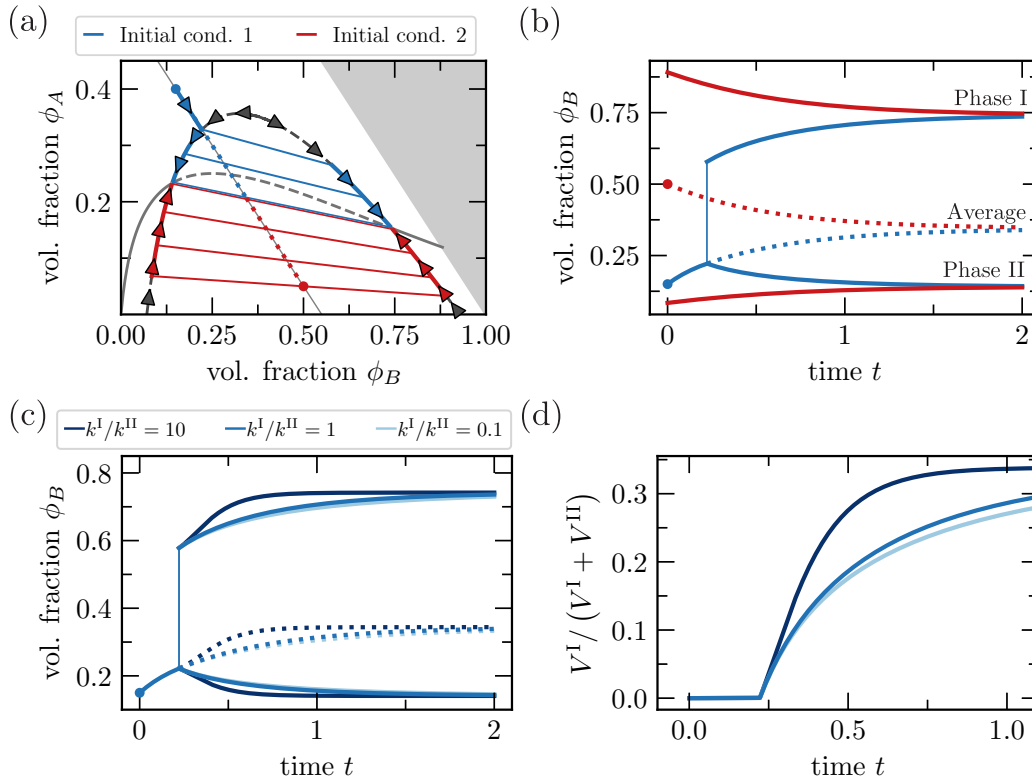


FIGURE 2.1: **Unimolecular reaction kinetics:** We show the relaxation dynamics of a ternary system, composed out of components A , B , and S , with the chemical reaction $A \rightleftharpoons B$, towards the thermodynamic equilibrium. Fig. (a) shows trajectories for two systems with the same amount of conserved material $\phi_A + \phi_B$, only differ in their relative composition at initialization. Whenever the system can phase separate, these trajectories follow the binodal line. Fig. (b) displays the temporal evolution of $\phi_B^{I/II}$ and its average $\bar{\phi}_B$ for these relaxation processes is shown for cases with a phase independent kinetic coefficient k_α . Fig. (c) shows $\phi_B^{I/II}$'s temporal evolution for the initial condition 1 for different kinetic coefficients k^I . The dynamics of the corresponding relative phase volumes $V^I/(V^I + V^{II})$ is shown in Fig. (d). Phase equilibrium ensures that the combination of distinct values for ϕ^I , ϕ^{II} , and V^I always occur together. For more details, see App. C.

different values of k^I/k^{II} due to the absence of phase I. As expected, when the trajectory hits the binodal line, the different kinetic coefficients accelerate or decelerate the time evolution. However, due to phase equilibrium, the phases can not develop independently. Therefore, increasing the kinetic coefficient just in one phase automatically speeds up the time evolution of volume fractions in the other phase, see FIG. 2.1(c). Furthermore, the time evolution of the phase volumes is affected, see FIG. 2.1(d). When the system demixes, phase I is spontaneously built, leading to a kink in the temporal evolution of V^I . The initial slope of the growing phase is affected by the kinetic coefficients, FIG. 2.1(d).

Due to the chemical reaction, material B is net produced for initial condition 1 in FIG. 2.1. With this, the chemical reaction leads to the growth of phase I. However, when the kinetic coefficient is phase-dependent, a non-linear feedback exists. In the case of $k^I > k^{II}$, for example, the chemical reaction occurs faster in the growing phase, therefore, more B material gets produced faster, which leads again to

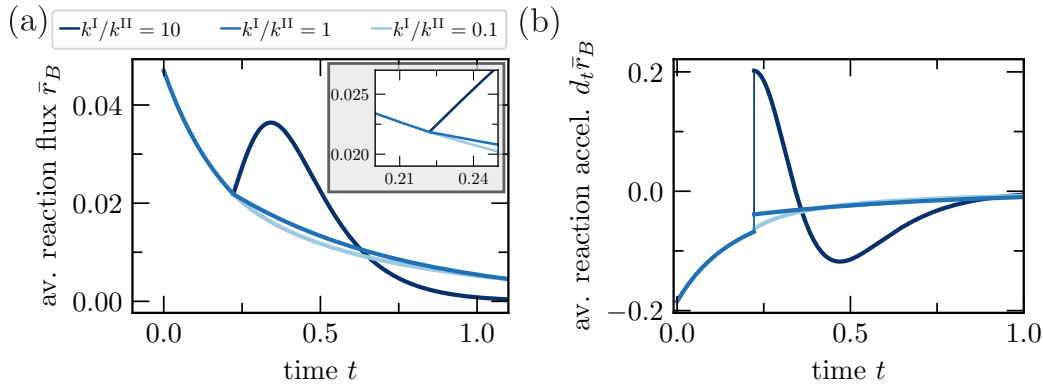


FIGURE 2.2: **Average reaction flux and acceleration:** Phase separation can accelerate or decelerate the net production of a material. We illustrate this by showing the averaged B -production $\bar{r}_B = (V^I r_B^I + V^{II} r_B^{II}) / (V^I + V^{II})$ for the initial condition I from FIG. 2.1 in Fig. (a). At the onset of phase separation, zoomed in the inset, \bar{r}_B has a kink, leading to a jump in the averaged reaction acceleration, shown in Fig. (b). For further details, see App. C.

faster growth of phase I. We show the consequence of this feedback for the averaged production of material B , $\bar{r}_B = (V^I r_B^I + V^{II} r_B^{II}) / (V^I + V^{II})$ (right-hand side of Eq. 2.5) in FIG. 2.2(a). When the system demixes, an initial increase of the average B -production occurs when $k^I/k^{II} = 10$, leading to a kink in its temporal evolution. However, the thermodynamical equilibrium is reached faster here, and therefore, the average reaction rate has to vanish earlier than in other cases, leading to a maximum of \bar{r}_B . In general, at the onset of phase separation, the averaged source and sink terms of chemical reactions \bar{r}_B are continuous but not differentiable functions. This leads to a jump of the averaged acceleration $d_t \bar{r}_i$, see FIG. 2.2(b). This discontinuous behavior is a direct consequence of the kink in the time evolution of the phase volumes.

2.2 Driven chemical reactions in compartmentalized systems

The kinetic equations described in the first part of this chapter can be used not only for studying the relaxation towards the thermodynamical equilibrium but also for non-equilibrium situations. In Section 1.4, we introduced how driven chemical reactions in cyclic reaction networks can lead to non-equilibrium steady states, where no effective equilibrium description can be found, and chemical reactions occur with constant rates at a steady state. In compartmentalized systems, driving chemical reactions differently in the phases, thus a compartment dependency of $\Delta \tilde{\mu}_\alpha^{I/II}$, does not allow an equilibrium description either⁵.

Analogously to Eq. 1.46, we include the driving of chemical reactions in compartmentalized systems by writing the forward and backward chemical reaction free

⁵Such dependencies can arise, e.g. when the kinetic coefficients of reactions involving the 'hidden' components, introduced in Section 1.4, are affected by phase separation.

energies as

$$\mu_{\alpha}^{\pm, I/II} = \sum_{i=0}^M \sigma_{i\alpha}^{\pm} \mu_i + \tilde{\mu}_{\alpha}^{\pm, I/II} \quad (2.8)$$

where the chemical energy supply $\Delta \tilde{\mu}_{\alpha}^{I/II} = \tilde{\mu}_{\alpha}^{-I/II} - \tilde{\mu}_{\alpha}^{+I/II}$. When $\Delta \tilde{\mu}_{\alpha}^I \neq \Delta \tilde{\mu}_{\alpha}^{II}$, the reaction free energy becomes compartment-dependent $\Delta \mu_{\alpha}^{I/II}$. Therefore, an effective equilibrium of chemical reactions, thus $\Delta \mu_{\alpha}^{I/II} = 0$, can not be reached simultaneously when the chemical potentials have to obey $\mu_i^I = \mu_i^{II}$. The latter is the condition for phase equilibrium. With this, phase equilibrium and chemical equilibrium contradict each other. Thus, phase-specific driving of chemical

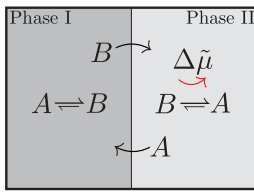


FIGURE 2.3

reactions forbid an equilibrium description already in binary mixtures with just one chemical reaction.

In FIG. 2.3, we sketch an exemplary system with components A and B which can convert into each other. This chemical reaction is driven in phase II. Thus, if these two compartments were isolated from each other, both would settle at effective chemical equilibria with different chemical potentials of the components. However, the diffusive transport equi-

librates differences in chemical potentials between compartments. In the limit of infinite fast diffusion, phase equilibrium is always maintained, even in the presence of chemical driving. With this, non-equilibrium steady states can occur where the constant chemical reaction fluxes are balanced by fluxes of components between the compartments. We study these non-equilibrium steady states in the following.

2.2.1 Non-equilibrium steady states at phase equilibrium

As mentioned above, we assume phase equilibrium between the compartments at all times. Thus, the chemical potentials of all components have to be identical between the phases. With this, the reaction free energy in the absence of chemical driving, as defined in Eq. 1.31, does not vanish but has to have the same value at all times. We define the chemical reaction free energy at the non-equilibrium steady state as

$$\Delta \mu_{\alpha}^{\text{NESS}} = \sum_{i=0}^M \sigma_{i\alpha} \mu_i^{\text{NESS}} \quad , \quad (2.9)$$

where μ_i^{NESS} is the chemical potentials of species i at the steady state. From the stationary state of Eq. 2.2 and Eq. 2.3, and the conservation law Eq. 2.4, it follows that

$$V^I r_i^I = -V^{II} r_i^{II} \quad , \quad (2.10)$$

for two phases at phase equilibrium. Any net excess material produced in one phase is balanced by a net shortfall in the other phase at steady state. From here, we can

conclude the stationary condition

$$\Delta\mu_\alpha^{\text{NESS}} = k_B T \log \left(\frac{k_\alpha^{\text{I}} V^{\text{I}} \exp\left(\frac{\tilde{\mu}_\alpha^{+, \text{I}}}{k_B T}\right) + k_\alpha^{\text{II}} V^{\text{II}} \exp\left(\frac{\tilde{\mu}_\alpha^{+, \text{II}}}{k_B T}\right)}{k_\alpha^{\text{I}} V^{\text{I}} \exp\left(\frac{\tilde{\mu}_\alpha^{-, \text{I}}}{k_B T}\right) + k_\alpha^{\text{II}} V^{\text{II}} \exp\left(\frac{\tilde{\mu}_\alpha^{-, \text{II}}}{k_B T}\right)} \right). \quad (2.11)$$

The non-equilibrium steady state chemical reaction free energy $\Delta\mu_\alpha^{\text{NESS}}$, therefore, couples the kinetic coefficients k_α^\pm , the active reaction free energies $\tilde{\mu}_\alpha^{\pm, \text{I/II}}$ in each phase, and the phase volumes $V^{\text{I/II}}$. The latter can be expressed again in terms of conserved densities $\bar{\psi}_i$, see Eq. 1.7. Therefore, the non-equilibrium steady state at phase equilibrium for a given system is still uniquely defined by knowing the average values of conserved quantities. Instead of the conditions for thermodynamic equilibrium stated in Eq. 1.43, we can define the conditions for non-equilibrium steady states for a system with M non-solvent components and L' linearly independent reactions at phase equilibrium via

$$\begin{aligned} \bullet \text{ phase equilibrium}^6: \mu_i^{\text{I}} &= \mu_i^{\text{II}}, & M + 1 \\ \bullet \text{ stationarity conditons: } \Delta\mu_\alpha^{\text{I/II}} &= \Delta\mu_\alpha^{\text{NESS}}, & L' \\ \bullet \text{ conservation laws: } \frac{\bar{\psi}_i - \psi_i^{\text{II}}}{\psi_i^{\text{I}} - \psi_i^{\text{II}}} &= \frac{\bar{\psi}_j - \psi_j^{\text{II}}}{\psi_j^{\text{I}} - \psi_j^{\text{II}}}, & M - L' - 1 \end{aligned} \quad \underline{\underline{2M}} \quad (2.12)$$

Therefore, we have found again $2M$ conditions for the $2M$ unknown volume fractions at steady state. Note, the stationary conditions are simultaneously fulfilled in both phases, I and II, due to phase equilibrium.

2.2.2 The tie line selecting manifold

In the introduction, we showed how the conditions of phase equilibrium, chemical equilibrium, and the combination of both, thus thermodynamic equilibrium, can be represented in composition space. Analogously, we will show conditions of a non-equilibrium steady state at phase equilibrium in composition space. In a passive system, the intersections between the chemical equilibrium line (manifold) and the binodal line (manifold) are necessarily connected via tie lines, see FIG. 1.3 and FIG. 1.4. However, these intersections between the two equilibrium lines (manifolds) are no longer connected via tie lines for phase-specific chemical driving. Nevertheless, the fact that we can express the conditions in Eq. 2.12 without solving for V^{I} and V^{II} explicitly⁷ means that we can still draw a classical phase diagram for the volume fractions at the non-equilibrium steady state.

For doing this, additional information is needed to identify which tie line gets selected in the non-equilibrium steady state at phase equilibrium. Therefore, we introduce the tie line selecting manifold, which translates between conserved quantities

⁶These constraints are given in the Gibbs ensemble. In the Helmholtz ensemble, we obtain M constraints from balancing the exchange chemical potentials $\tilde{\mu}_i^{\text{I/II}}$ and the osmotic pressure condition.

⁷However, when knowing the values of $\psi^{\text{I/II}}$, they are immediately given via Eq. 1.44.

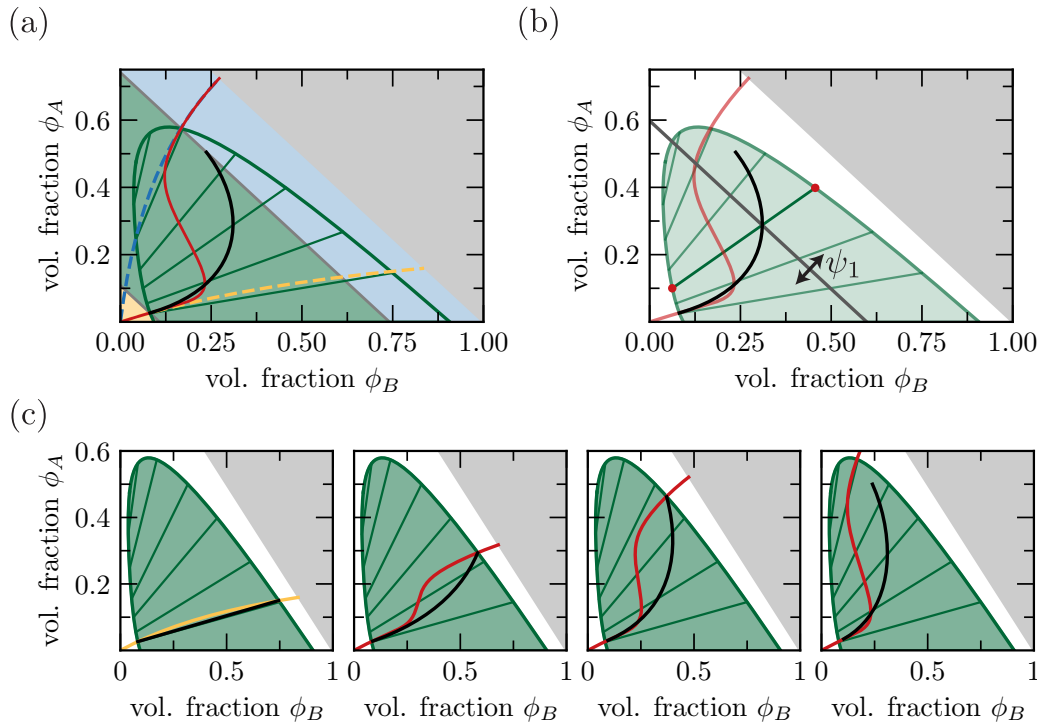


FIGURE 2.4: **Tie line selecting curve:** The binodal line (thick green) and the tie lines (thin green) denote phase equilibrium in all figures. Two chemical equilibria lines, compatible with thermodynamic equilibrium situations, are shown in Fig. (a) (blue and yellow dashed). An equilibrium situation can describe systems with well-mixed steady states (blue and yellow shaded areas). However, with phase-specific driving, we obtain the red chemical equilibrium line. Systems with coexisting phases at steady state (green shaded area) can not be at equilibrium—a non-equilibrium steady state at phase equilibrium but away from chemical equilibrium results. The tie line selecting curve (black) depicts which phase equilibrium along the binodal line is chosen. Fig. (b) shows how this curve translates from specific conserved quantities $\psi = \phi_A + \phi_B$ to the selected phase equilibrium. The latter is captured by the tie line, which runs through the intersection point of the conservation line (grey) and the tie line selecting curve. Tie line selecting curves for different driving strengths are shown in Fig. (c). When the system is not driven phase-specifically, the tie line selecting curve collapses to the tie line compatible with equilibrium (first plot). For the parameters, see App. C.

and volume fractions. This manifold summarizes the conditions of phase equilibrium and stationarity conditions while conservation laws still constrain the system on a subspace of the composition space. The non-equilibrium steady state can now be depicted as the intersection between the manifolds of conserved quantity and the tie line selecting manifold. It is defined by the average volume fractions $\bar{\phi}_i$ at steady state given specific values of conserved quantity and solving Eq. 2.12.

To illustrate this, we show in FIG. 2.4(a) the phase diagram of ternary mixture composed out of A , B and a solvent S with the driven chemical reaction $A \rightleftharpoons B$. The thick green line is the binodal line, while thin green lines are a set of tie lines. Additionally, we show two chemical equilibrium lines compatible with an equilibrium system as blue and yellow dashed. Both the intersection points of both of these lines are connected via a tie line. However, we drive the system phase-specific. Far below a certain value of the conserved quantity $\psi = \phi_A + \phi_B$, a well-mixed system would

follow the yellow chemical equilibrium line, while far above it would follow the blue chemical equilibrium line. However, due to the phase-specific driving, no tie line connects the intersections between the red chemical equilibrium line and the binodal line⁸. Thus, this system is active. However, we can depict the non-equilibrium steady state by introducing the tie line selecting curve in black. This non-equilibrium steady state depends on the conserved quantity ψ . We show in FIG. 2.4(b) how the tie line selecting curve allows identifying the non-equilibrium steady state. The conservation line for a given value of the conserved quantity ψ intersects the tie line selecting curve at one point. The tie line which runs through this intersection point depicts the non-equilibrium steady state. Therefore, we can colorize the areas in FIG. 2.4(a). The steady state is well-mixed in the yellow/blue shaded area and follows the yellow/blue chemical equilibrium curve. An effective equilibrium situation can describe these systems. However, a non-equilibrium steady state of coexisting phases exists in the green area. In this state, constant chemical reactions occur in the phases, balanced by a constant diffusive exchange between phases. In FIG. 2.4(c), we show the tie line selecting curve for different driving strength. If the system is passive (first case), the tie line selecting curve is identical to the selected tie line selected by the two intersections of the binodal line and the chemical equilibrium line. Whenever the system is phase-specific driven, the non-equilibrium state becomes dependent on the conserved quantity and a non-trivial tie line selecting curve occurs.

2.3 Discussion

In this chapter, we have studied chemical reactions in systems compartmentalized by phase separation. The central assumption is the limit of infinitely fast diffusion. Therefore, coexisting phases build homogeneous compartments that are at phase equilibrium at all times. Consequently, ordinary differential equations, namely Eq. 2.2 and Eq. 2.3, can describe the dynamics of their composition and sizes. This limit holds when chemical reactions are slow compared to the diffusive dynamics. This separation of time scales implies that the system size is smaller than the reaction-diffusion length scales, which are set by the reaction rate coefficients and the diffusion coefficients. Therefore, we want to highlight that this limit is not a hydrodynamic limit. On large length scales, chemical equilibrium will be reached faster than diffusive transport can equilibrate the spatial gradients of chemical potentials. However, first, this condition of a partial equilibrium holds in reaction-limited chemical kinetics also found in biology, see [52, 53]. Especially for small droplets, diffusion is sufficiently fast. Second, as we will see in the following chapters, the hydrodynamic limit can not be performed easily for actively driven systems. Therefore, it is convenient to have a well-defined limit, in which the non-equilibrium steady state is known and well-defined by Eq. 2.12.

⁸In this case, we have chosen $\Delta\bar{\mu}$ to be dependent on ψ . This leads to the smooth interpolation inside the binodal.

Chapter 3

Dynamics of concentration fields in phase-separating systems with chemical reactions

The previous chapter discussed chemical reactions in compartments formed by phase separation. These compartments are considered to be homogeneous and at phase equilibrium at all time points. This is the limiting case with fast diffusion compared to the rate of chemical reactions in finite systems. When chemical reactions occur on time scales, that diffusion needs to equilibrate chemical potentials on the relevant length scales, spatial gradients arise. For studying such systems, this chapter discusses chemical reactions in phase-separating systems with local variables in space, thus concentration fields. We introduce partial differential equations for describing reaction and diffusion processes, valid for non-dilute mixtures capable of phase separation.

After introducing the governing equations, we first discuss the circumstances under which the assumptions for homogeneous phases at phase equilibrium hold. We compare the relaxation dynamics toward equilibrium in passive systems and the relaxation towards a non-equilibrium steady state for driven systems to the dynamics derived in Chap. 2. Second, with the spatial dynamics at hand, we investigate systems where the chemical reactions can equilibrate locally towards their equilibrium, while diffusion is not fast enough to equilibrate the concentrations in space. Thus, gradients emerge.

These gradients also exist at the steady state when the system is maintained away from equilibrium, either by driving chemical reactions specific in some phases, similarly as done in Chap. 2, or by organizing chemical reactions inside phases and driving the system away from equilibrium via reservoirs at the boundaries of the system. The first breaks detailed balance of the rates only for chemical reactions, while the second only breaks detailed balance at the boundaries. Nevertheless, in both circumstances, the droplet dynamics changes compared to the nucleation-and-growth or ripening behavior of equilibrium systems. This, we discuss at the end of this chapter.

3.1 Reaction-diffusion equations for phase separating systems

Already in 1951, Alan Turing proposed that the pattern formation obtained from the interplay of chemical reaction and diffusion is a key mechanism for morphogenesis [54]. However, due to the generality of these concepts, they are not only used for modeling chemical reactions in spatial systems but are applied in many different fields. Examples are given by population dynamics, spreading of viruses and models of skin pigmentation, see [55, 9, 56].

However, the classical reaction-diffusion equations are valid only for dilute mixtures. Fick's law of diffusion then describes the spatial transport and mass-action laws with chemical reaction fluxes proportional to concentrations to the power of the stoichiometric coefficients describe the chemical reaction kinetics. The dynamics of systems with coexisting phases, however, can not be described with these equations.

Nevertheless, in the introduction of this work, we derived the dynamics of these processes from the minimization of a free energy. The reaction kinetics of homogeneous mixtures Eq. 1.38 can be applied locally. Thus, together with Eq. 1.8, we obtain

$$\partial_t \phi_i = -\nabla \cdot \mathbf{j}_i + r_i \quad , \quad (3.1)$$

with the spatial fluxes \mathbf{j}_i and the source or sink terms r_i stated in Eq. 1.39 and evaluated locally. We conclude

$$\partial_t \phi_i = \sum_{j=1}^M \nu_i \nabla \Gamma_{ij} \nabla \bar{\mu}_j + \sum_{\alpha=1}^L k_\alpha \sigma_{i\alpha} \nu_i \left(\exp \left(\frac{\mu_\alpha^+}{k_B T} \right) - \exp \left(\frac{\mu_\alpha^-}{k_B T} \right) \right) \quad . \quad (3.2)$$

The forward and backward chemical reaction energies μ_α^\pm are given by Eq. 1.30 in passive systems. For active driving of chemical reactions, we use Eq. 1.46. Here, the supplied chemical energy $\Delta \tilde{\mu}_\alpha$ can be composition dependent. Equation 3.2 is the governing equation of phase separating systems with chemical reactions. In general, it is a fourth-order non-linear partial differential equation. This equation can be reduced to the classical reaction-diffusion equations for dilute mixtures. Then, the diffusive fluxes lead to Fick's diffusion law, while the chemical reaction kinetics relaxes towards classical mass-action laws. However, for systems with molecular interactions of particles, non-linearities arise in the diffusion terms and in the reaction terms. Therefore, the same non-linearities that lead to phase separation make the reaction rates necessarily non-linear, even for unimolecular reactions like $A \rightleftharpoons B$.

In Eq. 3.2, several length-scales exist. First, the coefficients of the gradient terms in the free energy κ_i define, together with the mobility coefficients Γ_{ij} , the length scales of the interfaces of droplets, as in phase-separating systems without reactions. Furthermore, similar to classical reaction-diffusion equations, the combination of diffusion and chemical reactions set length scales. However, due to these non-linearities,

the reaction-diffusion length scales λ_{RD} can be defined only by linearizing Eq. 3.2. Note that even for constant kinetic coefficients and the choice of the mobility matrix given in Eq. 1.10, the reaction-diffusion length scales differ between the two phases. We can express, for example, the inverse of the reaction-diffusion length scale λ_{RD} for a unimolecular reaction $A \rightleftharpoons B$ as

$$\lambda_{RD}^{-1} = \sqrt{\frac{k}{\Gamma}} \sqrt{\bar{\gamma}_A \exp\left(\frac{\omega_A}{k_B T}\right) + \bar{\gamma}_B \exp\left(\frac{\omega_B}{k_B T}\right)} . \quad (3.3)$$

However, at phase equilibrium, $\bar{\gamma}_i^I \phi_i^I = \bar{\gamma}_i^II \phi_i^II$, therefore $\bar{\gamma}_i^I \neq \bar{\gamma}_i^II$, when the reacting molecules partition. Therefore λ_{RD}^{-1} becomes phase dependent.

3.2 Relaxation towards thermodynamic equilibrium in spatial systems

Local chemical reactions and spatial transport via diffusion occur in the relaxation kinetics towards equilibrium. This equilibrium is defined when both processes are at their equilibrium state. However, the relaxation rate of these processes can differ. Thus, the relaxation kinetics changes. We discuss this relaxation kinetics by using the same ternary mixture as done in Chap. 2. First, we assume fast diffusion, such that length scale and time scale separate, leading to the limit discussed in the previous chapter. We compare the dynamics of the spatial system to those derived in Chap. 2 by initializing a system in a well-mixed state outside the binodal area and away from chemical equilibrium (initial condition 1 in FIG. 2.1(a)) and solve Eq. 3.1 numerically in a two-dimensional system. Second, we show the differences arising when systems relax towards thermodynamic equilibrium in the presence of spatial gradients, when reactions are fast compared to diffusion. For this, we initialize a system with two homogeneous phases at phase equilibrium but away from chemical equilibrium (initial condition 2 in FIG. 2.1(a)).

3.2.1 Relaxation kinetics and fast diffusion

In FIG. 3.1, we compare the time evolution of the spatial system with the kinetics of homogeneous phases at phase equilibrium¹. Therefore, we again use an exemplary ternary mixture of components A , B , and S and allow the chemical reaction $A \rightleftharpoons B$. For the specific choice of parameters used for generating FIG. 3.1, the reaction-diffusion length scales, linearized around the thermodynamic equilibrium are $\lambda_{RD}^I = 0.60L$ in the B -rich phase I, and $\lambda_{RD}^{II} = 0.37L$ in phase II, where L is the system size.

¹Please note, in Chap. 2, we used the Gibbs Ensemble. For incompressible systems with volume-conserving reactions, this is equivalent to the corresponding Helmholtz ensemble used in the rest of the thesis. However, by changing the ensemble, a prefactor in k_α arises. Other than that, both ensembles are equivalent.

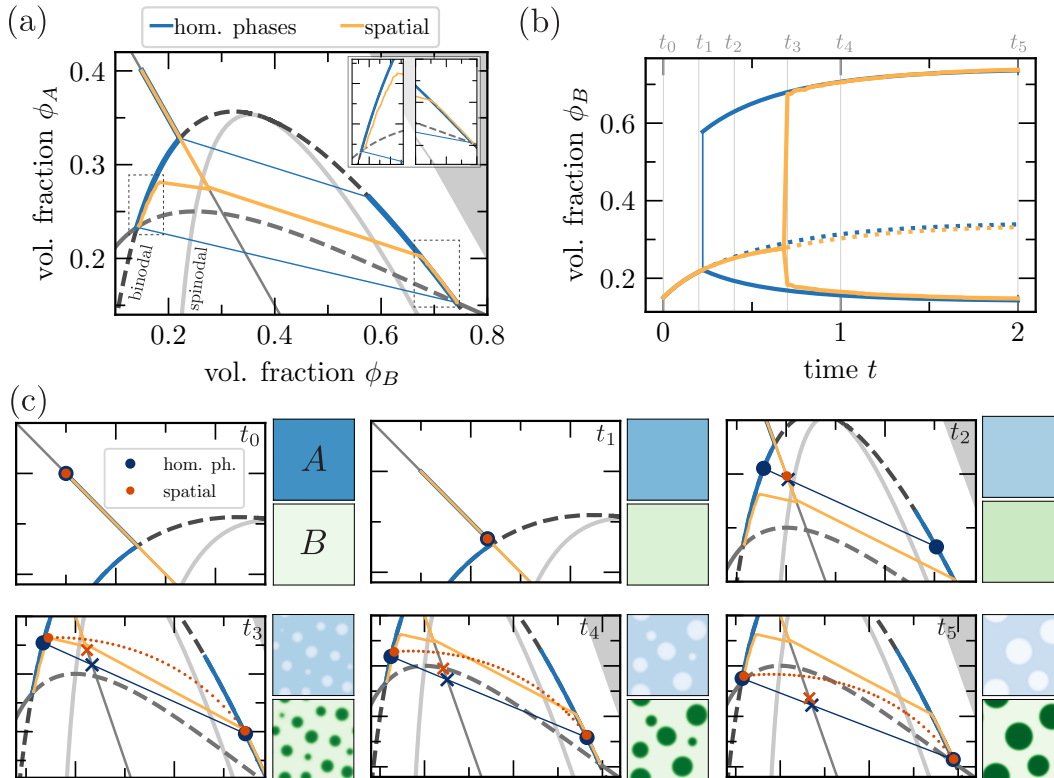


FIGURE 3.1: **Relaxation dynamics with instantaneous phases equilibrium vs. spatial systems with fast diffusion:** (a): The binodal (dark grey dashed), spinodal (light grey solid), and the chemical equilibrium line (thick grey - solid for equilibria state, dashed for otherwise) are shown, together with the line of conserved quantity (dark thin grey) used in the system. The reaction kinetics for two homogeneous phases at phase equilibrium (blue) and the composition of the bulk phases in a 2D spatial system (yellow) are shown as trajectories in composition space. The insets show a zoom of the dynamics in the phase-separated area. (b) Vol. fraction ϕ_B as a function of time is shown. The dotted line indicates the systems' average. (c): For six time points, volume fraction fields of A and B are shown on the right as spatial density plots, and on the left in composition space. These time points are indicated by vertical grey lines in (b). The dark blue points correspond to the volume fraction values under the dynamics for homogeneous phases. The orange points are constructed by binning the 2D composition space. The larger points are the averaged composition in the one/two (homogeneous/phase-separated state) bins with the highest counts, representing the bulk phases. Their dynamical evolution is shown in the yellow line. The small points correspond to all other bins with non-zero count, representing the interface values (for the non-monotonic form, see App. B). The x indicates the system average. For further details and parameters, see App. C.

The single droplets, and the inter-droplet distance, however, are much smaller than these length scales as long as the system is far away from chemical equilibrium. Therefore, the limit of fast diffusion compared to chemical reactions is valid.

Figure 3.1(a) shows, in addition to the phase diagram of the system without chemical reactions, the trajectories of the volume fractions in the composition space. We initialize the system outside the binodal line. Thus, the system is homogeneous and follows the conservation line ($\psi = 0.42$). Here, A gets converted into B , which leads to the enrichment of the latter over time, see FIG. 3.1(b) from t_0 to t_1 . These values, similarly to the trajectories shown in FIG. 2.1(a), can be directly obtained from the

dynamics of chemical reactions in compartments. We bin the volume fraction fields in the composition space for the spatial system by sorting every grid point (used for the numerical simulation) into a bin in the 2D composition space. In these early dynamics, the system is homogeneous (see the density plots FIG. 2.1(c)), and only one bin has a non-zero count. Its average composition is shown in with the yellow lines in FIG. 2.1(a),(b).

Around t_1 , the systems reach the binodal line. With the assumption of instantaneous phase equilibrium at all times, two homogeneous compartments are formed in the system with infinite diffusion. However, the homogeneous state in the spatial system is still locally stable. Therefore, it does not undergo spontaneous demixing (see FIG. 2.1(c) at t_2). The homogeneous phase becomes unstable only when the system reaches the spinodal line (shown in FIG. 3.1(a),(c)²). This happens shortly before t_3 . Here, the spatial system undergoes a spinodal decomposition, and droplets are formed. Due to the large reaction-diffusion length scales, these phases are almost homogeneous. The average of the two bins with the highest counts (representing the two bulk phases) are shown in the FIG. 3.1(a),(b) from thereon. In FIG. 3.1(c), we show these points by the larger orange points in the composition space. The smaller points are the average values of all the bins with a non-zero count, stemming from the interface between the two phases. These points follow a curve that minimizes the free energy of the interface, see App. B. In the dynamics, the bulk phases in the spatial system follow the binodal line closely from thereon. However, a small deviation can be seen, which declines over time (see the insets in FIG. 3.1(a)). This deviation stems from the Laplace pressure, which shifts the equilibrium values in finite two- or three-dimensional systems. These deviations get smaller during the dynamics because droplets ripen (see FIG. 3.1(c)) and reduce their average curvature. The wiggling seen in these curves results from the dissolution of tiny droplets. However, the average of the spatial system has gained a time lag, when compared with the homogenous one (see the shift of the blue and orange points and x's in the composition space in FIG. 3.1(c) $t_3 - t_5$). The reason for this lag is the fact that the reaction free energy $\Delta\mu^{\text{mix}}$ of the well-mixed state is smaller than the reaction free energy $\Delta\mu^{\text{I/II}}$ during this time evolution. Thus, the reaction is slower. However, in real systems or stochastic descriptions of Eq. 3.1, nucleation can happen due to fluctuations, and thus, the demixing would occur earlier.

3.2.2 Relaxation kinetics with spatial gradients

So far, we have chosen reaction rates k_α such that diffusion was much faster than chemical reactions on the length scales relevant to the droplets. However, we can also investigate how systems relax towards the thermodynamic equilibrium when diffusion is slow. For this, we initialize two phases at phase equilibrium but away

²We compute here the spinodal line for the system without chemical reactions. In general, the presence of chemical reactions can change stability. This can partially explain the delay between the onset of phase separation, seen in the FIG. 3.1(a), and the reaching of the spinodal line. Furthermore, the spatial system is almost perfectly homogeneous due to the dynamics up to that point. Therefore, the numerical variation of the fields is small.

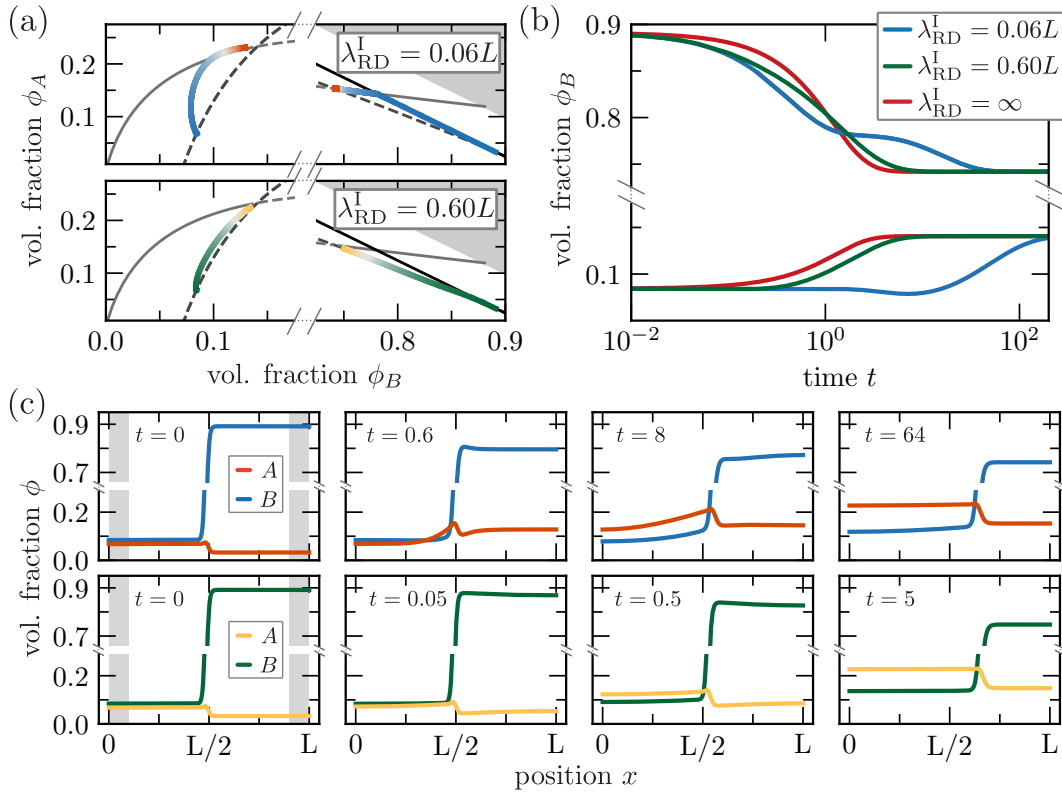


FIGURE 3.2: **Relaxation dynamics - slow and intermediate diffusion:** (a): Corners of the composition space, together with the binodal (dashed dark grey), and the chemical equilibrium line (solid light grey) are displayed. The trajectory of the relaxation kinetics stays closer to the binodal line the faster diffusion gets: slow diffusion in the upper row, intermediate diffusion in the lower row in a 1D system of length L . These trajectories are obtained by following the average compositions in the grey area in the first plot of (c) over time. Time is encoded in the color code (from blue/green to red/yellow). The conservation line in phase I is shown in (a) as a thin black line. (b): The dynamical evolution of ϕ_B in the case of homogeneous phases at instantaneous (infinite diffusivity) phase equilibrium (red), intermediate diffusion (green), and slow diffusion (blue) is shown. (c): The spatial profiles of these systems at different time points are shown: upper row - slow diffusion, lower row - intermediate diffusion. For further details and parameter, see App. C.

from chemical equilibrium in a spatial 1D system (initial condition 2 in FIG. 2.1(a)). Furthermore, the chemical reaction occurs only in the B -rich phase I. This is achieved by choosing $k \propto k^I \text{sig}((\phi_B - \phi_B^{\text{crit}})/\omega)$, with $\text{sig}(x) = (1 + \tanh(x))/2$, thus $\lambda_{RD}^{\text{II}} = \infty$. In FIG. 3.2, we compare the chemical kinetics in homogeneous phases with the dynamics in two spatial systems with different values of the mobility coefficients. The parameters are chosen such that $\lambda_{RD}^I = 0.06L$ for the first case, and $\lambda_{RD}^I = 0.60L$ in the second case. In the beginning, both phases occupy roughly half the system size (see FIG. 3.2(c) the first column). Thus, phase I is almost ten times bigger than the reaction-diffusion length scale for the first case and in the same order of magnitude as the second case's reaction-diffusion length scale. For the first case, the volume fraction values far away from the interface can thereby be altered by chemical reactions faster than diffusion can maintain phase equilibrium in space. To visualize this, we plot these values (the mean over the grey areas depicted in the first column of FIG. 3.2(c) respectively) in the composition space in FIG. 3.2(a) (see FIG. 3.1(a)

for the full phase diagram) and against time in FIG. 3.2(b). The temporal evolution is encoded in a linear colormap in FIG. 3.2(a). For the first case (upper row), these values do not follow the binodal line. In phase I, chemical reactions will equilibrate locally, and the trajectory follows the conservation line of the locally conserved quantity (black line) until it reaches the chemical equilibrium line (light grey line). From thereon, it relaxes along this chemical equilibrium line to phase equilibrium. This leads to two different time regimes, see FIG. 3.2(b)) (blue line). Until $t \approx 1$, the composition relaxes locally to a chemical equilibrium in phase I, while the composition in phase II stays constant due to the absence of chemical reactions. Only in the second time regime ($t > 5$) does diffusion slowly exchange material until phase equilibrium is finally reached between the phases.

For the second case the trajectory stays much closer to the binodal line (see the second row in FIG. 3.2(a)). Also, in time, the dynamics is similar to the chemical kinetics of two homogeneous phases at phase equilibrium (compare the red and green curves in FIG. 3.2(b)). As expected from the reaction-diffusion length scales, the spatial gradients are almost negligible in this case (see FIG. 3.2(c)). Even in the absence of chemical reactions in phase II, diffusion couples the composition of both phases such that chemical and phase equilibria are approached on similar time scales.

Furthermore, FIG. 3.2(c) reveals that also the interface length scale is affected by the composition (compare the initial and the final interface widths for both cases). This is related to the change of surface tension for different phase equilibria in a ternary mixture, see App. B.

In general, passive phase separating systems with chemical reactions have two processes by which they can reach equilibrium. In the limit that diffusion is much faster than reactions, we can describe the relaxation by the theory developed in the previous chapter. However, some local stabilities during the transients and the Laplace pressure in finite systems can alter the dynamics slightly for spatial systems. In the other limit, local chemical equilibrium is reached, and diffusion slowly equilibrates the phases. In these systems, droplets ripen and their equilibrium is governed by Eq. 1.43 at which diffusive and chemical fluxes vanish.

3.3 Driven chemical reactions in phase-separating systems

As seen already in the previous chapter, phase-separating systems with driven chemical reactions are active when chemical reactions are driven differently in phases. In Section 2.2 we studied the non-equilibrium steady states for fast diffusion. Similarly, in spatial systems, when the diffusion-reaction length scale is larger than the system size, the non-equilibrium steady states are determined by Eq. 2.12. Like the equilibrium case, only single droplets exist at the steady state. However, when this hierarchy of length scales is not given, spatial gradients occur. Due to the chemical reactions, finite length scales appear, which set, in general, limits to the droplet sizes and can lead to stable states of multiple droplets. Therefore, the ripening can be suppressed, and droplets can deform in non-spherical states and even divide.

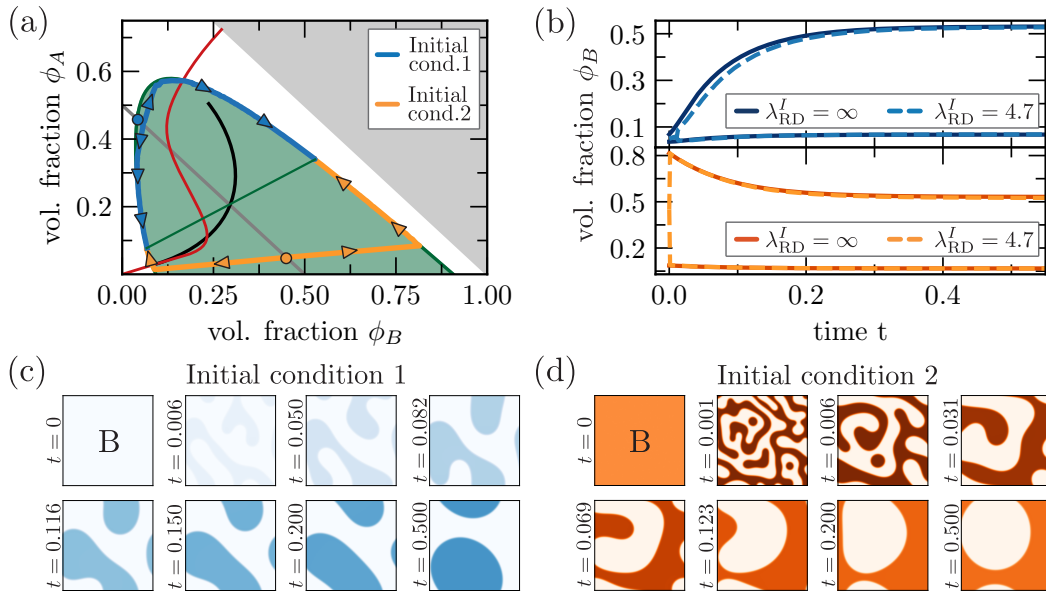


FIGURE 3.3: **Phase-specific driving and fast diffusion:** (a): The binodal (thick green), the effective chemical equilibrium line (red), a conservation line (grey), the tie-line selecting curve (black), and the selected tie-line (green) are shown. Furthermore, we display two trajectories (blue and orange lines) of the bulk phases in 2D spatial systems with fast diffusion for different initial conditions (blue and orange dots) but the conserved quantity as indicated with the conservation line. (b): The temporal evolution of the corresponding ϕ_B values as a function of time (dashed lines), together with the dynamics for homogeneous phases at phase equilibrium (solid line), is shown. (c): Density plots of ϕ_B in space for eight time points each are shown. For further details and parameters, see App. C.

These aspects have been studied in the literature mainly for binary systems, see [18, 19, 20]. However, some of the aspects have been already reported for multi-component mixtures recently, see [57, 58, 59]. Here, we start our discussion with the case of fast diffusion. In this limit, the non-equilibrium steady state is uniquely defined by Eq. 2.12. In the later part of this section, we discuss non-equilibrium states with spatial gradients and the dynamics for systems with finite diffusivities.

3.3.1 Driven chemical reaction and fast diffusion

As mentioned above, Chap. 2 discusses the chemical kinetics and non-equilibrium steady states for systems with phase-dependent chemical driving. The stationary states of chemical reactions are not compatible with phase equilibrium, which is maintained via diffusive exchanges instantaneously. Thus, no equilibrium can be found in such systems, but a unique non-equilibrium steady state is reached for simple reaction schemes. It is determined by Eq. 2.12. In FIG. 2.4, we show the tie line selecting curve and the phase diagram of a ternary mixture A , B , and S with the chemical reaction $A \rightleftharpoons B$.

Here, we compare the dynamics of spatial systems to those of two phases at phase equilibrium for this ternary mixture. To this end, two different conditions of compositions in ϕ_A and ϕ_B but with the identical value of the conserved quantity $\psi =$

$\phi_A + \phi_B$ are initialized. Despite being a spatial system, we chose chemical coefficients such that diffusion is fast compared to the chemical reactions on the system size length scale L ($\lambda_{RD}^I = 4.7L$). In FIG. 3.3(a), the binodal line (thick dark green), the effective chemical equilibrium line (red), the line of conserved quantity $\psi = 0.5$ (grey line), the tie line selecting curve (black), and the for this conserved quantity selected tie line is shown (thin dark green). Again, the dynamics of the two spatial systems are depicted in composition space (blue and orange lines). Therefore, the volume fractions fields are binned, and the mean of the two bins with the highest counts for bins above and below the average value of the conserved quantity are depicted. These values are a good proxy for the average composition in the two phases, away from the interface. After a fast spinodal decomposition, these two average compositions follow the binodal line again almost perfectly until they reach the values connected by the selected tie line resulting from the assumption of homogeneous phases at phase equilibrium.

Furthermore, these two average compositions match the chemical kinetics of two phases at phase equilibrium when shown versus time, see FIG. 3.3(b). Only the time needed for the spinodal decomposition leads to a slight offset because the chemical reaction fluxes are smaller for the well-mixed state. This shift is most dominant for initial condition 1 (upper row) because the system is initialized close to the critical point, leading to slower time scales of the spinodal decomposition. In FIG. 3.3(c), we show snapshots of the volume fraction field B for designated time points. The spinodal decomposition and the ripening of the resulting structures can be seen. Both systems form a single droplet in the steady state. The phase volume and the composition of these almost homogeneous phases are close to those predicted by the tie line selecting curve. This ripening occurs in the presence of a slow production of B material for initial condition 1 and slow degradation of B material for initial condition 2. Therefore, for systems with large reaction-diffusion length scales compared to the system size, which itself is much larger than the interface width, only the total volumes of each phase become the important variables. If these phase volumes are composed of many tiny droplets or just one big droplet is not resolved, and ripening will always lead to the latter state. The initial condition is therefore irrelevant for the non-equilibrium steady state.

3.3.2 Non-equilibrium steady states and spatial gradients

When the separation of length scales is not given, thus reaction-diffusion length scales are smaller than the system size, spatial gradients can occur. These gradients exist even at the steady state. Locally, the driven chemical reactions try to relax towards their effective chemical equilibrium. However, these chemical equilibria differ between the phases such that no phase equilibrium can be reached. Nevertheless, diffusion equilibrates the chemical potential profiles locally.

We illustrate this in FIG. 3.4. Here, we initialize a one-dimensional system at the steady state for two homogeneous phases at phase equilibrium. Then, we solve Eq. 3.1 numerically for different values of the mobility coefficient until a steady

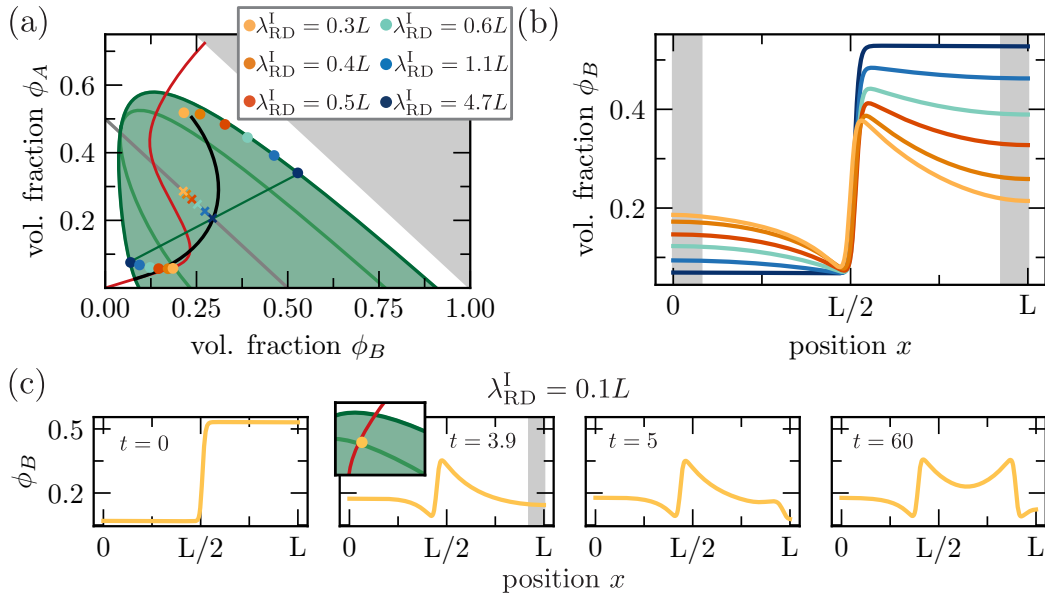


FIGURE 3.4: Non-equilibrium steady states for different kinetic coefficients: The binodal (thick green), the spinodal (light green), the effective chemical equilibrium line (red), a conservation line (grey), the tie-line selecting curve (black), and the selected tie-line (green) are shown in (a). Furthermore, we plot the average volume fractions deep inside the phases (grey area in (b)) of a 1D system at steady state for different kinetic coefficients (colored dots) and the conserved quantity shown in (a). The average of these systems is denoted by x . The steady state profiles of ϕ_B for these systems are shown in (b). In (c), we show the ϕ_B values for four different time points in a system with $\lambda_{\text{RD}}^{\text{I}} = 0.1L$. In the inset of the second plot, the volume fractions deep in phase I (average over grey area) are shown in composition space, touching the spinodal line. For further details and parameters, see App. C.

state is reached. The profile of the B component volume fraction ϕ_B , is depicted in FIG. 3.4(b). The smaller the reaction-diffusion length scale is, the stronger the spatial gradients become. Furthermore, different values at the interface are selected between the different cases. We show the average composition from the grey area in FIG. 3.4(a) in the composition space in FIG. 3.4(a). These values lie only on the binodal line (dark green) and are connected with a tie line for systems with large reaction-diffusion length scales, see the case of $\lambda_{\text{RD}}^{\text{I}} = 4.7$. With this, the phases are homogeneous and the tie line selecting curve depicts the average composition of the almost homogenous phases at the non-equilibrium steady state. However, when the reaction-diffusion length scales become smaller, the values deep in the phases do not lie on the binodal anymore, nor are they connected via a tie line. For $\lambda_{\text{RD}} < L$, the values deep within the phases come closer to the local chemical equilibrium. Dependent on the conserved quantities, the reaction-diffusion length (the smaller the reaction-diffusion length scales, the closer they come to the effective chemical equilibrium line, see FIG. 3.4(a)) and the local stability, the chemical equilibrium can be reached. In the system shown in FIG. 3.4, the local chemical equilibrium lies within the spinodal area (light green line) for the conserved quantity used in these systems ($\psi = 0.5$). When local volume fraction values reach the spinodal line, the system starts to build a new interface. Therefore, for such systems, the reaction-diffusion length scale, combined with the distance between the binodal and the spinodal line,

set a maximum droplet size. This can be seen in FIG. 3.4(c). For $\lambda_{\text{RD}}^{\text{I}} = 0.1L$, the composition deep within the B -rich phase reaches the spinodal point at $t \approx 4$ (see the zoom of the same phase diagram as in (a) in the inset). A second interface is formed (around $t = 5$), and the droplet slowly moves towards the center (the stationary state, not shown, is at the center of the system). This mechanism leads to finite length scales of phases for one-dimensional systems, for two-dimensional systems to rings, and in three-dimensional systems to spherical shells or tori.

In general, in systems where some reaction-diffusion length scales are significantly smaller than the system size, but the conserved quantities require total phase volumes larger than these length scales, complex dynamics of multiple droplets can arise. This, we study in the following.

3.3.3 Droplets growth and ripening with driven chemical reactions

For passive systems, we showed in Section 1.3 that the equilibrium is uniquely defined by Eq. 1.43, which only depends on the conserved quantities. This equilibrium is reached either by the constant growth of a single droplet in the nucleation-and-growth regime or by the ripening of many droplets after a spinodal decomposition, see Section 1.1.2. In Section 3.3.1, we studied already the dynamics of systems with driven chemical reactions towards the non-equilibrium steady state defined in Eq. 2.12 for systems with fast diffusion. Here, we show the droplet dynamics for systems with driven chemical reactions and finite diffusivities. Interestingly, by making the system active only in the chemical reactions, the dynamics of the conserved quantities also changes. Due to different interactions between components, the conserved quantities are coupled to the non-conserved variables, in general. Thus, although only maintaining the non-conserved reaction extent out of equilibrium, also the conserved quantities can not relax towards their equilibrium, and the droplet dynamics changes.

We illustrate this interplay again by a ternary mixture with components A , B , and S , where components A and B can chemically interconvert by the chemical reaction $A \rightleftharpoons B$. For simplicity we assume identical molecular volumes $\nu = \nu_i$ with $i = A, B, S$. We define the conserved quantity $\psi = \phi_A + \phi_B$ and the non-conserved one $\xi = \phi_B - \phi_A$. Following Eq. 3.1, Eq. 1.19 and Eq. 1.20 the dynamical equations for the conserved and non-conserved quantity read

$$\partial_t \psi = -\nabla \cdot \mathbf{j}_\psi \quad , \quad (3.4)$$

$$\partial_t \xi = -\nabla \cdot \mathbf{j}_\xi + r \quad , \quad (3.5)$$

where $\mathbf{j}_\psi = \mathbf{j}_A + \mathbf{j}_B$ is the flux of the conserved quantity, $\mathbf{j}_\xi = \mathbf{j}_B - \mathbf{j}_A$ is the flux of the non-conserved quantity, and $r = 2r_B$ the reaction source term of the reaction extent. At the steady state, \mathbf{j}_ψ must be zero³. However, this does not require $\nabla \psi$ or $\nabla \bar{\mu}_\psi$ with $\bar{\mu}_\psi = 1/2(\bar{\mu}_A + \bar{\mu}_B)$ to be zero, in general. From the stationarity of Eq. 3.4

³Strictly, it must be a constant which is then fixed by boundary conditions.

follows

$$\nabla\psi = -\frac{[(\chi_{AS} - \chi_{BS})\psi - \chi_{AB}\xi]\nabla\xi - \kappa/\nu(\psi\nabla^3\psi + \xi\nabla^3\xi)}{\frac{2k_B T}{\nu(1-\psi)} + [(\chi_{AB} - 2\chi_{AS} - 2\chi_{BS})\psi + (\chi_{AS} - \chi_{BS})\xi]} \quad (3.6)$$

when exchange chemical potentials of the form Eq. 1.2 and a mobility matrix of the form Eq. 1.10 are considered. Equation 3.6 reveals that, in general, a gradient in the conserved quantity ψ is an unavoidable consequence of a gradient of the non-conserved reaction extent ξ , even in the limit of $\kappa = 0$, thus a vanishing interface width. Therefore, when active driving of chemical reactions leads to spatial gradients of the non-conserved quantity ξ , the conserved quantity ψ is also kept away from equilibrium via the molecular interactions, in general. However, there are two special cases. One is the case where phase separation only occurs between the conserved quantity and the solvent. Second, the case where phase separation only occurs within the non-conserved quantity. We will start with these spatial cases and come to the general case of coupled dynamics at the end.

Phase separation of the conserved quantity from the solvent

When the components A and B have the same interaction parameters with the solvent, thus $\chi_{AS} = \chi_{BS}$, but do not interact with each other, thus $\chi_{AB} = 0$, the conserved quantity phase separates from the solvent independently from its specific composition in terms of ϕ_A and ϕ_B . With this, the numerator of Eq. 3.6 vanishes outside of the interface area related to the terms proportional to κ .

In FIG. 3.5(a), we show a phase diagram of such a system. The binodal lines (thick green) are parallel to the conservation lines (example given by the dark blue line with $\psi = 0.4$). Due to active driving from $B \rightarrow A$ in the solvent-rich phase, component B gets locally enriched compared to the solvent-poor phase. Therefore, the intersections of the chemical equilibrium line (red) with the binodal lines are not connected via a common tie line (thin green lines). In FIG. 3.5(c), we show the volume fraction profiles of ϕ_A and ϕ_B , as well as the related chemical potentials $\bar{\mu}_A$ and $\bar{\mu}_B$ of a stationary state in a one-dimensional system. Inside the droplet, chemical reactions try to equilibrate the chemical potentials. While in the outside phase, B material gets enriched due to active driving. Furthermore, we show the profiles of the conserved quantity ψ and the reaction extent ξ and the related chemical potentials in FIG. 3.5(d). Due to the symmetric choice of the interactions, the ψ -profile is constant inside the two phases, while ξ can vary in space. Here, the conserved quantity can reach an effective equilibrium, while the constantly ongoing chemical reactions only change the local composition of the conserved quantity. However, even for this symmetric choice, the chemical potentials of $\bar{\mu}_\psi$ and $\bar{\mu}_\xi$ show gradients due to a non-diagonal mobility matrix in the conserved/non-conserved ensemble. Furthermore, we show the volume fraction of component B at different time points in a two-dimensional system as density plots. We initialize the system homogeneously with $\psi = 0.4$. After a fast spinodal decomposition, tiny droplets are formed. Over time, these droplets ripen but display gradients of the volume fractions. Close

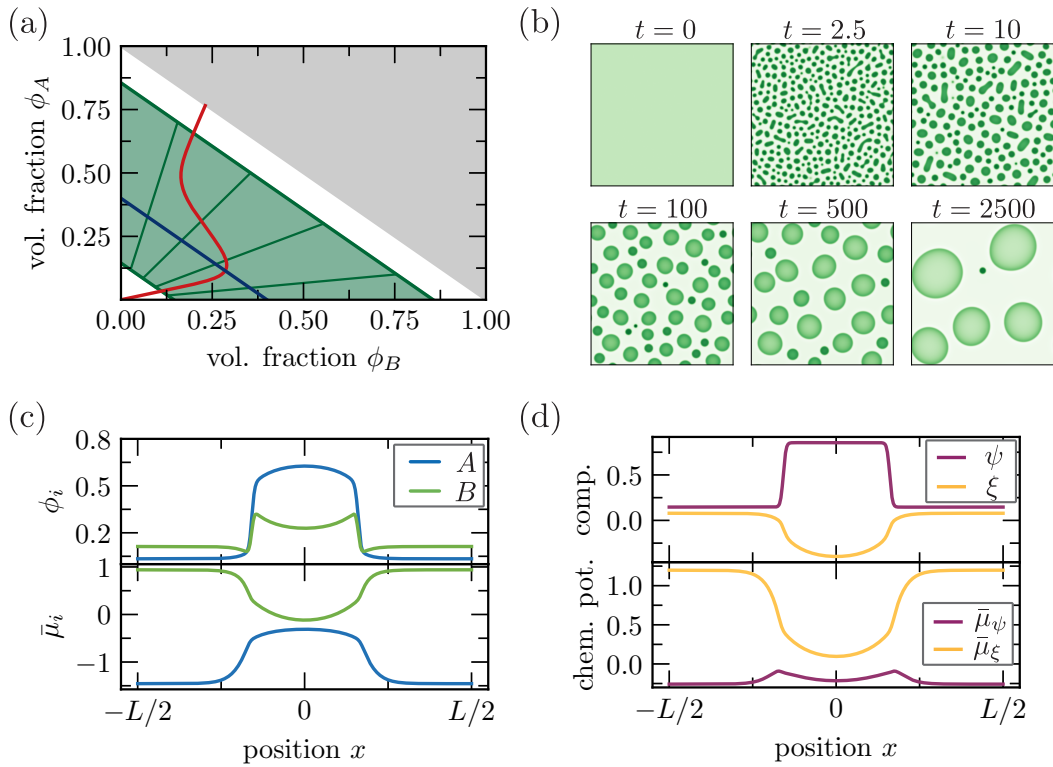


FIGURE 3.5: **Ripening of chemically active droplets:** The binodal line (thick green), some tie-lines (thin green), and the effective chemical equilibrium line are shown in (a). Density plots of the volume fraction profiles ϕ_B in a 2D system with the conserved quantity indicated by the blue line in (a) are shown in (b). We show the profiles of volume fractions (c), as well as the conserved quantity ψ and non-conserved quantity ξ (d), and their corresponding chemical potentials in the steady state of a 1D system with the same conserved quantity. see App. C.

to the interface, the B concentration is higher than deep within the droplets. Therefore, shortly before small droplets dissolve in the ripening process, they have a high concentration of B material due to the active enrichment of B in the other phase. Nevertheless, this driving does not affect the conserved quantity. Independent of how the conserved quantity is built up in terms of ϕ_A and ϕ_B , its interactions are always the same. Therefore, the dynamical equation of the conserved quantity - up to some slight changes in the interface region - decouples from the dynamics of the actively driven non-conserved reaction extent, and normal Ostwald ripening takes place. Thus, we can identify the conserved quantity as the only relevant variable in a hydrodynamic limit.

Phase separation within the non-conserved quantity

Another special case is when phase separation only occurs within the non-conserved quantities. In our ternary example, this means A only phase separates from B , leading to a high interaction parameter χ_{AB} , but their interactions with the solvent are identical, thus $\chi_{AS} = \chi_{BS}$. A phase diagram of such a situation is shown in FIG. 3.6(a). Here, the tie lines (thin green lines) are parallel to the conservation lines

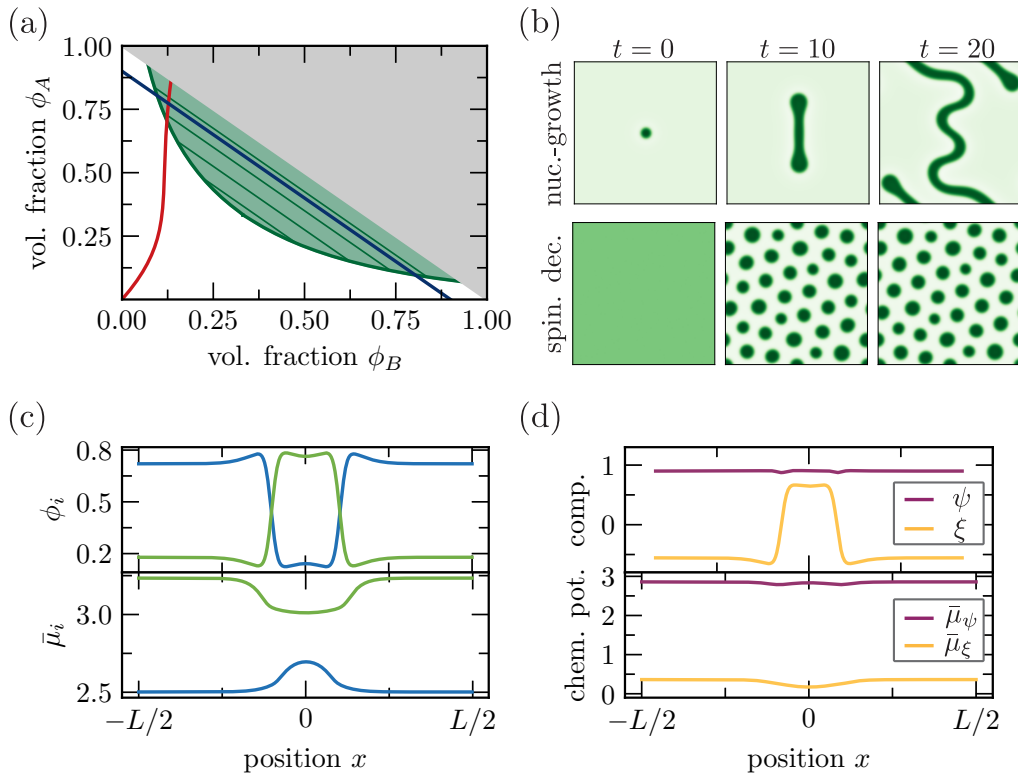


FIGURE 3.6: **Decoupled conserved and non-conserved variables:** The binodal line (thick green), some tie-lines (thin green), and the effective chemical equilibrium line are shown in (a). Density plots of the volume fraction profiles ϕ_B for two 2D systems with the conserved quantity indicated by the blue line in (a) are shown in (b). In the upper row, the system is initialized in the nucleation-and-growth regime, in the lower row inside the spinodal regime. We show the profiles of volume fractions (c), as well as the conserved quantity ψ and non-conserved quantity ξ (d), and their corresponding chemical potentials in the steady state of a 1D system with the same conserved quantity. For further details and parameters, see App. C.

(example given by the dark blue line with $\psi = 0.9$). However, due to the active driving, the chemical equilibrium line (red) intersects the binodal line (thick green) only at one point. For these interaction parameters and the reaction $A \rightleftharpoons B$, a passive system without driving can not have coexisting phases at equilibrium. Except for the degenerate case of $\omega_A = \omega_B$, where the chemical equilibrium line is the bisecting line of the first quadrant, the chemical equilibrium line can not intersect the binodal line without driving.⁴

Also, for this case, the conserved quantity decouples from the non-conserved reaction extent outside of the interface region. Again, the term $[(\chi_{AS} - \chi_{BS})\psi - \chi_{AB}\xi]\nabla\xi$ in the numerator of Eq. 3.6 vanishes, because when $\chi_{AS} = \chi_{BS}$, its dependency on ψ immediately disappears. Furthermore, the term proportional to $\xi\nabla\xi = 1/2\nabla\xi^2$. For these interactions, the absolute value of ξ is identical in the two phases, and only

⁴The physical argument here is identical to the binary case. Geometrically, this can be understood by considering the tangent construction of a binary mixture. Phase equilibrium is reached at the points of the common tangent. However, chemical equilibrium is reached at the absolute minimum of the free energy density.

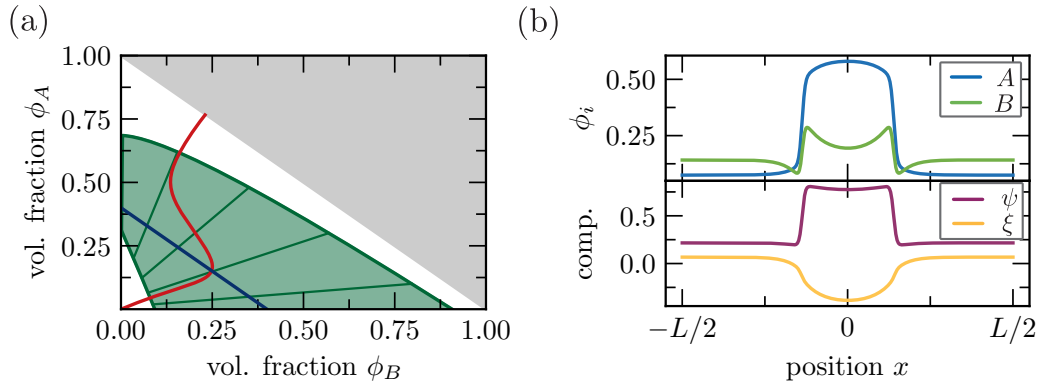


FIGURE 3.7: **Coupled conserved and non-conserved variables:** The binodal line (thick green), some tie-lines (thin green), and the effective chemical equilibrium line are shown in (a). We show the profiles of volume fractions (c), as well as the conserved quantity ψ and non-conserved quantity ξ (d), and their corresponding chemical potentials in the steady state of a 1D system with the same conserved quantity. For further details and parameters, see App. C.

its sign varies between the phases. Therefore, ξ^2 can be constant in space. Therefore, gradients of the non-conserved field do not cause gradients of the conserved field. In FIG. 3.6(c), we show the volume fraction profiles of ϕ_A and ϕ_B , as well as the related chemical potentials $\bar{\mu}_A$ and $\bar{\mu}_B$ of a stationary state in a one-dimensional system. Due to the phase-specific driving, gradients in both volume fractions occur, and the B -rich phase adapts to a size where the total loss of B material gets balanced by a flux from the B -poor phase through the interface. However, due to the symmetric interactions, the conserved quantity can reach a flat profile in the presence of a spatial variation of ξ , see FIG. 3.6(d).

This case is equivalent to a binary mixture. Here, droplets can become shape unstable [20], or Ostwald ripening can be suppressed [19]. The first happens in this system, when it is initialized in the nucleation-and-growth regime, see FIG. 3.6(b) (upper row). The second, when the system is initialized inside the spinodal regime FIG. 3.6(b) (lower row). Both behaviors differ clearly from the equilibrium dynamics shown in FIG. 1.2. However, due to the decoupling with the conserved variable, the dynamics of the non-conserved reaction extent is not constrained by the material conservation of ψ . This differs in the general case, which we will discuss next.

Coupling between the conserved quantity and the non-conserved quantity

After having discussed these special cases where the conserved quantity decouples from the non-conserved one, we come to the general case. Here, maintaining the reaction extent away from equilibrium via active chemical reactions also influences the conserved variable. To illustrate that and show its consequence, we slightly alter the interaction parameters of the first case of this section, such that $\chi_{AS} < \chi_{BS}$. Figure 3.7(a) shows the corresponding phase diagram of such a system. Different from the first example in FIG. 3.5, the binodal lines (dark green) are no longer parallel to the lines of a conserved quantity (example given by the dark blue line with $\psi = 0.4$).

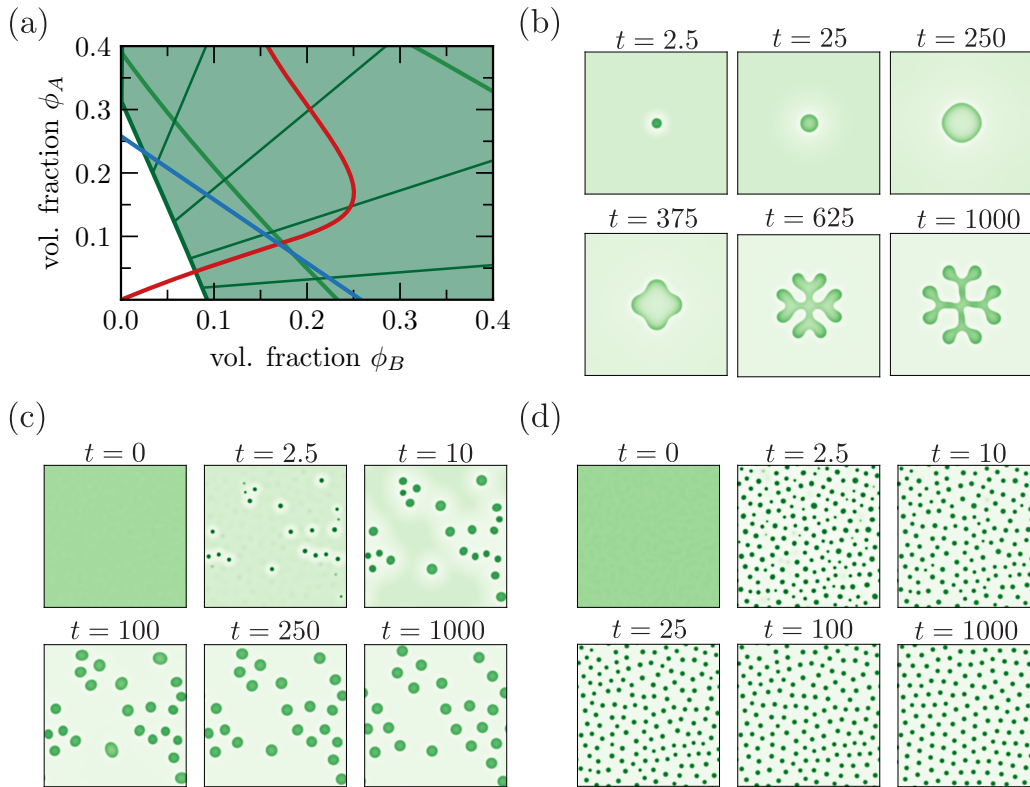


FIGURE 3.8: **Dynamics of coupled conserved and non-conserved variables:** The lower-left corner of the composition space, shown in FIG. 3.7(a), is displayed in (a). In addition to the binodal line (thick green), some tie-lines (thin green), the effective chemical equilibrium line (red), also the spinodal line (light green) is illustrated. The conservation line (blue) denotes the conserved quantity used in the three systems shown in (b-d). In (b), the density plots of ϕ_B in a 2D system at different time points are shown, nucleated in the nucleation-and-growth regime. Similarly, (c-d) show density plots of ϕ_B for systems initialized slightly within (c) or deep within (d) the spinodal regime. For further details and parameters, see App. C.

Even though the volume fraction profiles in FIG. 3.7(b) (upper panel) look similar to the profiles shown in FIG. 3.5(c), weak gradients of the conserved quantity appear at steady state, see FIG. 3.7(b) (lower panel). Thus, the active driving of the chemical reaction leads to spatial gradients of the conserved quantity due to the interaction between particles.

Therefore, the dynamics of the conserved quantity is coupled to the dynamics of the reaction extent and shows gradients in a stationary state. A further consequence of this is that droplets necessarily interact due to the conserved quantity. In contrast to the last special case, where droplets do not change the local amount of the conserved quantity and the formation of a new droplet somewhere in the system does not change the amount of conserved quantity in other areas far away, the local formation of a new droplet changes necessarily the amount of the available conserved material in other areas of the system.

To illustrate the effect of this competition, we initialize three different systems with the identical amount of conserved material and the exact same parameters, identical to those used for FIG. 3.7. We use systems with an average amount of conserved quantity, such that we can initialize them inside and outside of the spinodal area. In

FIG. 3.8(a), we show a zoomed-in version of FIG. 3.7(a), where the line of the average conserved quantity used in FIG. 3.8(b-d) is shown in dark blue, and the spinodal line in dark green. The intersection of the chemical equilibrium line (red) and the conservation line lies outside the spinodal area. Thus, the well-mixed state with the corresponding composition is meta-stable and lies in the nucleation-and-growth regime.

In FIG. 3.8(b), we initialize the system almost at this point, together with a small perturbation at the center. This perturbation leads to the nucleation of a B -rich, growing droplet. However, due to the active driving, B material gets enriched locally in the B -poor phase compared to the B -rich phase. Thus, when the droplet becomes large enough, the circular shape becomes unstable, and the droplet undergoes a shape instability. Thereby, four branches are formed, which split up several times until a non-equilibrium state is reached, at which no conserved material is available, which could lead to further growth. We study this shape instability in the next chapter.

In FIG. 3.8(c), we initialize the system slightly within the spinodal region such that several droplets are formed in some areas. Nevertheless, the meta-stable, local chemical equilibrium is reached in other areas. Again, these droplets grow but compete against conserved material, such that their size is limited. And finally, in FIG. 3.8(d), we initialize the system such that the full spinodal decomposition can take place. In both of the last two cases, ripening is suppressed, and droplets have the same size within the system. Furthermore, droplets position themselves. In FIG. 3.8(d), a lattice is formed. In FIG. 3.8(c), droplets move apart from each other. However, this positioning dynamic slows down dramatically. With this, disordered structures can become stationary over very long time scales. However, the droplet sizes differ vastly between FIG. 3.8(c) and FIG. 3.8(d), revealing that here, not the reaction-diffusion length scales but the competition over conserved material limits the growth of droplets.

3.4 Boundary driven chemically active droplets

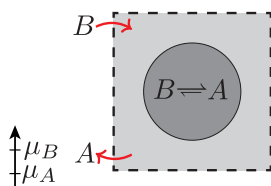


FIGURE 3.9

In the previous section, detailed balance of the rates was broken via an external supply of chemical energy. This section introduces another way of driving systems out of equilibrium when chemical reactions are organized by phase separation. Here, we couple the systems to particle baths at the system boundaries via concentration boundary conditions. Then, even when detailed balance is fulfilled everywhere in the bulk of the system, these reservoirs at the boundaries can drive fluxes. In the absence of chemical reactions, droplets would constantly grow or shrink in open systems. However, with chemical reactions organized only inside droplets, stationary chemically active droplets can exist. This is motivated by the idea that these reactions are enabled by catalysts that are only located inside one phase and are absent in the other. We model this by choosing

composition-dependent kinetic coefficients k_α , without breaking detailed balance of the rate. When fixing the concentration values at the system boundary, a hierarchy of chemical potentials is imposed, which dictates the direction of the chemical reactions in a phase far away from the system boundaries. In FIG. 3.9, we sketch such a system. The chemical reaction will locally deplete component B inside the droplet, thus lowering the chemical potential of B , which causes a diffusive flux from the reservoirs towards the droplet. Vice versa, component A gets enriched inside the droplet and diffuses outwards.

3.4.1 Droplets in open systems

As already mentioned, in open systems, thus systems that can exchange particles with their surrounding, droplets can not be stationary in the absence of chemical reactions. Instead, droplets either shrink or grow. This is because the volume fraction values at the system boundaries set specific chemical potentials. Particle fluxes occur whenever chemical potentials are locally lower than these values at the system boundary. These particle fluxes flatten concentration gradients in non-interacting mixtures with free diffusion until the chemical potentials are equilibrated. However, these particle fluxes do not smoothen gradients in phase-separated systems but grow phases. This is possible whenever the boundary values lie within the binodal area. Then, a set of identical chemical potentials with lower values than those defined by the reservoirs can be found. The particle flux towards the area of lower chemical potentials now just shifts the phase boundaries.

In FIG. 3.10, we illustrate this in a ternary mixture, where the component B phase separates from the solvent. The domains of growth and shrinkage as a function of the reservoir volume fraction values called ϕ_i^∞ in the following, are shown in FIG. 3.10(a). Droplets shrink in the white domain and grow in the green. The boundary of these domains is given by the binodal line of a closed system. We restrict ourselves to reservoir values outside of the spinodal area, where further droplets would be nucleated. Examples of volume fractions fields of components A (blue) and B (green) in one-dimensional system are shown in FIG. 3.10(b-c). The reservoir values in FIG. 3.10(b) are in the white area. Thus, an initialized droplet shrinks until it dissolves. The stationary state is given by homogeneous solutions of the corresponding boundary values. In FIG. 3.10(c), we carefully selected reservoir values lying on the binodal line. Thus, any droplet, independent of its size, is stable in a 1D system where no Laplace pressure exists. If the reservoir values lie within the green area, droplets grow until they fill the system, see FIG. 3.10(d).

3.4.2 Non-equilibrium steady droplets and shape instabilities

When chemical reactions occur inside droplets, these droplets can be stabilized in open systems. Instead of constantly growing or shrinking, a specific droplet size, dependent on the driving strength and kinetic coefficients, can exist at which the droplet gets stationary. Diffusive processes transport chemical reactants towards the

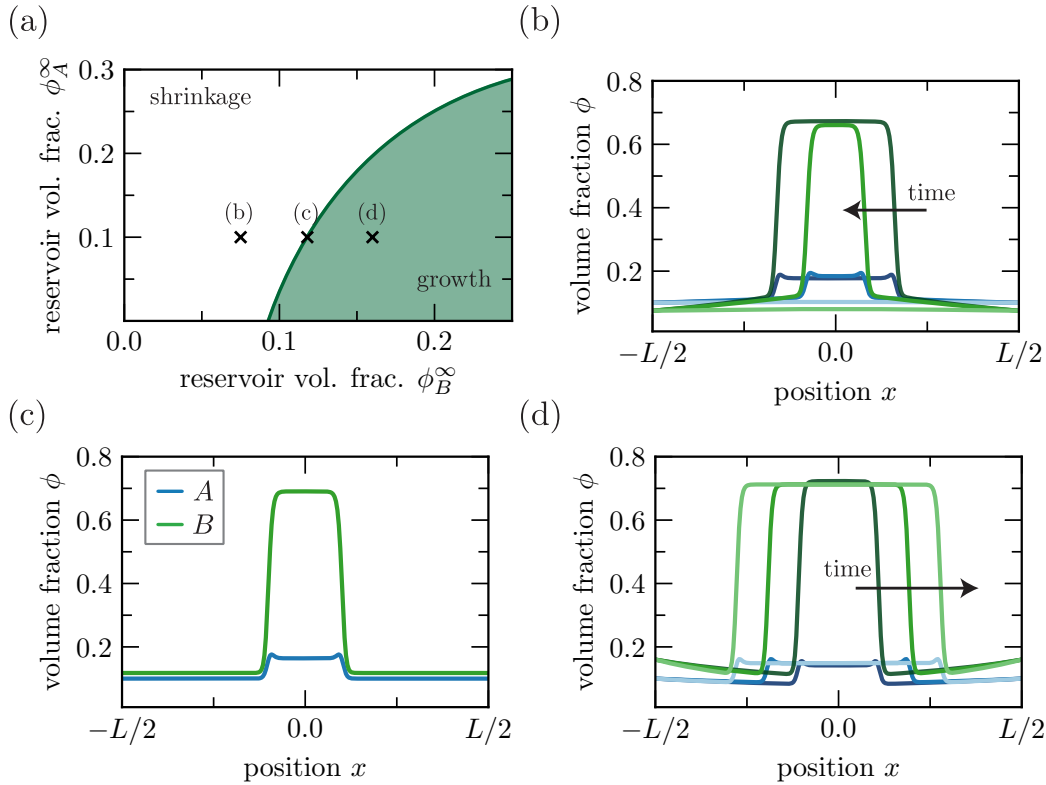


FIGURE 3.10: **Droplet growth and shrinkage in open systems without reactions:** (a): Areas of growth (green) and shrinkage (white) of droplets in open systems as a function of the reservoir values at the system boundaries. (b-d): Exemplary volume fraction profiles of components A (blue) and B (green). Black \times 's in (a) indicate the boundary conditions. Dark colors correspond to earlier time points. For the parameters and details, see App. C.

droplet, where these become products that diffuse outwards towards the reservoirs. The total amount of products that decay at every time point scales with the droplet size, while the total amount of products that enter the droplet scale size of the interface. Small droplets grow, and large droplets shrink until these two processes balance.

We use the same ternary system as in the previous discussion about the droplet in open systems and allow the chemical transition from $A \rightleftharpoons B$ inside the B -rich phase. Again, this is achieved by making the kinetic coefficient k_α composition dependent. In FIG. 3.11(b), we show profiles of the volume fractions ϕ_A and ϕ_B of a one-dimensional system in space. They were obtained by solving Eq. 3.2 numerically until a steady state was reached. The black \times indicates the reservoir values in the composition space, shown in FIG. 3.11(a). They lie within the binodal area (green domain in FIG. 3.11(a)) but below the chemical equilibrium line (purple). Thus, the system can phase separate, and the chemical potential of B is larger than that of component A . At the interface of the droplet, local phase equilibrium is established. This can be seen when plotting the interface values from the local profile in the composition space - indicated by the yellow symbols in FIG. 3.11. Both lie on the binodal line and are connected by a tie line. However, both pairs of volume fractions still

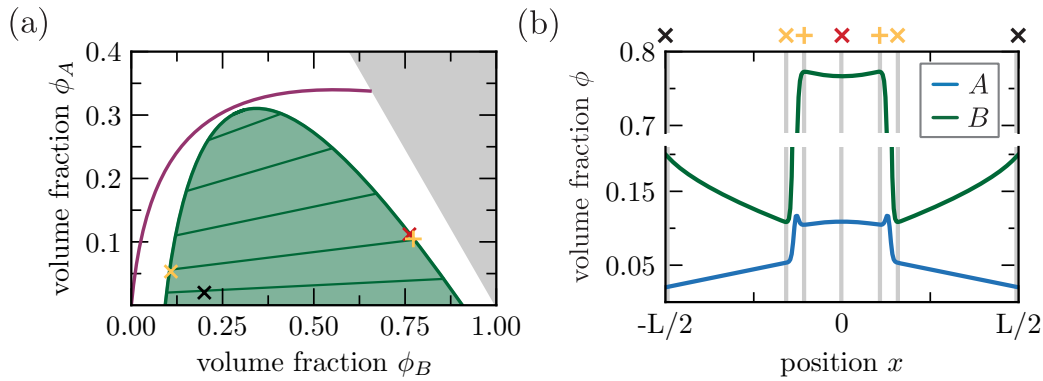


FIGURE 3.11: **Stationary chemically boundary driven droplet in 1D:** (a): The chemical equilibrium line (purple), the binodal line (thick green), and tie lines (thin green) of a closed system are shown in the composition space. Furthermore, we highlight the boundary values (black), the values at the interface (yellow), and the value at the center of a stationary droplet (red), shown in (b). (b): Volume fraction profiles in a 1D system are shown of a stationary chemically active droplet. The symbols on top of the grey lines correspond to the symbols in (a). For parameter choices and details, see App. C.

lie below the chemical equilibrium line. Thus, the chemical reaction runs predominantly from B to A inside the droplet. This causes a decreasing profile of B and an increasing profile of A towards the droplet center. The volume fraction values here are closer to the local chemical equilibrium, indicated by the equilibrium line in FIG. 3.11(a).

However, the size of these droplets can be controlled by the reservoir values. This, we show in FIG. 3.12. Here, we solve Eq. 3.2 in a two-dimensional system⁵ for five different reservoir values, again indicated by the black x 's in the composition space shown in FIG. 3.12(a) and numerated with I-V. All of them lie within the binodal area. However, for low values of ϕ_B^∞ , e.g. by setting I, no stationary droplet can exist, see FIG. 3.12(b). For higher reservoir values of B , stationary chemically active droplets exist, with larger sizes for higher values of ϕ_B^∞ , see II-IV. Furthermore, chemically active droplets driven over the system boundaries also can undergo shape instabilities and elongate, similar to the droplets in systems with driven chemical reactions discussed in the previous section. In FIG. 3.12(c), we show the volume fraction fields for different time points for even higher values of ϕ_B^∞ . After initializing a slightly elongated droplet, the droplet elongates and divides. Both daughter droplets grow in size and move towards the system boundaries. When reaching them, they form a wetting layer, and a stationary state is reached. We study this shape instability further in the following chapter.

⁵This system is similar to the previous system. However, we changed the parameters slightly such that A is enriched in the B -poor phase for illustrative purposes in FIG. 3.12(c).

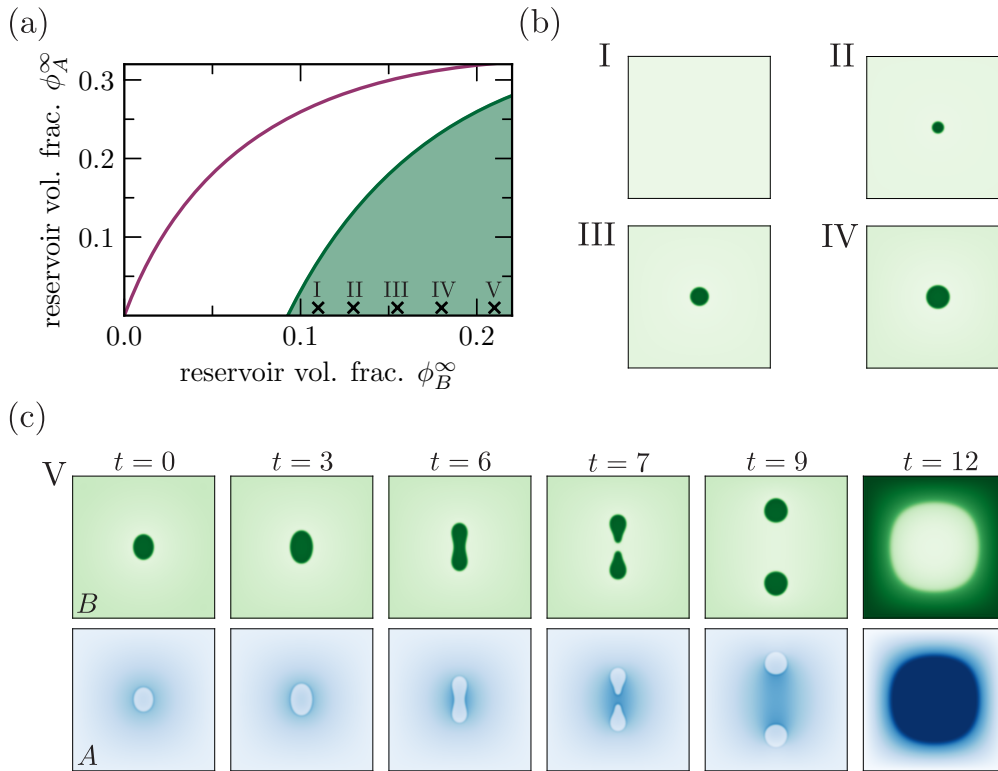


FIGURE 3.12: **Stationary chemically active droplets and shape instabilities in 2D:** (a): The chemical equilibrium line (purple) and the binodal line (green) of a closed system in the volume fraction space of the reservoir values. We indicate reservoir values of the systems shown in (b-c) with black x's. (b): Spatial density plots of the volume fraction ϕ_B are shown of stationary chemically active droplets in 2D systems with different reservoir values, indicated in (a) with I-IV. (c): Density plots of the volume fraction field ϕ_A (blue) and ϕ_B (green) at different time points for the reservoir values V, when a slightly elongated droplet was initialized. For parameters choices and details, see App. C.

3.5 Discussion

This chapter introduced the governing equations for the dynamics of volume fractions fields in phase-separating systems with chemical reactions. For passive systems, this dynamics relaxes toward the thermodynamical equilibrium described in Section 1.3. The relative magnitude of the kinetic coefficients and the system size govern which equilibrium, either phase or chemical equilibrium, is reached first. We compared the dynamics for chemical reactions at phase equilibrium from Chap. 2 to the spatial dynamics in the limit of fast diffusion. Both agree well, except for the local stability of well-mixed states outside the spinodal and minor differences due to the Laplace pressure.

Furthermore, we studied two different ways of maintaining the system out of equilibrium. First, by driving chemical reactions specific in phases. Second, by coupling the system to reservoirs at its boundaries. In both cases, chemical reactions can reach locally different equilibria than compatible with phase equilibrium. In spatial systems with sufficiently fast reactions, spatial gradients occur, causing spatial fluxes

that are balanced by fluxes of chemical reactions. However, due to molecular interactions, these spatial gradients also affect the conserved quantities. The latter causes a different droplet dynamics in active systems. While in equilibrium systems, droplets continuously grow or ripen until the equilibrium is reached, droplets deform, divide or show reversed ripening in active systems.

Chapter 4

Chemically active droplets in the sharp interface limit

The last chapter showed that in systems with chemical reactions organized by phase separation, out-of-equilibrium situations can emerge where phase equilibrium and chemical equilibrium cannot be satisfied simultaneously. Here, the dynamics of droplets can differ from passive systems. In the latter, droplets in the nucleation-and-growth regime grow spherical until they have reached the maximal size compatible with the conservation laws in the system. In active systems, these droplets can undergo shape instabilities, leading to elongated droplets or droplet division. This chapter introduces an effective description of chemically active droplets inside that nucleation-and-growth regime. Thus, the dynamics of single droplets in out-of-equilibrium situations.

Instead of solving the dynamical equations in spatially continuous systems, we reduce the system to two reaction-diffusion equations coupled via a moving interface¹. Therefore, we assume an infinitely sharp interface, only taken into account by its corresponding surface tension. This limit is valid for large enough droplets and reaction-diffusion length scales larger than the interface width. Inside the phases, we linearize the dynamics. Thus, all the non-linearities of the problem get reduced to boundary conditions at the interface. With this, we can quantitatively study the stationary size of spherical chemically active droplets and their shape instability under these simplified dynamics.

4.1 Droplet dynamics via reaction-diffusion equations coupled by a moving interface

When phase separation occurs, the volume fraction values at the interface jump, while the chemical potentials are continuous in space. In the following, we will call these volume fraction values at the interface $\Phi^{I/II}$. Assuming we know these values, we can linearize Eq. 3.1 around the corresponding values in each phase and make the limit $\kappa_i \rightarrow 0$, such that the interface width goes to zero. The exact values of

¹These moving boundary problems are also called Stefan problem [60].

these interface volume fractions are then determined at the end in a self-consistent manner. With the linearization, we obtain

$$\partial_t \phi_i = \sum_{j=1}^M \left[D_{ij}^{I/\Pi} \nabla^2 \phi_j + k_{ij}^{I/\Pi} (\phi_j - \Phi_j^{I/\Pi}) \right] + c_i^{I/\Pi}, \quad (4.1)$$

where $D_{ij}^{I/\Pi} = D_{ij}(\Phi^{I/\Pi})$ are the diffusion coefficients introduced in Eq. 1.11. The reaction coefficients k_{ij} are obtained from the reaction fluxes r_i , given in Eq. 1.39, by

$$k_{ij}^{I/\Pi} = \frac{\partial r_i(\Phi_i^{I/\Pi})}{\partial \phi_j} \quad (4.2)$$

and constant source terms are

$$c_i = r_i(\Phi_i^{I/\Pi}) \quad . \quad (4.3)$$

The latter source terms result from the fact that volume fraction values at the interface are no stationary states of the chemical reactions in general.

Furthermore, we can also express the fluxes of volume fraction

$$j_i^{I/\Pi}(x) = - \sum_{k=1}^M D_{ik} \nabla \phi_k \quad , \quad (4.4)$$

as functions of the volume fractions at the interface $\Phi_i^{I/\Pi}$.

These linear equations can be solved. Thus, the volume fraction profiles and their fluxes can be found analytically, given an interface position R and the values $\Phi_i^{I/\Pi}$ on both sides of the interface. However, these interface volume fractions are not free. Locally, the chemical potentials and the osmotic pressure must be balanced, leading to values of $\Phi_i^{I/\Pi}$ that obey a local phase equilibrium. Nevertheless, the constraint of phase equilibrium only determines these values fully in a binary mixture. Already in a ternary mixture, all volume fraction values along the binodal² line (manifold) obey these conditions. The values at phase equilibrium in passive systems are only defined by the additional global conservation laws of $\bar{\phi}_i$, see Eq. 1.6. Therefore, additional conservation laws are needed to determine the interface values self-consistently. We will discuss these interface conditions in the next section.

4.2 Stationary interface positions in spherical symmetry

The additional conservation laws differ between open and closed systems. Closed systems have to obey global conservation laws, which are absent in open systems, where material can be exchanged with the surrounding. In this work, we restrict ourselves to quasi-stationary dynamics of the interface. Thus, the volume fraction profiles are considered to be at steady state, while the interface can slowly relax

²Strictly, the binodal does not take the shift stemming from the Laplace pressure into account, which has to be considered.

towards its stationary state. However, the global conservation laws prohibit this limit. Assuming that the volume fraction profiles are at steady state immediately leads to a non-moving interface. Therefore, we solve in closed systems directly for the stationary interface position, while in open systems, a quasi-stationary relaxation kinetics towards this position can be considered. In general, also the dynamical problem of Eq. 4.1 can be solved analytically. This would also allow us to investigate the relaxation kinetics in closed systems. However, due to the non-linear interface conditions, this approach is challenging.

4.2.1 Interface conditions in closed systems

In closed systems with non-flux boundary conditions at the system boundaries, and at steady state of the volume fraction profiles, there can not be fluxes of conserved quantities. Therefore, no conserved material is transported, and the interface position has to be at a steady state when the values of conserved densities differ between the phases. Nevertheless, the conserved quantities can still have gradients because of the coupling of the fluxes to the non-conserved reaction extents. As mentioned above, in a closed system, we solve for the volume fraction values $\Phi^{I/II}$ and the stationary interface position R . Thus, in total $2M + 1$ unknowns have to be determined by conditions at the interface. These constraints read

$$\begin{aligned}
&\bullet \text{ chem. pot. balance between phases: } \bar{\mu}_i^I = \bar{\mu}_i^{II}, & M \\
&\bullet \text{ pressure condition: } f^I - f^{II} = \sum_{i=1}^M \frac{\bar{\mu}_i^{I/II}}{\nu_i} (\phi_i^I - \phi_i^{II}) - \frac{2\gamma}{R}, & 1 \\
&\bullet \text{ local conservation laws: } \mathbf{j}_j^{\xi,I}(R) = \mathbf{j}_j^{\xi,II}(R), & L \\
&\bullet \text{ global conser. laws: } \int_0^R dr r^2 \psi_i^I(r) + \int_R^{R^{\text{sys}}} dr r^2 \psi_i^{II}(r) = (R^{\text{sys}})^3 \bar{\psi}_i, & M - L \\
& & \frac{2M + 1}{(4.5)}
\end{aligned}$$

Here, we assumed a spherical droplet of phase I in a closed spherical system with size R^{sys} in 3D. For 2D systems, the additional Laplace-pressure term $-2\gamma/R$ in the pressure condition gets reduced to $-\gamma/R$, while in 1D systems, it vanishes completely. Furthermore, the surface tension itself is a function of the interface volume fractions. We determine it by the method explained in App. B. Locally at the interface, we assume an equilibrium of phase separation, local conservation laws of the reaction extents, and global conservation laws of the conserved quantities in the system. This determines all volume fractions $\Phi_i^{I/II}$ and the stationary interface position. We illustrate this method for the same system as we used in Section 3.3.2. There, we introduced a one-dimensional closed system maintained away from equilibrium by phase-specific driving of a chemical reaction between two components in a ternary mixture. The volume fraction profiles of non-equilibrium steady states are shown in FIG. 3.4(b). Here, we compare these profiles obtained by solving the continuous

partial differential equations with the resulting profiles using the method introduced above. We linearize the dynamical equations and find the set of equations

$$\begin{aligned}\partial_t \phi_A^{I/II} &= D_{AA}^{I/II} \nabla^2 \phi_A^{I/II} + D_{AB}^{I/II} \nabla^2 \phi_B^{I/II} + k_{AA}^{I/II} (\phi_A^{I/II} - \Phi_A^{I/II}) + k_{AB}^{I/II} (\phi_B^{I/II} - \Phi_B^{I/II}) + c_A^{I/II}, \\ \partial_t \phi_B^{I/II} &= D_{BA}^{I/II} \nabla^2 \phi_A^{I/II} + D_{BB}^{I/II} \nabla^2 \phi_B^{I/II} + k_{BA}^{I/II} (\phi_A^{I/II} - \Phi_A^{I/II}) + k_{BB}^{I/II} (\phi_B^{I/II} - \Phi_B^{I/II}) + c_B^{I/II},\end{aligned}\quad (4.6)$$

in the corresponding phases I (*B*-rich) and II (*B*-poor), with $k_{BA}^{I/II} = -k_{AA}^{I/II}$, $k_{BB}^{I/II} = -k_{AB}^{I/II}$ and $c_B^{I/II} = -c_A^{I/II}$. Due to the initialization in Section 3.3.2, we assume that phase II is to the left of phase I. The stationary solutions of Eq. 4.6 in phase II can be written as

$$\begin{aligned}\phi_A^{II}(x) &= \frac{c_A^{II}}{k_{AA}^{II} + k_{AB}^{II} \rho^{II}} \left(\frac{\cosh(x/\lambda^{II})}{\cosh(R/\lambda^{II})} - 1 \right) + \Phi_A^{II}, \\ \phi_B^{II}(x) &= \frac{c_A^{II} \rho^{II}}{k_{AA}^{II} + k_{AB}^{II} \rho^{II}} \left(\frac{\cosh(x/\lambda^{II})}{\cosh(R/\lambda^{II})} - 1 \right) + \Phi_B^{II},\end{aligned}\quad (4.7)$$

for $0 < x < R$, where R is the position of the interface. These solutions fulfil the boundary conditions $j_i^{II}(0) = 0$ and $\phi_i^{II}(R) = \Phi_i^{II}$. Similarly, the stationary solutions in phase I read

$$\begin{aligned}\phi_A^I(x) &= \frac{c_A^I}{k_{AA}^I + k_{AB}^I \rho^I} \left(\frac{\cosh((x-L)/\lambda^I)}{\cosh((R-L)/\lambda^I)} - 1 \right) + \Phi_A^I, \\ \phi_B^I(x) &= \frac{c_A^I \rho^I}{k_{AA}^I + k_{AB}^I \rho^I} \left(\frac{\cosh((x-L)/\lambda^I)}{\cosh((R-L)/\lambda^I)} - 1 \right) + \Phi_B^I,\end{aligned}\quad (4.8)$$

for $R < x < L$. Here, the boundary conditions are stated by $j_i^I(L) = 0$ and $\phi_i^I(R) = \Phi_i^I$. The factor $\rho^{I/II}$ and the length-scales $\lambda^{I/II}$ are connected to the diffusion coefficients D_{ij} and reaction rates k_{ij} via

$$\begin{aligned}\rho^{I/II} &= -\frac{D_{AA}^{I/II} + D_{BA}^{I/II}}{D_{AB}^{I/II} + D_{BB}^{I/II}}, \\ \lambda^{I/II} &= \sqrt{\frac{D_{AB}^{I/II} D_{BA}^{I/II} - D_{AA}^{I/II} D_{BB}^{I/II}}{(D_{AB}^{I/II} + D_{BB}^{I/II}) k_{AA}^{I/II} - (D_{AA}^{I/II} + D_{BA}^{I/II}) k_{AB}^{I/II}}}.\end{aligned}\quad (4.9)$$

The latter are the reaction-diffusion length scales, now expanded around phase equilibrium as opposed to Eq. 3.3, where we expanded around the stationary state of chemical reactions. With this, Eq. 4.7 and Eq. 4.8 are the general solutions for the linearized dynamics around arbitrary interface values $\Phi_i^{I/II}$. Furthermore, we can compute the resulting fluxes $j_i^{I/II}(\Phi_i^{I/II})$ at the interface for those volume fraction values. Being able to express the fluxes as functions of $\Phi_i^{I/II}$ enables us finally to solve for the boundary conditions at the interface and the interface position. As

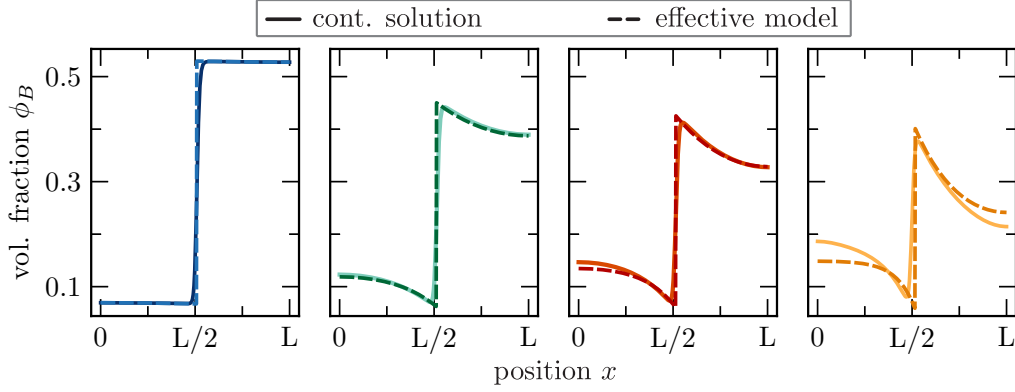


FIGURE 4.1: **Comparison of continuous profiles and the effective description for different kinetic coefficients:** The continuous profiles (solid lines) are identical to the curves shown in FIG. 3.4(b) with the same color. The reaction-diffusion length scale decreases from left to right. Furthermore, we plot the corresponding solution of the effective model on top of these profiles (dashed lines). For the specific parameters, see App. C.

stated in Eq. 4.5, from the assumption of phase equilibrium at the interface, we obtain $\bar{\mu}_A^I = \bar{\mu}_A^{\text{II}}, \bar{\mu}_B^I = \bar{\mu}_B^{\text{II}}$ and $f^I - f^{\text{II}} = \bar{\mu}_A^{I/\text{II}}(\phi_A^I - \phi_A^{\text{II}}) + \bar{\mu}_B^{I/\text{II}}(\phi_B^I - \phi_B^{\text{II}})$. In the latter condition, no additional term from the surface tension appears due to the Laplace pressure's absence in $1D$. Furthermore, the local conservation of component A at an infinitely small interface region requires $j_A^I(R) = j_A^{\text{II}}(R)$. Due to the symmetry $j_A^{I/\text{II}}(x) = -j_B^{I/\text{II}}(x)$ for all x , this automatically fulfills the conservation law of component B . Thus, we obtain four conditions for the four interface values. However, the position of the interface R is determined by the amount of conserved material $\bar{\psi}$ in the system. We find³ $R/L = (\bar{\psi} - \Phi_A^I - \Phi_B^I) / (\Phi_A^{\text{II}} + \Phi_B^{\text{II}} - \Phi_A^I - \Phi_B^I)$.

In FIG. 4.1, we show the solutions for four different values of the kinetic coefficients Γ/k . This ratio decreases from the left plot to the right. The reaction-diffusion length scale is directly proportional to $\sqrt{\Gamma/k}$. Thus, the larger this ratio becomes, the weaker the spatial gradient. For the first plot (blue color scheme), we choose $\Gamma/k = 10^{-6}$. This choice leads to $\lambda^I/L = 4.6$ and $\lambda^{\text{II}}/L = 1.6$ (their value differ slightly from the reaction-diffusion length scales when expanded around the effective chemical equilibrium, e. g. $\lambda_{\text{RD}}^I/L = 4.7$). Therefore, the profiles get almost constants in the corresponding phases. To show the equivalency to the non-equilibrium steady state for homogeneous phases, as introduced in Section 3.1, we note that

$$\begin{aligned} j_i^{\text{II}}(x) &= r_i^{\text{II}} \lambda^{\text{II}} \tanh\left(R/\lambda^{\text{II}}\right) + \mathcal{O}(x - R) \quad , \\ j_i^I(x) &= r_i^I \lambda^I \tanh\left((R - L)/\lambda^I\right) + \mathcal{O}(x - R) \quad , \end{aligned} \quad (4.10)$$

in general. When $R < \lambda^{\text{II}}$ and $L - R < \lambda^I$, we can use $\tanh(x) \approx x$ and obtain from the condition $j_i^I = j_i^{\text{II}}$ again the stationarity condition from Eq. 2.10 in the form of $r_i^{\text{II}} R = -r_i^I (L - R)$ for a one-dimensional system. For the second and third plots

³Here, we assume that the conserved quantity stays constant in space. This is not true in general, but given the mobility coefficients stated in Eq. 1.10 and the molecular interactions chosen in this example, the gradients of the conserved quantities are weak.

(green and red color schemes), $\Gamma/k = 5 \cdot 10^{-5}$ and $\Gamma/k = 10^{-4}$. These choices lead to $\lambda^I/L = 0.65$ and $\lambda^{II}/L = 0.23$ for the second plot and $\lambda^I/L = 0.46$ and $\lambda^{II}/L = 0.17$ for the third plot. Spatial gradients become visible. However, the effective description matches the continuous solutions to a reasonable degree. The two profiles must differ directly at the interface because the effective description assumes an infinitely sharp interface. Furthermore, the profiles can deviate from each other far away from the interface because we linearize the reaction fluxes around the interface values. This effect can be seen already in phase II in the third plot, but it becomes more dominant in the fourth plot. Here, we choose $\Gamma/k = 3 \cdot 10^{-4}$ which leads to $\lambda^I/L = 0.26$ and $\lambda^{II}/L = 0.10$. The spatial gradients become strong enough to show large deviations between the two profiles, resulting from the non-linear nature of the reaction fluxes and diffusive fluxes in phase-separating systems.

In general, the method introduced above allows to self-consistently solve for non-equilibrium steady states in the presence of spatial gradients. It captures the continuous solutions well when the interface length scale is small and the spatial gradients are weak. Under these circumstances, the assumption of an infinitely sharp interface becomes valid, and the linear order of the dynamics is sufficient to describe the spatial gradients. However, it does not take spinodal instabilities into account.

4.2.2 Interface conditions in open systems

In open systems, like the case with boundary driven chemically active droplets, components can be exchanged with the surrounding. Therefore, the under chemical reactions conserved quantities can change in the system over time. Thus, divergence-free fluxes of the conserved quantities can exist and droplets can grow or shrink in the quasi-stationary limit. Instead of solving for the stationary radius directly, we can assume any droplet radius R . The boundary conditions at the interface read

- chem. pot. balance between phases: $\bar{\mu}_i^I = \bar{\mu}_i^{II}$, M
- pressure condition: $f^I - f^{II} = \sum_{i=1}^M \frac{\bar{\mu}_i^{I/II}}{\nu_i} (\phi_i^I - \phi_i^{II}) - \frac{2\gamma}{R}$, 1
- local conservation laws: $\frac{\mathbf{j}_i^I - \mathbf{j}_i^{II}}{\phi_i^I - \phi_i^{II}} = \frac{\mathbf{j}_k^I - \mathbf{j}_k^{II}}{\phi_k^I - \phi_k^{II}}$, $M - 1$

(4.11)

The local conservation laws result from the continuity equation in the comoving frame of reference and the fact that the normal velocity

$$v = \frac{\mathbf{j}_i^I - \mathbf{j}_i^{II}}{\phi_i^I - \phi_i^{II}} \mathbf{n} \quad , \quad (4.12)$$

where \mathbf{n} is the normal vector of the interface, is identical for every component. Thus, by assuming a droplet radius R and Eq. 4.11, we obtain the temporal dynamics of

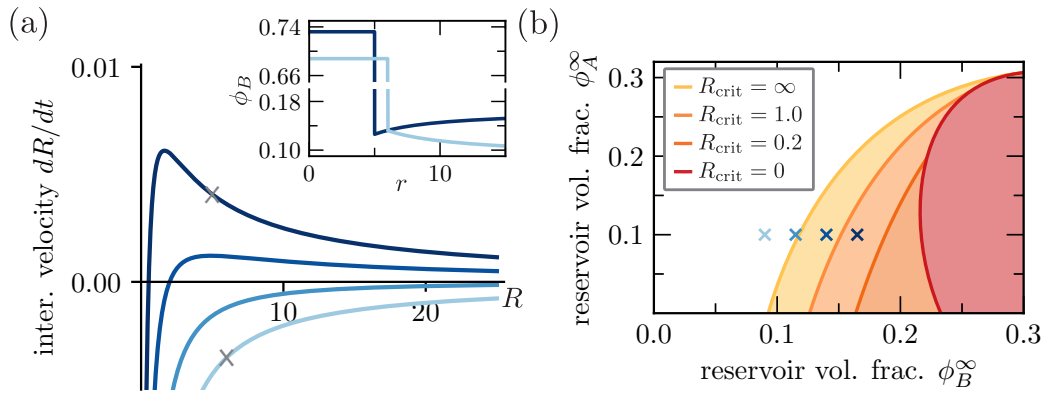


FIGURE 4.2: **Growth and shrinkage of a droplet in an open system without chemical reactions:** (a): Interface velocities as a function of droplet size in open systems are shown. The x's of the same color denote the reservoir values of these curves in composition space in (b). In the inset of (a), we show the volume fraction profiles for the two droplets denoted by the grey x's in (a). (b): Domains with continuously growing droplets, when initialized above the critical radius denoted in the corresponding color, are shown. The yellow line corresponds to the binodal line, and the red line to the spinodal of a closed system. Droplets always dissolve in the white domain. For the parameters, see App. C.

the interface. It follows

$$\frac{dR}{dt} = v \quad , \quad (4.13)$$

leading to growth or shrinkage of a droplet.

Identical to the last chapter, we use this method to show the growth and shrinkage dynamics of droplets in open systems without chemical reactions. Therefore, we study the same system of a ternary mixture studied in Sec. 3.4.1. We control the volume fraction values of reservoirs ϕ_A^∞ and ϕ_B^∞ far away from the droplet. The stationary solutions of Eq. 4.1 are solutions of the spherical Laplace equation. For a B -rich droplet with radius R , we find

$$\begin{aligned} \phi_i^I(r) &= \Phi_i^I \quad , \\ \phi_i^{\text{II}}(r) &= \frac{(\Phi_i^{\text{II}} - \phi_i^\infty)R}{r} + \phi_i^\infty \quad . \end{aligned} \quad (4.14)$$

Inside the droplet, no diffusive fluxes occur, while in the outside area, divergence-free fluxes transport molecules either towards or away from the droplet. Using Eq. 4.14, we can express these fluxes at the interface $j_i^{\text{II}}(R)$ as functions of Φ_i^{II} . Finally, Eq. 4.11 can be used to determine the values $\Phi_i^{\text{I/II}}$. Note that the surface tension itself is also a function of $\Phi_i^{\text{I/II}}$, see App. B.

Instead of the average composition, FIG. 4.2(b) shows a stability diagram in terms of the composition of the reservoirs. The yellow line is the binodal line. When the reservoirs have values lying on this line, no finite droplet can exist due to the surface tension. The red line is the spinodal line. For reservoir values inside the spinodal area (red), droplets would be spontaneously built in the system, thus violating our assumption of a single droplet. In between, a critical radius $R > R_{\text{crit}}$ exists, as defined in Eq. 1.15. Droplets of larger sizes, thus $R > R_{\text{crit}}$, always grow while

smaller droplets shrink. We show lines of two different critical radii (light orange and orange). These lines define areas in the phase diagram. For example, inside the light orange area, all droplets smaller than $R = 1$ shrink, while droplets larger than this radius will grow. In FIG. 4.2(a), we show the interface velocity as a function of droplet size for four different reservoir values (depicted by x in the corresponding color in FIG. 4.2(b)). The two examples with reservoir values within the binodal area but outside the spinodal area always have a positive interface velocity beyond the critical radius. The interface velocity is always negative for reservoir values outside the binodal area. Therefore, in the absence of chemical reactions, no stationary state can occur, and one phase will always grow at the expense of the other. Furthermore, we show two profiles of volume fraction in the inset of FIG. 4.2(a). The reservoir values are depicted by the color of the lines, matching the corresponding velocity curves, and the droplet sizes by grey x 's in FIG. 4.2(a).

For chemically active droplets driven over the system's boundary, we now allow chemical reactions inside the droplet, as introduced in Sec. 3.4. Here, we study the dynamics of these droplets in ternary mixtures quantitatively, first, in systems with the same interaction parameters as studied previously in the absence of chemical reactions for two systems with different reference chemical potentials ω_i , leading to two different chemical equilibrium lines. Second, for a system where both components, A and B , can phase separate from the solvent solely.

In all cases, the chemical reactions inside the droplet lead to gradients in the volume fraction profiles, even at the stationary state. These stationary volume fraction profiles of Eq. 4.1 for a single spherical symmetric droplet of radius R are given by

$$\begin{aligned}\phi_A^I(x) &= \frac{c_A^I}{k_{AA}^I + k_{AB}^I \rho^I} \left(\frac{\sinh(r/\lambda^I)}{\sinh(R/\lambda^I)} \frac{R}{r} - 1 \right) + \Phi_A^I, \\ \phi_B^I(x) &= \frac{c_A^I \rho^I}{k_{AA}^I + k_{AB}^I \rho^I} \left(\frac{\sinh(r/\lambda^I)}{\sinh(R/\lambda^I)} \frac{R}{r} - 1 \right) + \Phi_B^I,\end{aligned}\quad (4.15)$$

where λ^I and ρ^I are given in Eq. 4.9. In the outside phase, no reaction occurs. The stationary solutions of Eq. 4.1 are identical to the solutions of $\phi_i^{\text{II}}(r)$ given in Eq. 4.14. Finally, we can use Eq. 4.11 for finding the values $\Phi_i^{\text{I/II}}$ at the interface.

In FIG. 4.3(a), we show exemplary solutions of the the volume fraction profiles stated in Eq. 4.15 and Eq. 4.14. Here, we have chosen $\phi_B^\infty = 0.17$ and $\phi_A^\infty = 0.05$. For these values, $\bar{\mu}_B^\infty$ is larger than $\bar{\mu}_A^\infty$, leading to a predominant degradation of B within the droplet. With this degradation, also the chemical potential of B gets reduced inside the droplet, leading to a diffusive flux j_B from the reservoir to the droplet. Vice versa, A material gets produced within the droplet and carried away by diffusive fluxes j_A to the reservoir. Thus, the chemical reaction can never equilibrate. However, for the shown case of a droplet with size $R = 15$, B material gain via j_B is smaller than the loss of A via j_A . A droplet of this size therefore shrinks. Thus the interface velocity dR/dt is negative as displayed in FIG. 4.3(b) (denoted by grey x), where we show the interface velocity dR/dt as a function of droplet size. For the chosen examples, $\phi_A^\infty = 0.05$ and we vary ϕ_B^∞ . For the cases of $\phi_B^\infty = 0.08$ and

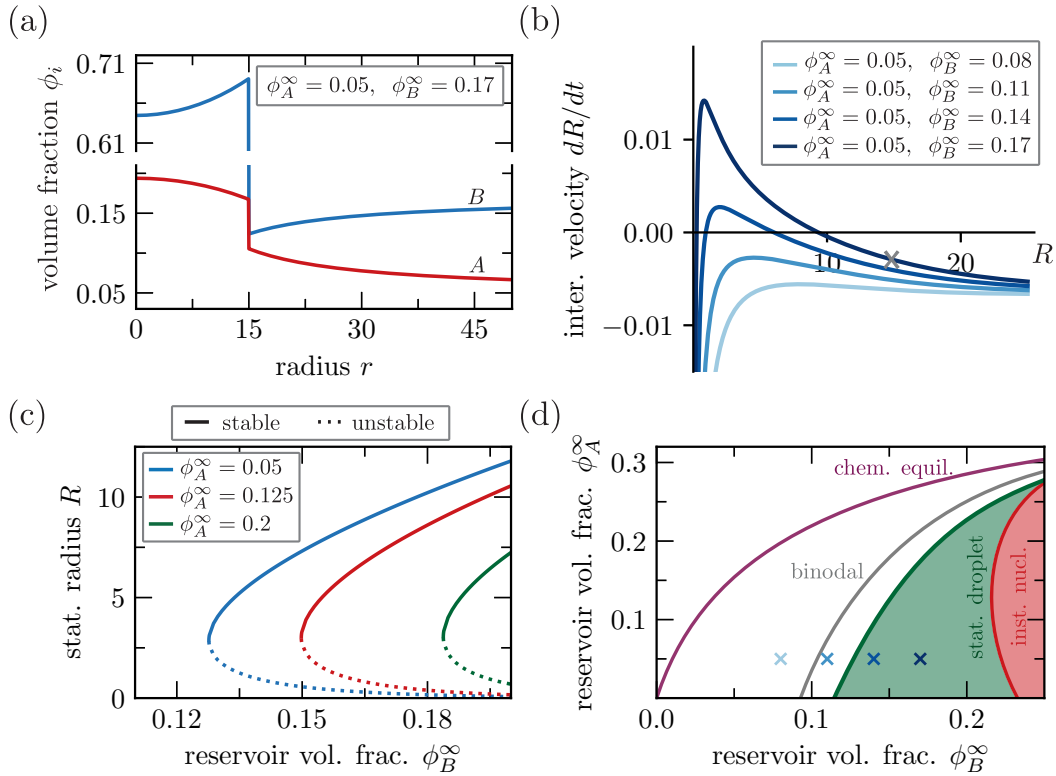


FIGURE 4.3: **Stationary chemically active droplets in a boundary driven system:** (a): Radial profiles of a chemically active droplet are shown. Its interface velocity is denoted by the grey x in (b). (b): Interface velocities as a function of droplet size R are shown for reservoir volume fractions settings, indicated by the x's with the same color in (d). (c): The roots of the dR/dt -functions in (b) denote the stationary droplet radii. The larger radii are stable (solid), while the smaller radii are unstable (dotted). (d): The line of chemical equilibrium in the reservoir (purple) and the binodal of a closed system without chemical reactions (grey) are shown. In the green domain, chemically active droplets with stationary radius exist, while in the red domain, the homogeneous compositions in the reservoirs are locally unstable. No stationary chemically active droplets can exist in the white domain. For further details and parameters, see App. C.

$\phi_B^\infty = 0.11$, droplets of all sizes will shrink. However, for the cases $\phi_B^\infty = 0.14$ and $\phi_B^\infty = 0.17$, we find regions of positive interface velocities. The roots of this function dR/dt denote stationary droplet radii. While the left one is unstable, and thus the critical radius of nucleation, similar to the case without chemical reactions, the right one is stable. It depicts the stationary radius of a spherical chemically active droplet. These two stationary radii are shown as functions of ϕ_B^∞ for three different values of ϕ_A^∞ in FIG. 4.3(c). Identical to the numerical studies in 2D of a similar system, see FIG. 3.12, the stationary radii grow for larger values of ϕ_B^∞ . We show the stability diagram in terms of the reservoir volume fractions ϕ_i^∞ in FIG. 4.3(d). Here, the purple line denotes the chemical equilibrium line, where $\bar{\mu}_A^\infty = \bar{\mu}_B^\infty$. Below this line $\bar{\mu}_B^\infty > \bar{\mu}_A^\infty$, and vice versa above. The grey line is the binodal line of a closed system without chemical reactions. Different from the system without chemical reactions, even when the reservoir values ϕ_i^∞ lie within the binodal area, some chemically active droplets do not grow. This is because the nucleation radius set by the surface

tension is larger than the length scales set by the chemical reactions. Only at the green line does the function dR/dt intersect the x -axis, leading to spherical droplets of fixed size in the green area. The red line is the spinodal line. The reservoir values in the red area would lead to an instant decomposition of the system, thus violating our assumption of a single spherical droplet. The blue x 's denote the examples shown in FIG. 4.3(b), matching the curves of identical color.

Here, we have chosen parameters such that $\bar{\mu}_B^\infty > \bar{\mu}_A^\infty$ within the binodal area. Thus the chemical equilibrium line does not intersect the binodal line. However, changing the reference chemical potentials ω_i , as introduced in Eq. 1.2, the binodal and spinodal lines stay constant, but the chemical equilibrium line gets shifted. In FIG. 4.4(a), we show the stability diagram for a system with identical interactions but other reference chemical potentials, such that the chemical equilibrium line intersects the binodal line. Under these circumstances, also the line for stationary droplets (green) can intersect the chemical equilibrium line. Our analysis shows that independent of ϕ_B^∞ , chemically active droplets driven by reservoirs with a ϕ_A^∞ values above the value of this intersection point (yellow area) do not have a stationary stable radius and continuously grow, even for reservoir values outside of the binodal area. To illustrate that, we show the interface velocity dR/dt as a function of R for the reservoir values denoted by the blue x 's in FIG. 4.4(c). This function for the two dark blue values from the green area has two roots, leading to the critical and stable radii. However, for the other three parameter values (lighter blue), only one root exists and thus only the critical radius. In FIG. 4.4(e), we show these radii as a function of ϕ_B^∞ . For higher ϕ_A^∞ values, the stable critical radii get larger until they diverge at $\phi_A^\infty \approx 0.176$.

Finally, we also discuss a system where both components, A and B , can phase separate from the solvent S . Here, we allow the chemical reaction $A \rightleftharpoons B$ only in the solvent-poor phase. In general, the area of always growing droplets (yellow) increases while the area of stationary droplets (green) gets reduced under these circumstances. In many cases of such interaction parameters, the region of stable droplets disappears completely. When both components can phase separate, the binodal area reaches from the x -axis to the y -axis in the stability diagram. Therefore, the chemical equilibrium line must cross the binodal line. An exemplary phase diagram of such a system is shown in FIG. 4.4(b). In the chosen example, the interaction between B and S is stronger than between A and S . This asymmetry leads to a small area of stationary droplets for low ϕ_A^∞ values. However, when ϕ_B^∞ becomes too large, the stationary radius again vanishes, see FIG. 4.4(d,e).

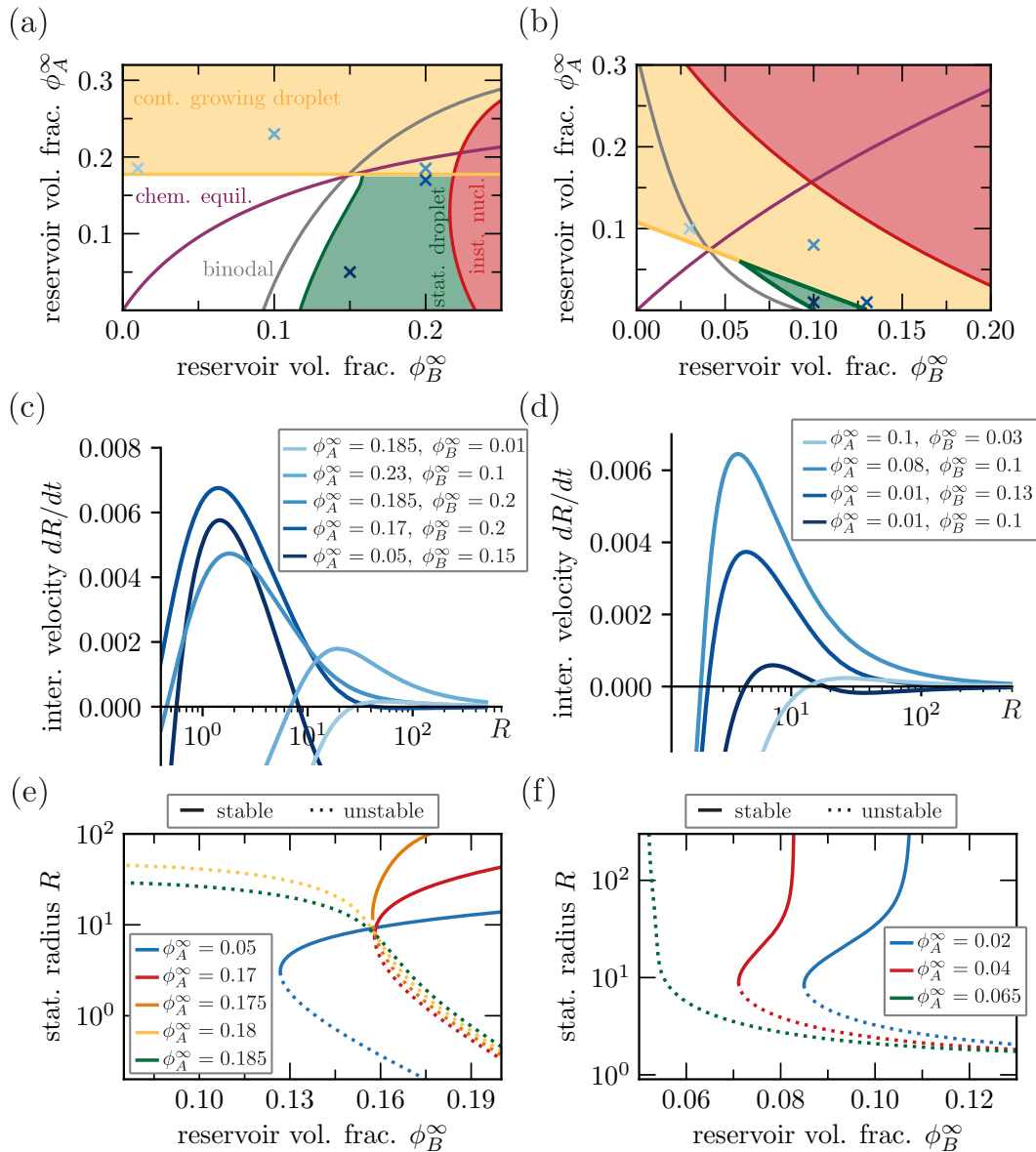


FIGURE 4.4: **Stationary chemically active droplets for different phase diagrams:** (a,b): Stability domains of chemically active droplets for different reservoir values are shown. Areas without (white) and with (green) stable stationary radii are indicated. In the yellow domains, only unstable stationary radii exist. The red area indicates the spinodal regime where many droplets would be instantaneously nucleated. Furthermore, the line of chemical equilibrium in the reservoir (purple) and the binodal of a closed system without chemical reactions (grey) are shown. (c,d): The interface velocities dR/dt as a function of droplet radius R are shown for the parameter settings indicated by the x 's in (a,b) with identical colors. (e,f): Stable (solid) and unstable (dotted) stationary radii as a function of the reservoir value ϕ_B^∞ are shown for different values of ϕ_A^∞ . For the parameters, see App. C.

In general, even when the effective description finds stable spherical droplets, their stability against shape deformation must be considered: First, the values at the droplet center can reach the spinodal area. When this happens, a solvent-rich phase is built, leading to spherical shells, similar to the process described in FIG. 3.4(c). Second, when the droplet is chemically driven, spherical droplets can become unstable and deform, as seen in the previous chapter. We study this shape instability

in the following.

4.3 Shape instabilities of spherical droplets

In out-of-equilibrium situations, droplets can elongate. The spherical symmetric shape becomes unstable, and the droplet deforms, see, e.g., FIG. 3.8(c). This instability can be studied quantitatively by performing a linear stability analysis of the spherical symmetric stationary states found in the previous section. To this end, we study relaxation kinetics of spherical harmonics perturbations. We write

$$\phi_i^{I/\Pi}(r, \varphi, \vartheta, t) = \hat{\phi}_i^{I/\Pi}(r) + \delta\phi_i^{I/\Pi}(r, \varphi, \vartheta, t) \quad , \quad (4.16)$$

$$R(\varphi, \vartheta, t) = \hat{R} + \delta R(\varphi, \vartheta, t), \quad (4.17)$$

where $\hat{\phi}_i(r)$ are the volume fraction profiles of the stable solutions and \hat{R} is the stable droplet radius. Furthermore, we have introduced the perturbations $\delta\phi_i$ for the perturbation of the volume fraction profiles and δR , which is the perturbation of the interface. In spherical coordinates, the latter two depend on the radial coordinate r , and the azimuthal angle ϑ and the polar angle φ . Due to the linear nature of Eq. 4.1, we obtain the differential equations for the perturbations

$$\partial_t \delta\phi_i^{I/\Pi} = \sum_{j=1}^M \left(D_{ij}^{I/\Pi} \nabla^2 \delta\phi_j^{I/\Pi} + k_{ij}^{I/\Pi} \delta\phi_j^{I/\Pi} \right) \quad (4.18)$$

where all the constant terms in Eq. 4.1 are solved by the stationary solutions $\hat{\phi}_i^{I/\Pi}$. These coupled partial differential equations can be solved by using the ansatz

$$\delta\phi_i^{I/\Pi}(r, \varphi, \vartheta, t) = \sum_{n,l,m} \epsilon_{nlm} \varrho_{inl}^{I/\Pi}(r) Y_{lm}(\vartheta, \varphi) \exp(\tau_{nl} t) \quad , \quad (4.19)$$

$$\delta R(\varphi, \vartheta, t) = \sum_{n,l,m} \epsilon_{nlm} Y_{lm}(\vartheta, \varphi) \exp(\tau_{nl} t) \quad , \quad (4.20)$$

which separates this set of equations into a radial problem for r , an angular problem for φ and ϑ , and a temporal problem for t . This ansatz is a linear combination of modes to the problem, where the index $n = 0, \dots, \infty$ is related to the radial coordinate r , the index $l = 0, \dots, \infty$ is related to the polar angle φ , and the index $m = -l, \dots, l$ is related to the azimuthal angle ϑ . The amplitude of each mode is given by ϵ_{nlm} . The angular problem is solved by the spherical harmonics $Y_{lm}(\vartheta, \varphi)$, while an exponential function solves the temporal problem, where we have introduced the relaxation rate τ_{nl} . At the end, it is this relaxation rate which dictates if the mode m, n, l is stable $\tau_{nl} < 0$, or unstable $\tau_{nl} > 0$. The remaining spatial problem must be solved for all components i simultaneously. However, it is again a linear coupling of so-called Bessel problems. Thus, the solution is given by the summation of M linearly independent Bessel functions. Each Bessel function enters the component i with a different weight. Furthermore, each Bessel function comes in two forms, the first

and second kind. The boundary conditions at $r = 0$ and at the system's boundary determine which solutions are allowed. Here, the open and the closed system differ. For illustrative purposes, we show the solutions of a ternary mixture with $i = A, B$, in an open system. For the radial functions in Eq. 4.19, we make the ansatz

$$\begin{aligned} \varrho_{A_{nl}}^I(r) &= C_{1nl}^I i_l(r/\lambda_{1nl}^I) + C_{2nl}^I i_l(r/\lambda_{2nl}^I) \quad , \\ \varrho_{B_{nl}}^I(r) &= C_{1nl}^I \rho_{1nl}^I i_l(r/\lambda_{1nl}^I) + C_{2nl}^I \rho_{2nl}^I i_l(r/\lambda_{2nl}^I) \quad , \\ \varrho_{A_{nl}}^{II}(r) &= C_{1nl}^{II} k_l(r/\lambda_{1nl}^{II}) + C_{2nl}^{II} k_l(r/\lambda_{2nl}^{II}) \quad , \\ \varrho_{B_{nl}}^{II}(r) &= C_{1nl}^{II} \rho_{1nl}^{II} k_l(r/\lambda_{1nl}^{II}) + C_{2nl}^{II} \rho_{2nl}^{II} k_l(r/\lambda_{2nl}^{II}) \quad . \end{aligned} \quad (4.21)$$

In phase I, within the droplet, we use the modified spherical Bessel functions of the first kind $i_l(r)$, which ensure vanish gradients at $r = 0$. In phase II, the outside area, we use the modified spherical Bessel functions of the second kind $k_l(r)$, which ensure finite values at $r \rightarrow \infty$. In closed systems, a combination of the first and second kind has to be taken such that the flux vanishes at the system boundary. Here, we have to sum up two independent solutions since. As mentioned above, the time-dependent problem of any coupled linear reaction-diffusion system of M free components has M independent solutions. The independent solutions follow when using an ansatz of type Eq. 4.21, together with Eq. 4.19, in Eq. 4.18. We obtain the modified Bessel problems

$$\left(\partial_r r^2 \partial_r - \left(\frac{r^2}{\lambda^2} + l(l+1) \right) \right) b_l(r/\lambda) = 0 \quad , \quad (4.22)$$

where b_l is either i_l or k_l . For the ternary case, we are left with two equations from where we obtain

$$\lambda^2 = \frac{D_{AA}^{I/II} + \rho_{nl}^{I/II} D_{AB}^{I/II}}{k_{AA}^{I/II} + \rho_{nl}^{I/II} k_{AB}^{I/II} - \tau_{nl}} \quad (4.23)$$

from the differential equation for component A , and

$$\lambda^2 = \frac{D_{BA}^{I/II} + \rho_{nl}^{I/II} D_{BB}^{I/II}}{-k_{AA}^{I/II} - \rho_{nl}^{I/II} k_{AB}^{I/II} - \rho_{nl}^{I/II} \tau_{nl}} \quad (4.24)$$

from the differential equation for component B ⁴. The latter two equations have two independent solutions for $(\lambda_{nl}^{I/II})^2$ and ρ_{nl} , giving rise two the two contributions in Eq. 4.21. Therefore, we obtain four free coefficients $C_{1/2nl}^{I/II}$, which must be determined by boundary conditions at the interface. Furthermore, these interface conditions determine the relaxation rate τ_{nl} . Thus, five conditions are needed to fix the coefficients $C_{1/2nl}^{I/II}$ and τ_{nl} . In general, we have to determine again $2M + 1$ unknown values. They follow in linear order of perturbations to the interface condition stated in Eq. 4.11. In the linear problem, we can solve every mode independent from the

⁴Note, that even when all $k_{ij} = 0$, which is the case in phase II, we still have well-defined length-scales due to the existence of τ_{nl} . This ensures that we find always the right number of solutions in the dynamical problem, even in the absence of chemical reactions.

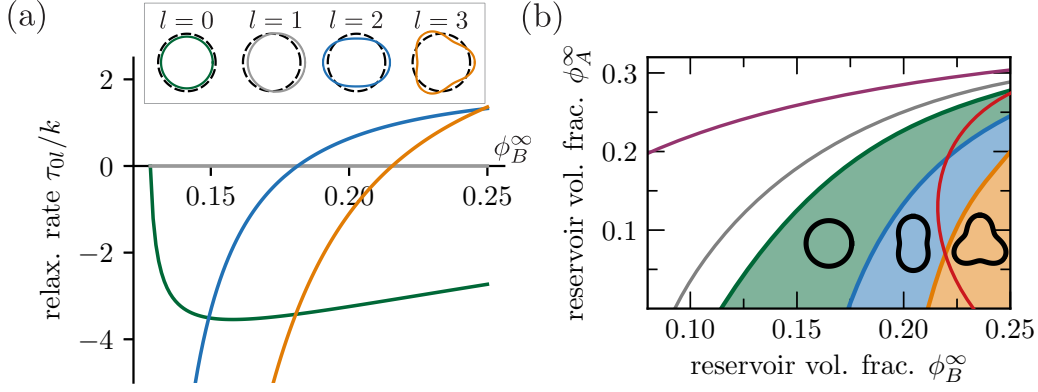


FIGURE 4.5: **Shape stability of chemically active droplets:** (a): The largest relaxations rates τ_{0l} of spherical harmonic deformations with $l = 0, \dots, 3$ are shown as functions of ϕ_B^∞ for $\phi_A^\infty = 0.05$. We show sketches of the perturbations in the inset (crosssections through the deformed spheres). (b): The same stability diagram as FIG. 4.3(d) is shown. Furthermore, we highlight domains with unstable $l = 2$ modes in blue and unstable $l = 3$ modes in orange. For parameters, see App. C.

other. Thus, every mode n, l, m has to obey

- perturbations of chemical potential balance between phases:

$$\sum_{j=1}^M \frac{\partial \bar{\mu}_i^I}{\partial \phi_j} \left(\partial_r \hat{\phi}_j^I(\hat{R}) + \varrho_{jnl}^I(\hat{R}) \right) = \sum_{j=1}^M \frac{\partial \bar{\mu}_i^{\Pi}}{\partial \phi_j} \left(\partial_r \hat{\phi}_j^{\Pi}(\hat{R}) + \varrho_{jnl}^{\Pi}(\hat{R}) \right), \quad M$$

- perturbation of the pressure condition:

$$\frac{\gamma(l^2 + l - 2)}{\hat{R}^2} = \sum_{i=1}^M \frac{\phi_i^I - \phi_i^{\Pi}}{\nu_i} \left(\sum_{j=1}^M \frac{\partial \bar{\mu}_i^{I/\Pi}}{\partial \phi_j} \left(\partial_r \hat{\phi}_j^{I/\Pi}(\hat{R}) + \varrho_{jnl}^{I/\Pi}(\hat{R}) \right) \right), \quad 1$$

- perturbation of the local conservation laws:

$$\tau_{nl} = - \frac{\sum_{j=1}^M \left[D_{ij}^I \left(\partial_r^2 \hat{\phi}_j^I(\hat{R}) + \partial_r \varrho_{jnl}^I(\hat{R}) \right) - D_{ij}^{\Pi} \left(\partial_r^2 \hat{\phi}_j^{\Pi}(\hat{R}) + \partial_r \varrho_{jnl}^{\Pi}(\hat{R}) \right) \right]}{\phi_i^I - \phi_i^{\Pi}}, \quad M$$

$$\frac{2M + 1}{(4.25)}$$

when using Eq. 4.19, where the amplitude of this mode ϵ_{nlm} , the spherical harmonics and the exponential function cancel in every line. Furthermore, we used that when a sphere of radius \hat{R} is perturbed with δR , its mean curvature is given by $H(\hat{R} + \delta R) = H(\hat{R}) + (l^2 + l - 2)\delta R/\hat{R}^2 + \mathcal{O}(\delta R^2)$, see [61, 62].

To demonstrate the outcome of this linear stability analysis, we show in FIG. 4.5(a) the stability of the ternary mixture of components A, B and S studied in the previous section. For this problem, the spatial solutions are given by Eq. 4.21. We show the numerical values of τ_{nl} with $n = 0$, corresponding to the longest length-scales, for $l = 0, \dots, 3$ as a function of ϕ_B^∞ for the system used for generating FIG. 4.3 and a fixed value of $\phi_A^\infty = 0.05$. Whenever we find a radially symmetric stable solution (see FIG. 4.3(c) blue line), the relaxation rate of modes with $l = 0$ (green line) are

always negative. These perturbations are radially symmetric and must therefore decay. Translations of the droplet correspond to the mode $l = 1$. Their relaxation rates are always zero (grey line) due to the infinite, radially symmetric system. However, in systems with high reservoir values ϕ_B^∞ , first modes with $l = 2$ (blue line) and latter modes with $l = 3$ (orange line) become unstable. Whenever these chemically active droplets are slightly deformed, these modes will always lead to elongations of the radially symmetric shape. In FIG. 4.5(b), we show the phase diagram of this system where we highlight the parameters with radially symmetric droplets in green, areas in which modes with $l = 2$ are unstable in blue, and areas where modes with $l = 3$ are unstable in orange. The results are consistent with the numerical study of a similar system in 2D in FIG. 3.12. For low values of ϕ_B^∞ , no spherical droplet can exist, even inside the binodal area. Increasing the reservoir value leads to stationary circular droplets. For even higher values of ϕ_B^∞ , the droplet becomes shape unstable and elongates.

4.4 Discussion

This chapter introduced a semi-analytical method for studying chemically active droplets quantitatively. Here, we focused on the dynamics of single droplets, as found in the nucleation-and-growth regime. Instead of solving the spatially continuous fourth-order partial differential equations introduced in the last chapter, we consider the limit of an infinitely sharp interface and couple two reaction-diffusion equations via a moving interface.

We showed how this method can be used to quantitatively study the existence and size of stationary droplets of spherical shape. In particular, we explored the stability diagram of boundary driven chemically active droplets in ternary mixtures. Dependent on the phase diagram and the chemical equilibrium line, stationary droplets can exist only inside the binodal area. Furthermore, we can explore the shape instabilities of these chemically active droplets by perturbing the stationary state and studying the relaxation kinetics of these perturbations.

Chapter 5

Models of protocells and their metabolism as chemically active droplets

Almost a hundred years ago, chemically active droplets were proposed as a potential step in the origin of life. Namely, Alexander Oparin [63], and John Haldane [64, 65] brought up the idea that droplets, that localized chemical reactions in the early oceans, could have been the first life-like objects on this planet. These droplets could have formed distinct chemical compartments that could compete in an evolutionary setting. Recently, a minimal model of such chemically active droplets in a binary mixture has been introduced [20]. The authors showed that in this binary mixture, a single chemically active droplet can undergo cycles of growth and division, leading to several droplets.

In this chapter, we introduce a protocell model of a quaternary mixture, where we take the dynamics of nutrients and waste explicitly into account¹. We discuss the stability of these droplets and study the energy and matter balance of these droplets. Following the ideas of Alexander Oparin, who defined “*the simplest but still complete prototype of metabolism*” as processes with “*absorption of substances from the surrounding medium, their assimilation and breakdown and the giving off of the products of their decomposition*” [67], the energetics of these chemically active droplets serve as simple models of protometabolism.

5.1 Breaking detailed balance in protocell models

To explicitly model the consumption of nutrients and the release of waste, we introduce a quaternary mixture composed of components $i = S, D, N, W$. These components are solvent S , droplet material D , nutrient N , and waste W . The droplet material D phase-separates from the solvent S , leading to droplets. Nutrient N can chemically convert to droplet material D , thereby feeding the droplet. Droplet material can undergo a chemical change to become waste W . These reactions can be

¹The main results of this chapter have been published here [66].

written as



and are indexed with $\alpha = 1, 2$. For simplicity, we consider that reactions involving the droplet material only occur inside the droplets. This is motivated by the idea that these reactions are enabled by catalysts that are absent outside and thus solely located inside droplets. Similar to the previous chapters, we distinguish two different scenarios of how phase separation organizes chemical reactions for making these systems active.

5.1.1 Boundary driven protocell models

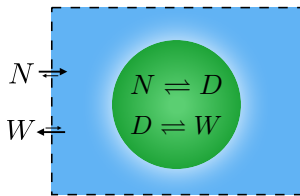


FIGURE 5.1

In the boundary-driven protocell models, we fix the volume fraction values of nutrient N , waste W , and droplet material D at the system boundary via concentration boundary conditions, see FIG. 5.1. This corresponds to the coupling of the system to reservoirs. These reservoir set values of the chemical potentials at the boundary $\bar{\mu}_i^\infty$. We choose conditions where $\bar{\mu}_N^\infty > \bar{\mu}_D^\infty > \bar{\mu}_W^\infty$ such that the direction of chemical reactions is from nutrient via droplet material to waste.

Therefore, nutrient will be provided, and waste will be absorbed by the reservoir. Thus, the free energy provided by the reservoir per consumed nutrient molecule is $\bar{\mu}_N^\infty - \bar{\mu}_W^\infty > 0$. This difference maintains the system out of equilibrium and drives a constant flux of molecules through the system. Under these chemical reactions, the only non-trivial conserved quantity in the system is $\psi = \phi_D + \phi_N + \phi_W$. It obeys the continuity equation, $\partial_t \psi + \nabla \cdot \mathbf{j}_\psi = 0$, where \mathbf{j}_ψ is the associated, conserved current. The conserved quantity is provided by the reservoir and can feed droplet growth. Therefore, droplet size is not limited by the conservation law.

5.1.2 Bulk driven protocell models

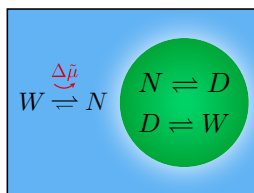
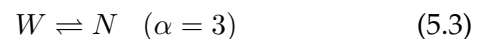


FIGURE 5.2

In the bulk-driven protocell models, we impose no-flux boundary conditions, considering that no exchange of molecules with reservoirs occurs at the boundaries, see FIG. 5.2. The system is maintained out-of-equilibrium by driving an additional chemical reaction



by an additional chemical energy $\Delta\tilde{\mu}$. For simplicity, we only allow this chemical reaction outside the

droplets in the bulk phase. This energy input could, for example, be provided by chemical fuel or by radiation. The energy input $\Delta\tilde{\mu}$ drives the reaction, which would spontaneously run from N to W in the opposite direction and allows nutrient to be recycled to waste. This can be achieved when $\Delta\tilde{\mu} + \bar{\mu}_W > \bar{\mu}_N$. The chemical reaction $\alpha = 3$ is linearly dependent on reactions $\alpha = 1, 2$. Thus, the same quantity $\psi = \phi_D + \phi_N + \phi_W$ is the only non-trivially conserved quantity in the system. Since there is no exchange at the boundaries, the amount of this conserved quantity ψ is fixed inside the system. Therefore, the amount of droplet material D is limited by the conserved quantity. This implies that even though free energy is constantly supplied via free energy $\Delta\tilde{\mu}$ to the system, the droplet size is limited by the conservation law.

5.2 Protocell dynamics

The latter case of bulk-driven protocell models can be compared to the minimal protocell model based on a binary system studied previously [20]. In this simple system, two components phase-separate from each other and can also be chemical converted into each other. Therefore, there is only one independent volume fraction in this binary system and no conservation law. Thus, droplet size is not limited by a conservation law. This previous work showed that these droplets can either shrink and disappear, grow until droplets reach a stable size, or undergo a shape instability and divide. In the latter case, cycles of growth and division can lead to many daughter droplets that together occupy an increasing volume.

As we will show in the following, our simple protocell models also exhibit regimes where droplets are stable with a finite size and regimes where droplets divide via a shape instability. Examples of droplet dynamics in the boundary-driven case are shown in FIG. 5.3 as snapshots of configurations of droplet material at different time points and for different nutrient reservoir volume fractions ϕ_N^∞ . For a small nutrient supply ($\phi_N^\infty = 0.04$), an initially prepared droplet tends to shrink as the waste released from the droplets exceeds the nutrient supply. For a larger nutrient supply ($\phi_N^\infty = 0.08$), an active droplet is stationary with a size that is determined by the nutrient supply. Increasing the nutrient supply further ($\phi_N^\infty = 0.13$), the droplet shape becomes unstable, and division occurs.

Solving these three coupled non-linear partial differential equations of fourth order is numerically costly. Therefore, we will use the effective description introduced in the last chapter to study these active droplet systems. Thus, we can quantitatively investigate the shrinkage, stationarity, growth, and division of protocells in these models.

5.2.1 Steady states droplets

The upper row of FIG. 5.4(a) shows profiles of volume fractions of droplet material D , nutrient N and waste W in the boundary driven case for a spherical droplet of size R as a function of the radial coordinate r . The droplet material is produced by

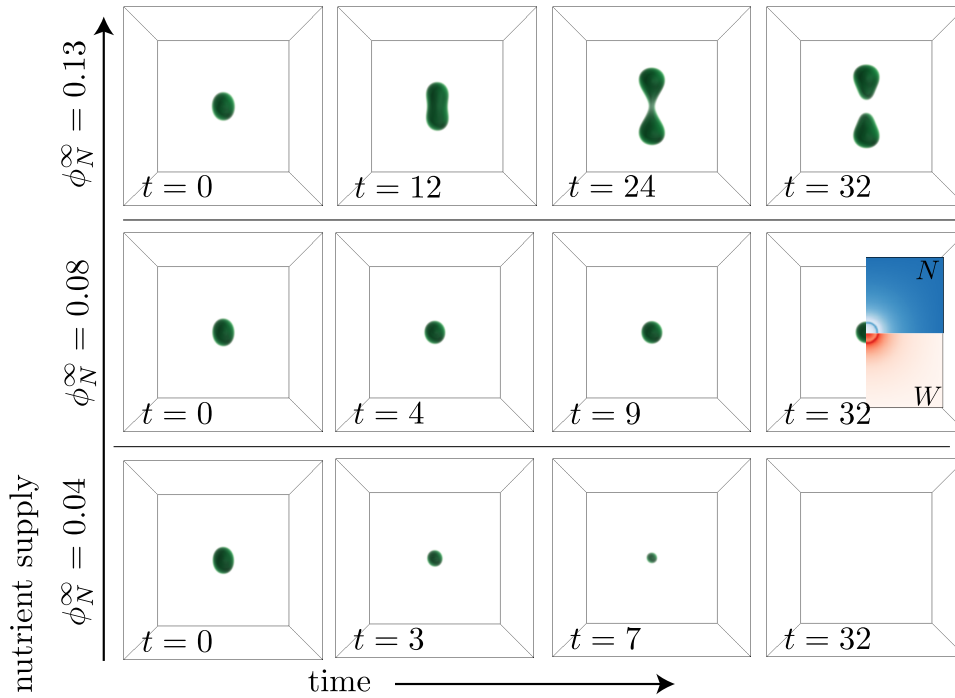


FIGURE 5.3: **Numerical study of a boundary driven chemically active droplet:** Volume fraction fields of droplet material ϕ_D for different time points t in boundary-driven systems for three values of ϕ_N^∞ are shown. The last panel in the middle row shows densities of ϕ_N and ϕ_W of a planar crosssection. Solutions were obtained by numerical integration of Eq. 3.1, and initializing a slightly elongated droplet at $t = 0$. For parameters and further details, see App. C.

reaction $\alpha = 1$ inside the droplet (gray region), where it is also the majority component. The droplet material also occurs outside at low concentrations. Nutrient is provided at large distances and diffuses toward the droplet. Waste is produced inside the droplet by the reaction $\alpha = 2$ and diffuses outwards. This can be seen by the profiles of the volume fraction fluxes (lower row). Outside the droplet, no reactions occur, and divergence-free fluxes couple the droplet to the reservoirs. In general, also fluxes of the droplet material exist. However, we have chosen reservoir values such that this flux almost vanishes. The system is maintained out-of-equilibrium by the concentration boundary conditions at infinity, where $\bar{\mu}_N \neq \bar{\mu}_W$. Note that detailed balance is obeyed everywhere in the system.

In the bulk-driven case, we impose that no-flux boundary conditions at infinity. With this, the reaction $\alpha = 3$ is at local chemical equilibrium with $\Delta\tilde{\mu} = \bar{\mu}_N - \bar{\mu}_W$, where $\Delta\tilde{\mu}$ is the chemical free energy supplied by a fuel. Note that the reaction $\alpha = 3$ occurs outside the droplet to regenerate nutrient from waste. The profiles of volume fractions of a steady state droplet are shown in FIG. 5.4(c), together with the corresponding currents. The profiles of volume fraction are qualitatively similar to the boundary-driven case shown in FIG. 5.4(a). The main difference is that the fluxes decay more quickly, and no net flux remains at infinity. Furthermore, the flux of the droplet material \mathbf{j}_D has to be strictly zero everywhere outside the droplet.

In the bulk-driven case, the steady state droplet radius depends on the concentrations imposed at infinity, see FIG. 5.4(b) which shows stationary radii of stable (solid

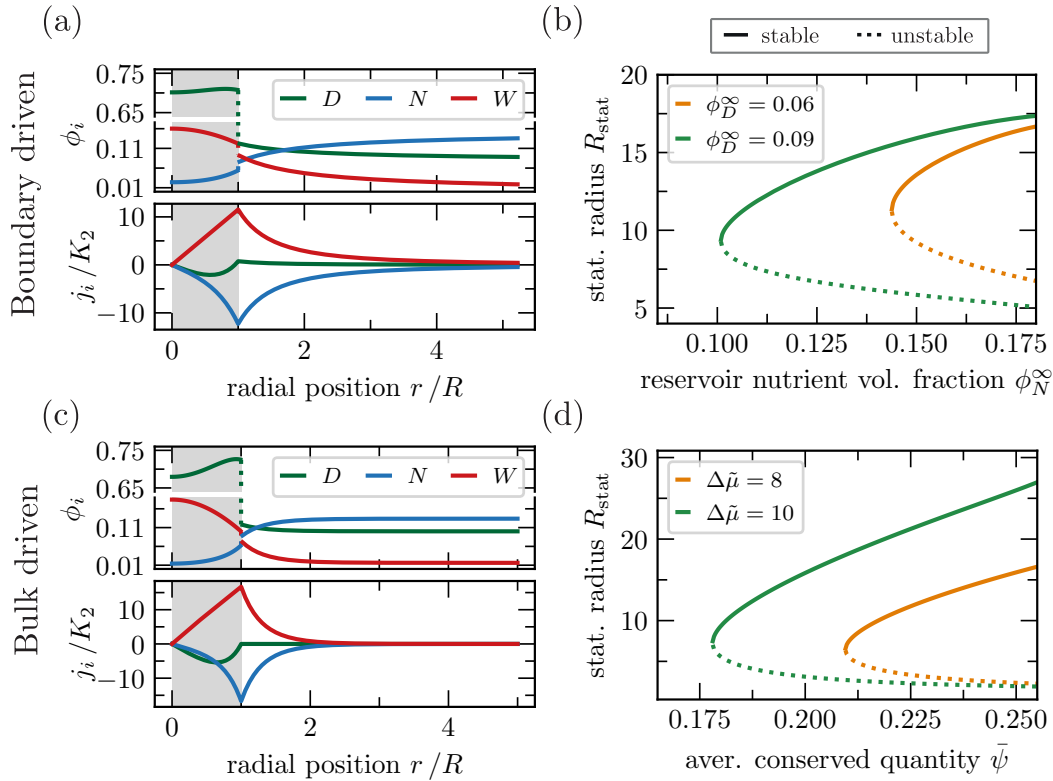


FIGURE 5.4: **Stationary protocells:** Spatial profiles of volume fractions and fluxes and the functional dependency of the stationary radius on the driving are shown. In the upper row for the boundary-driven case, while in the lower row for the bulk-driven case. (a,c): Exemplary profiles of volume fractions and corresponding diffusive fluxes for droplet material, nutrient and waste are shown. (b,d): Stable and unstable stationary radii R_{stat} of chemically active droplets are shown. For the boundary-driven case, R_{stat} is shown as a function of the nutrient volume fraction of the reservoir ϕ_N^∞ for two different reservoir values of the droplet material ϕ_D^∞ . For the bulk-driven case, R_{stat} is depicted as a function of the averaged conserved quantity $\bar{\psi}$ for two different values of external energy input $\Delta\tilde{\mu}$ that break detailed balance of the rates (1.35). For parameters and more details, see App. C.

lines) and unstable (dashed lines) droplets for two different values of ϕ_D^∞ as a function of ϕ_N^∞ . Droplets nucleated beyond the critical radius (dashed lines) grow until they reach the stable stationary radius (solid lines), while droplets larger than the stable radius shrink. For smaller volume fractions, ϕ_D^∞ droplet material is lost by diffusion towards infinity, requiring larger volume fractions ϕ_N^∞ to maintain the droplet.

For the bulk-driven case, the stable and unstable radii of stationary droplets are shown in FIG. 5.4(d). Here, as a function of the conserved quantity $\bar{\psi}^\infty$ and for two different values of $\Delta\tilde{\mu}$. Increasing the driving via $\Delta\tilde{\mu}$ enables chemically active droplets for smaller values of the conserved quantity $\bar{\psi}^\infty$ and leads to larger stable stationary droplets. This behavior is similar to that of the boundary-driven case, see FIG. 5.4(b). Increasing $\Delta\tilde{\mu}$ in the bulk-driven case has the same qualitative effect on the stationary radius as an increase of nutrient supply via ϕ_N^∞ in the boundary driven case, compare FIG. 5.4(b) and FIG. 5.4(d).

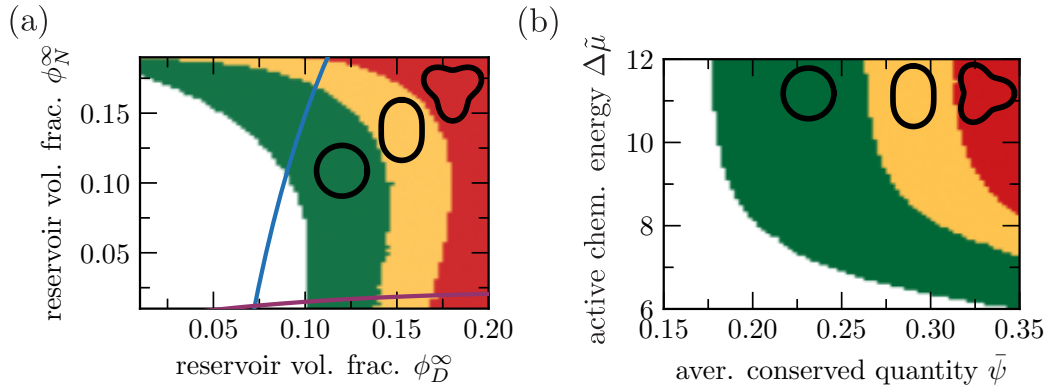


FIGURE 5.5: **Shape stability of protocells:** Stability diagrams for chemically active droplets for the boundary driven case in (a) and the bulk driven case (b) are shown. In the green area stationary droplets of spherical shape can exist. All shape perturbations decay. In the yellow area, the slowest $l = 2$ perturbation becomes unstable. Thus droplets elongate. In the red area, additionally, the slowest $l = 3$ mode becomes unstable. For the boundary driven case, we show the stability for a specific value of waste volume fraction of the reservoir, $\phi_W^\infty = 0.001$. Therefore, we can draw the chemical equilibrium line of reaction $\alpha = 1$ (purple) and the binodal line of these systems in the absence of chemical reactions (blue). For parameters, see App. C.

5.2.2 Shape stability of spherical symmetric droplets

So far, we have considered stationary droplets of spherical shapes. However, due to non-equilibrium conditions, chemically active droplets can also undergo a shape instability and take non-spherical shapes and thereby even divide. An example of a division event is shown in FIG. 5.3 (upper row). We can systematically study the linear stability of spherical shapes using the effective description in the sharp interface limit introduced in the last chapter.

In FIG. 5.5(a), we show a stability diagram of chemically active droplets for the boundary driven case as function of nutrient and droplet material volume fraction at infinity, ϕ_N^∞ and ϕ_D^∞ , for fixed ϕ_W^∞ . Stationary spherical droplets are stable within the green region of the diagram. However, within the yellow area, a spherical harmonic deformation mode with $l = 2$ is unstable. This corresponds to an elongation of the droplet shape. Similarly, in the red region, a spherical deformation mode with $l = 3$ is also unstable. In the white area, no stationary droplets exist. The figure shows, that starting from a stationary stable droplet, division can typically be induced by increasing the supply of either nutrient or droplet material. The binodal line of phase coexistence is shown as a solid blue line. In the absence of chemical reactions, droplets within the binodal region grow, while outside, they shrink. Chemical reactions also permit the existence of chemically active droplets outside of the binodal area, where droplet material is constantly lost towards the reservoir² Under such non-equilibrium conditions, the volume fractions at the interface (governed by the binodal) differ from the values imposed by boundary conditions at

²This only works in this quaternary mixture. The last chapter shows that stable chemically active droplets only exist inside the binodal area in a ternary mixture.

large distances. The solid purple line indicates the chemical equilibrium of reaction $\alpha = 1$, where the chemical rate r_α changes sign. For nutrient volume fractions above this line, droplet material is produced by the nutrient, while below this line, nutrient is produced.

Figure 5.5(b) shows the corresponding stability diagram for the bulk driven case as a function of the conserved density at infinity ψ^∞ and the active chemical free energy $\Delta\tilde{\mu}$. The same regions of stability are indicated: stable spherical droplets green, unstable mode with $l = 2$ yellow, and unstable mode with $l = 3$ red. Spherical stable droplets will typically divide when the conserved quantity is supplied, i.e., the conserved density ψ^∞ is increased. Moreover, for increasing values of $\Delta\tilde{\mu}$, the stability of active droplets becomes independent of $\Delta\tilde{\mu}$. This is because almost all waste is turned over into nutrient by the chemical reaction $\alpha = 3$.

5.3 Energetics of protocells

In our protocell models as chemically active droplets, we explicitly model the dynamics of nutrient and waste. As mentioned above, this provides us with simple models of the metabolic processes of such protocells. Therefore, we study the balance of matter and energy of chemically active droplets in this section.

5.3.1 Mass conservation and droplet growth or shrinkage

Like living objects, the chemically active droplets studied in this chapter are maintained away from equilibrium by fluxes of molecules. However, these fluxes lead to droplet shrinkage or growth, in general. However, when the incoming and outgoing fluxes are balanced, they only lead to the supply of free energy, which keeps the system away from equilibrium. To identify these two different behaviors, we can again use the concept of conserved and non-conserved quantities. In both cases of driving, we can identify the conserved quantity $\psi = \phi_D + \phi_N + \phi_W$. Furthermore, we can identify the variables $\xi_1 = -\phi_N$ and $\xi_2 = \phi_D + \phi_N - 2\phi_W$ as reaction extents in these systems. Droplet growth and shrinkage are governed by the dynamics of the conserved quantity, while fluxes of the reaction extents maintain the system out of equilibrium. To illustrate this, we show in FIG. 5.6 radial profiles of the conserved and non-conserved quantities and the corresponding fluxes at the stationary state for the boundary- and bulk-driven droplets shown in FIG. 5.4(a,c). To illustrate this, we show in FIG. 5.6 radial profiles of the conserved and non-conserved quantities (upper row) and the corresponding fluxes (lower row) at the stationary state for the boundary-driven (FIG. 5.6(a)) and bulk-driven droplets (FIG. 5.6(b)). The profiles of these quantities look similar between the cases, like the volume fraction profiles shown in FIG. 5.4(a,c). However, even for the boundary-driven case, the flux of the conserved quantity vanishes everywhere at the steady state. Reactions can not compensate for a flux of the conserved quantity. Thus, the droplet would have to shrink or grow. To maintain the system out of equilibrium, fluxes of the reaction extent occur inside and outside the droplet. These fluxes are again divergence-free in the

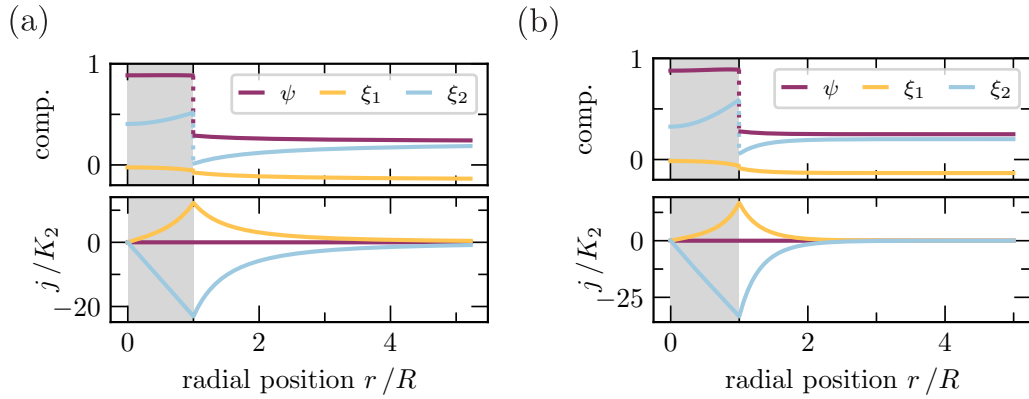


FIGURE 5.6: **Matter balance at the stationary state:** Radial profiles of the conserved quantity $\psi = \phi_D + \phi_N + \phi_W$ and the reaction extents $\xi_1 = -\phi_N$ and $\xi_2 = \phi_D + \phi_N - 2\phi_W$ are shown for the stationary droplets depicted in FIG. 5.4(a,c). For parameters and details, see App. C.

outside area in the boundary-driven case. In the bulk-driven case, they decay to zero for large distances, where reaction $\alpha = 3$ is at local chemical equilibrium with the additional supplied chemical energy.

5.3.2 Energy conservation and droplet heating or cooling

In the previous part, we have shown that fluxes of components with different chemical potentials can maintain droplets in a non-equilibrium steady state. In this section, we study the transport of energy explicitly. For this, also the transport of heat has to be taken into account. For simplicity, we focus on isothermal systems at constant temperature T and compute the heat flux transported away instantaneously, in the limit of an infinite heat conductance. We first derive this heat flux and the local entropy production rate for phase separating systems with chemical reactions, in general. Afterward, we come back to our protocell model and compute the flux of the released or absorbed heat from a heat bath at the boundary of the system. Phase separation and chemical reactions occur to lower the free energy $F = \int f dV$. Its local density (including the gradient terms) is denoted here by f . The density of the energy, $e = f + Ts$, can be decomposed into the free energy density and an entropy density $s = -\partial f / \partial T$. While the free energy gets lowered by the phase separation and chemical reactions, entropy has to increase to conserve the internal energy. The conservation of internal energy locally reads

$$\partial_t e + \nabla \cdot \mathbf{j}_h = -\nabla \cdot \mathbf{j}_q \quad , \quad (5.4)$$

where we split up the energy flux into an enthalpy flux \mathbf{j}_h , and a heat flux \mathbf{j}_q . The first is given by $\mathbf{j}_h = \sum_{i=1}^M h_i \mathbf{j}_i / \nu_i$, where we define the enthalpy $h_i = \bar{\mu}_i + T s_i$ per molecule of species i with $s_i = -\partial \bar{\mu}_i / \partial T$ denoting the entropy per molecule, and \mathbf{j}_i being the volume fraction flux. With this, Eq. 5.4 defines the heat flux³.

³For a more general discussion about defining heat fluxes in open systems, see [68]

The rate of change of internal energy density reads $\partial_t e = \sum_{i=1}^M h_i \partial_t \phi_i / \nu_i$. Using Eq. 5.4, we can identify the heat production rate as

$$\nabla \cdot \mathbf{j}_q = - \sum_{\alpha=1}^L r_\alpha \Delta h_\alpha - \sum_{i=1}^M \frac{\mathbf{j}_i}{\nu_i} \cdot \nabla h_i \quad , \quad (5.5)$$

where $\Delta h_\alpha = \sum_{i=1}^M \sigma_{i\alpha} h_i$ is the reaction enthalpy. Using the definitions of the entropy density s and energy density e , we obtain the entropy balance

$$\partial_t s + \nabla \cdot \mathbf{j}_s = \dot{\Theta} \quad , \quad (5.6)$$

where the entropy flux is $\mathbf{j}_s = \sum_{i=1}^M s_i \mathbf{j}_i / \nu_i + \mathbf{j}_q / T$. The entropy production rate $\dot{\Theta}$ obeys

$$T \dot{\Theta} = - \sum_{\alpha=1}^L r_\alpha \Delta \mu_\alpha - \sum_{i=1}^M \frac{\mathbf{j}_i}{\nu_i} \cdot \nabla \mu_i \quad , \quad (5.7)$$

which is zero or positive according to the second law of thermodynamics.

With these general equations at hand, we can compute the heat flux in our protocell models. While the entropy production of every process in Eq. 5.7 has to be positive, heat can be released or absorbed. Each term in Eq. 5.5 can have both signs under processes that minimize the free energy. Heat is released by chemical reactions if the reaction enthalpy $\Delta h_\alpha > 0$ (exothermic) and is absorbed by chemical reactions if $\Delta h_\alpha < 0$ (endothermic). In addition, heat is absorbed or released at the droplet interface (latent heat) for $\sum_i \mathbf{j}_i \cdot \nabla h_i > 0$ and $\sum_i \mathbf{j}_i \cdot \nabla h_i < 0$, respectively. Here, the sum is over all solute species.

Figures 5.7(a-d) present four scenarios that differ in the heat released by reactions and the heat released at the interface. For this example, we have chosen the reservoir values for a boundary-driven chemically active droplet such that the flux of droplet material is zero outside the droplet. In all four scenarios, the imposed chemical potentials at large distances start high for the nutrient, are lower for droplet material, and lowest for waste, $\bar{\mu}_N^\infty > \bar{\mu}_D^\infty > \bar{\mu}_W^\infty$. This biases reactions $\alpha = 1$ and $\alpha = 2$ in the forward direction, and diffusive transport and chemical reactions run in the same directions in all four scenarios.

The first scenario of exothermic reaction and latent heat release at the interface is shown in FIG. 5.7(a). It is characterized by the profiles of molecular enthalpies h_i (upper row) and total heat flux $\mathbf{J}_q = 4\pi r^2 \mathbf{j}_q$ (lower row). The nutrient enthalpy inside the droplet h_N^I (blue) is larger than the waste enthalpy h_W^I (red), indicative of a net exothermic reaction from N to W . In addition, FIG. 5.7(a) shows that at the interface $h_N^{II} - h_N^I > h_W^{II} - h_W^I$, corresponding to a net latent heat release. Here, index I refers to the droplet phase and II to the phase outside. The release of heat at a distance r corresponds to the slope of total heat flux $d\mathbf{J}_q/dr$. Heat release by chemical reactions corresponds to an increase of \mathbf{J}_q inside the droplet. The contribution of latent heat is captured by a discontinuity of \mathbf{J}_q at the interface.

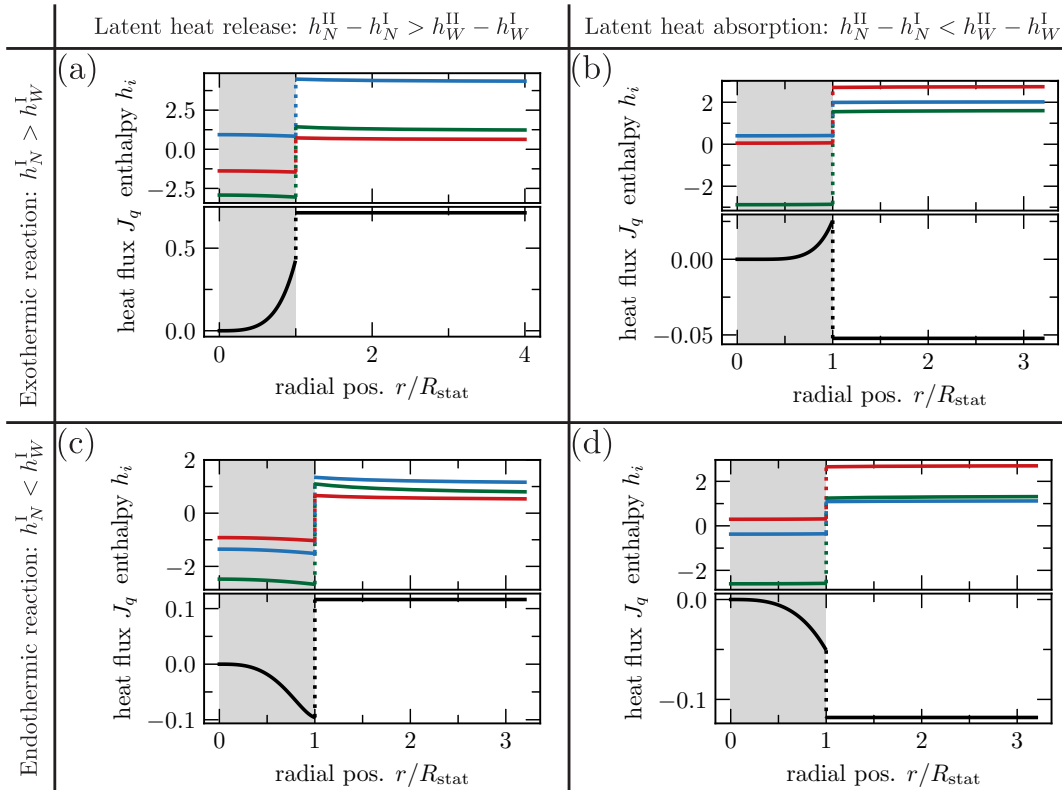


FIGURE 5.7: Heat flux in stationary protocells: We show the profiles of molecular enthalpies h_i for four different boundary driven stationary active droplets in the panels in the upper row of all figures (a-d). Despite the identical hierarchy of chemical potentials, $\bar{\mu}_N^\infty > \bar{\mu}_D^\infty > \bar{\mu}_W^\infty$, at the system boundary, these profiles differ. Thus the total heat flux $\mathbf{J}_q = 4\pi r^2 \mathbf{j}_q$ varies respectively (lower row). For simplicity, we have chosen ϕ_D^∞ such that the current of droplet material vanishes outside of the droplet in the steady state. Thus there is no flux of the droplet material over the interface at a stationary state, which would contribute to latent heat production or absorption. For parameters and details, see App. C.

There are three other additional scenarios are shown in FIG. 5.7: Exothermal reactions with latent heat absorption at the interface FIG. 5.7(b), endothermal reactions with heat release FIG. 5.7(c) and endothermal reactions with heat absorption FIG. 5.7(d). In the case of endothermal reactions, the enthalpy of the waste is higher than that of the nutrient, see FIG. 5.7(c,d) (upper row). In the case of latent heat absorption, \mathbf{J}_q drops at the interface, such that the heat generated inside the droplet by exothermic reactions is not fully transported to the outside FIG. 5.7(b). Finally, in the case of endothermic reactions and heat absorption at the interface, the system takes up heat, which enters at large distances and is absorbed by reactions inside the droplet, FIG. 5.7(d). The droplet, therefore, acts as a cooling device, which in the case of finite heat conductivity, could lead to lower temperatures inside the droplet compared to the outside.

5.4 Discussion

This chapter introduced a protocell model of chemically active droplets. These droplets are maintained away from equilibrium by the supply of nutrient and the removal of

waste. We distinguish between two different driving forms, boundary driven and bulk driven. In the first case, detailed balance is obeyed everywhere within the system and only broken by reservoirs at the system boundaries. In the latter case, we drive an additional chemical reaction outside the droplet for regenerating nutrient from waste. We showed that non-equilibrium steady states can exist and that for strong enough driving, chemically active droplets can divide in multi-component mixtures motivated by protocells.

In addition, we considered the balance of energy and matter. We showed that the growth or shrinkage of a chemically active droplet is governed by fluxes of the conserved quantities. However, non-equilibrium steady states are maintained by fluxes of the non-conserved reaction extents. This highlights the different roles of conserved densities ψ_j and of non-conserved reaction extents ξ_α for protocell dynamics. From the point of view that active droplets represent simple models for protocells, the chemical reactions inside the droplets represent a simple metabolism.

In biology, metabolic processes are classified as anabolic or catabolic. Anabolic processes are considered to build complex components from smaller units by consuming energy, while catabolism typically describes the break-up of complex molecules into smaller units by which energy is released. The reactions in our models of protocells can capture such anabolic and catabolic processes. As an example, we can consider nutrient and waste to be simple molecules of high and low internal energy, respectively. Droplet material D would then represent more complex components. In such a setting, the reaction $N \rightleftharpoons D$ ($\alpha = 1$) corresponds to anabolic processes, while the reaction $D \rightleftharpoons W$ ($\alpha = 2$) corresponds to catabolic processes.

A signature of the non-equilibrium state of living systems is the release of heat [69]. Our framework captures energy balance and heat exchange. Nutrients supply free energy via a high chemical potential compared to waste $\bar{\mu}_N > \bar{\mu}_W$, which drives the system out of equilibrium. Typically, nutrient N is also a molecular energy carrier and waste W , a low energy molecule that is reflected in molecular enthalpies ($h_N > h_W$). Active droplets are exothermic and release heat, see FIG. 5.7(a). However, protocells can also be endothermic if the molecular enthalpy of waste exceeds that of nutrient ($h_N < h_W$). In this case, the droplet would absorb heat from the environment, see FIG. 5.7(c,d). The latent heat of phase separation at the interface also enters this energy balance. Latent heat can be either released or absorbed, which leads overall to four different scenarios shown in FIG. 5.7. One of these scenarios shows that even if the droplet absorbs heat and appears to be endothermic, the reactions inside could still be exothermic, see FIG. 5.7(b). This shows that a measurement of overall heat absorption by an organism does not necessarily imply endothermic biochemistry. Therefore, our finding in this theoretical model is parallel to the proposed mechanism, leading to the measured heat uptake measured in bacteria [70, 71].

Chapter 6

The role of dimensionality on droplet division

A minimal model of chemically active droplets for protocells has been introduced by Zwicker et al. [20]. In this model, active chemical reactions in a binary phase-separating mixture can lead to droplet division. However, this only happens in three dimensions. In two-dimensional systems, independent of the number of components in the system, droplet division does not occur for driven chemical reactions. Droplets can elongate, leading to tubular structures¹, see FIG. 3.7(b) or FIG. 3.8(b). Only in boundary-driven systems droplet division can occur in small 2D systems, see FIG. 3.12(c). In the divergence-free gradients from the system boundaries, elongated droplets get pulled apart until they wet the boundary. Nevertheless, these systems have to be small due to the logarithmic decay of the volume fraction profiles, which are the solution of the corresponding Laplace equation. In this system, typically, only one division event can occur.

The aim of this chapter is, first, to explain the cause of the different behavior between 2D and 3D systems. Second, to build a minimal model that shows cycles of droplet growth and division in 2D. The primary motivation is that solving these fourth-order partial differential equations in 3D is numerically costly. By lowering the dimensionality of the system, much larger systems can be simulated with not only tens, but hundreds or thousands of droplets. This hopefully opens the door for further investigations of chemically active droplets as models for protocells. Therefore, we will introduce a mechanism that can robustly lead to droplet division in 2D. This mechanism is built on chemical reactions at the interface, dependent on its mean curvature. However, the study of chemical reactions at the interface of droplets is an interesting problem in itself.

¹Division in 2D was reported under specific initial condition when also noise was taken into account in the dynamics, see [72].

6.1 Stability of chemically active droplets in 2D vs. 3D

For building a minimal model, we will use the binary system introduced by Zwicker et al. [20]. Here, we will shortly introduce it and explain, with this model, the difference in the stabilities between 2D and 3D. The local composition of binary mixtures is entirely described by just the volume fraction of just one component. In the following, we consider a mixture of components A and B , which phase-separate from each other and can chemically convert into each other. We use the volume fraction of B , denoted as ϕ in the following, to describe the composition. Furthermore, the equilibrium values $\Phi_0^{I/II}$ of phase separation in an infinite system are independent of the total composition in the system. As long as the average composition $\bar{\phi}$ stays within these values, replacing A with B or vice versa only changes the phase volumes. Therefore, we will use, in contrast to the rest of this thesis, the Ginzburg-Landau free energy

$$f(\phi) = \frac{b}{2\Delta\phi} \left(\phi - \Phi_0^I\right)^2 \left(\phi - \Phi_0^{II}\right)^2 \quad (6.1)$$

as free energy density in Eq. 1.1, where $\Delta\phi = \Phi_0^I - \Phi_0^{II}$, and b characterizes the molecular interaction strength. It can be understood as the expansion of a binary free energy density close to the critical point, see [73]. For this free energy density, the exchange chemical potential $\bar{\mu}$ of component B reads

$$\bar{\mu} = \frac{b}{\Delta\phi} \left(\phi - \Phi_0^I\right) \left(\phi - \Phi_0^{II}\right) \left(2\phi - \Phi_0^I - \Phi_0^{II}\right) - \kappa\nabla^2\phi \quad (6.2)$$

This chemical potential drives the diffusive fluxes. With the Ginzburg-Landau free energy, we can use a constant mobility coefficient Γ , without obtaining any singularities for any dilute case. Thus we can write

$$\partial_t\phi = \gamma\nabla^2\bar{\mu} + r \quad (6.3)$$

which is the reduced form of Eq. 3.2. However, due to simplicity, the authors of [20] directly assumed a linear dependency in each phase, which makes the system active. For this, they used

$$r = \begin{cases} -k^{II}(\phi - \Phi_0^{II}) + c^{II}, & \phi \leq \phi_c^+, \\ p(\phi), & \phi_c^+ < \phi < \phi_c^-, \\ -k^I(\phi - \Phi_0^I) - c^I, & \phi \geq \phi_c^- \end{cases}, \quad (6.4)$$

thus two linear regimens connected by a fourth-order polynomial $p(\phi)$, ensuring a smooth interpolation. If $c^{I/II} > 0$, B material is degraded below the equilibrium value Φ_0^I within the B -rich droplet with the turnover c^I and produced above equilibrium value Φ_0^{II} in the outside area until ϕ reaches the supersaturation $\epsilon = c^{II}/k^{II}$. This implicitly assumes the same breaking of detailed balance by an additional fuel component, as previously studied in this thesis. Zwicker et al. [20] studied this

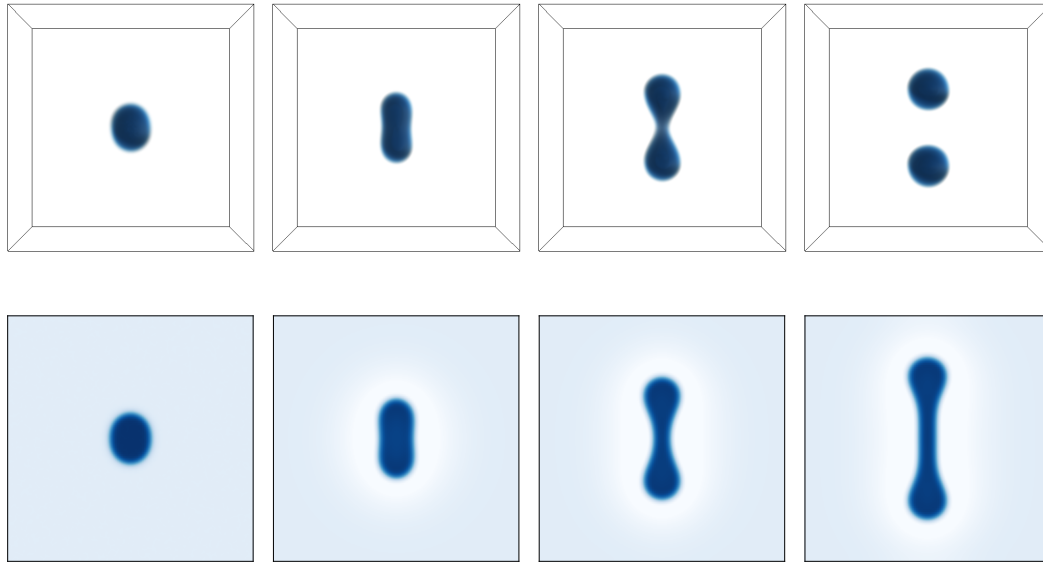


FIGURE 6.1: **3D vs. 2D - elongation and division:** We show snapshots of volume fraction fields obtained by solving Eq. 6.5 numerically. A three-dimensional system is shown in (a), while in (b), a two-dimensional system. In both cases, the chemically active droplet elongates. However, only in 3D does the formed neck pinch off, leading to a division. In 2D, a stable neck is formed. For the parameter settings, see App. C.

model in detail and showed that these chemically active droplets can undergo cycles of growth and division numerically in 3D. Furthermore, they studied the shape instability when small deformation of spherical chemically active droplets become unstable, leading to further elongation.

In FIG. 6.1(a), we show snapshots of volume fraction fields of numerical solutions of this model. In the upper row, we solve this model in a three-dimensional system. Here, a slightly elongated droplet elongates further, and the formed neck shrinks until it finally pinches off. Identical to the results of Zwicker et al. However, solving Eq. 6.3 in a two-dimensional system with the parameters leading to similar droplet radii, see FIG. 6.1(b), the droplet elongates, builds a neck of fixed size, and never pinches off. This behavior is robust; thus, a division of a chemically active droplet, driven by phase-specific driving, never occurs in 2D. However, the authors of [72] reported a division event in a noise version of this model for very elongated droplets. A quantitative study of the pinch-off instability of a formed neck and comparing the 2D case with the 3D case is missing in the literature. Therefore, we revisit the elongation stability of spherical chemical active droplets in 3D, as performed in [20], and compare it two the 2D stability of circular chemical active droplets. Then, we study the stability of a cylindrical shape in 3D and compare it two the stability of a rectangular shape in 2D. With this, we obtain insights into the pinch-off instability.

6.1.1 Stationary droplets in 1D, 2D and 3D

A considerable advantage of dealing with binary mixtures is that the equilibrium volume fractions $\Phi_0^{I/\text{II}}$ in infinite systems are independent of the average composition. In the multicomponent mixture, we linearized Eq. 3.1 around not previously known volume fractions. These values were only determined self-consistently at the end, see Section 4.2. In a binary mixture, however, we can use the known equilibrium values of infinite systems $\Phi_0^{I/\text{II}}$ to linearize Eq. 3.1. For deriving Eq. 6.3, we used the composition-independent mobility coefficient γ . For the given free energy density Eq. 6.1 the diffusion coefficients in each phase, as defined in Eq. 1.11, are composition independent $D^{I/\text{II}} = D$ and read $D = \gamma b$, while the reaction fluxes are linear by construction. Thus, the linear problem of Eq. 6.3 in each phase read

$$\partial_t \phi^{I/\text{II}} = D \nabla^2 \phi^{I/\text{II}} - k^{I/\text{II}} \left(\phi^{I/\text{II}} - \Phi_0^{I/\text{II}} \right) \mp c^{I/\text{II}} \quad , \quad (6.5)$$

which we can solve, once we know the interface volume fractions. Identical to Section 4.2, we assume the equilibrium of phase separation at the interface. These values differ from $\Phi_0^{I/\text{II}}$ due to the Laplace pressure contribution for a droplet of finite size R , see FIG. 1.1. However, in a small surrounding of these values, we can approximate these effects by using

$$\phi^{I/\text{II}}(R) = \Phi_0^{I/\text{II}} + \gamma \beta^{I/\text{II}} H(R) \quad , \quad (6.6)$$

where the mean curvature $H(R) = 2/R$ in 3D, $H(R) = 1/R$ in 2D, and $H(R) = 0$ in 1D. In the binary mixture with our choice of the free energy density, even the surface tension becomes composition-independent and can be derived as $\gamma = \Delta \phi^2 \kappa b / 6$, in the same way as done in App. B for multicomponent mixtures. The coefficients $\beta^{I/\text{II}}$ are coming from the so-called Gibbs-Thomson relations, see [73]. In our given system, they are identical in both phases, thus $\beta^{I/\text{II}} = \beta$, and are given in our system by $\beta = 1/(b \Delta \phi)$ in our system. The idea behind the underlying approximation is to use two parabolas around $\Phi_0^{I/\text{II}}$, instead of the entire function $f(\phi)$ for constructing the tangents with identical slopes, see [73].

Thus, the stationary solution of Eq. 6.5 for a B -rich droplet of radius R is given by

$$\phi^I(r) = \left(\beta \gamma H(R) + \frac{c^I}{k^I} \right) \left(\frac{\varrho^I(r/\lambda^I)}{\varrho^I(R/\lambda^I)} - 1 \right) + \Phi_0^I + \beta \gamma H(R) \quad , \quad (6.7)$$

$$\phi^{\text{II}}(r) = \left(\beta \gamma H(R) - \frac{c^I}{k^{\text{II}}} \right) \left(\frac{\varrho^{\text{II}}(r/\lambda^{\text{II}})}{\varrho^{\text{II}}(R/\lambda^{\text{II}})} - 1 \right) + \Phi_0^{\text{II}} + \beta \gamma H(R) \quad , \quad (6.8)$$

with the reaction-diffusion length scale $\lambda^{I/\text{II}} = \sqrt{D/k^{I/\text{II}}}$. The spatial dependency is captured by the functions $\varrho^{I/\text{II}}(r)$. In 3D, these functions are given by the modified spherical Bessel functions of the first and second kind and zeroth order, $\varrho^I(r) = \sinh(r)/r$ and $\varrho^{\text{II}}(r) = \exp(-r)/r$. In 2D, the modified Bessel functions of the first and second kind and zeroth order $\varrho^I(r) = I_0(r)$ and $\varrho^{\text{II}}(r) = K_0(r)$ have to be used, while in 1D, $\varrho^I(r) = \cosh(r)$ and $\varrho^{\text{II}}(r) = \exp(-r)$. The one-dimensional case is

needed for studying the pinch-off instability. For the two- and three-dimensional systems, we show exemplary volume fraction profiles in FIG. 6.2(a). At the interface, the slightly higher Laplace pressure in 3D leads to higher volume fraction values. The radial profiles in the phases differ too. Besides having the same value far away from the droplet, in 2D, diffusion leads to weaker gradients in the outside area. Thus less B -material is provided for identical parameters.

We can derive the fluxes $j^{I/II}(R)$ at the interface from these profiles. Even though this system is equivalent to a phase-driven system, we can use Eq. 4.11, as used in the open systems, for computing the interface velocity dR/dt . The interface can move because, in a binary system, the only conserved quantity is trivially conserved. FIG. 6.2(b) shows that, when the supersaturation is high enough, two stable radii exist, similar to FIG. 4.3(b). The smaller one is the critical radius for nucleation, while the larger corresponds to a chemically active droplet of fixed size. Interestingly, the supersaturation level at which stable droplets can exist is almost identical between the two- and three-dimensional systems. However, the values of these stationary radii differ. Due to the smaller Laplace pressure, the critical nucleation radius is smaller in 2D than in 3D. However, the stable droplet radius is also smaller in 2D than in 3D due to the weaker diffusive fluxes. We show the dependencies of these radii on the supersaturation for a specific value turnover in FIG. 6.2(c).

6.1.2 Elongation instability

The stability analysis of slightly deformed droplets in 3D shows that these droplets can be shape unstable, see [20]. We perform the same stability analysis and compare it to the two-dimensional elongation instability derived analogously. We perturb radial symmetric spherical droplets with radius R equal to the stable radius \hat{R} , as described above, and study the relaxation rate of this perturbation. Therefore, we write

$$\begin{aligned}\phi^{I/II}(r, \varphi, \vartheta, t) &= \hat{\phi}^{I/II}(r) + \delta\phi^{I/II}(r, \varphi, \vartheta, t) \quad , \\ R(\varphi, \vartheta, t) &= \hat{R} + \delta R(\varphi, \vartheta, t) \quad ,\end{aligned}\tag{6.9}$$

where the ϑ dependency vanishes for the two-dimensional case, and $\hat{\phi}$ is the stationary volume fraction profile. Similar to Section 4.3, the linear problem in Eq. 6.5 can be solved, when using the separation ansatz

$$\begin{aligned}\delta\phi^{I/II}(r, \varphi, c, t) &= \sum_{n,l,m} \epsilon_{nlm} A_{nlm}^{I/II} \varrho_l^{I/II}(r/\lambda_{nl}^{I/II}) Y_{ml}(\vartheta, \varphi) \exp(\tau_{nl} t) \quad , \\ \delta R(\varphi, \vartheta, t) &= \sum_{n,l,m} \epsilon_{nlm} Y_{ml}(\vartheta, \varphi) \exp(\tau_{nl} t) \quad ,\end{aligned}\tag{6.10}$$

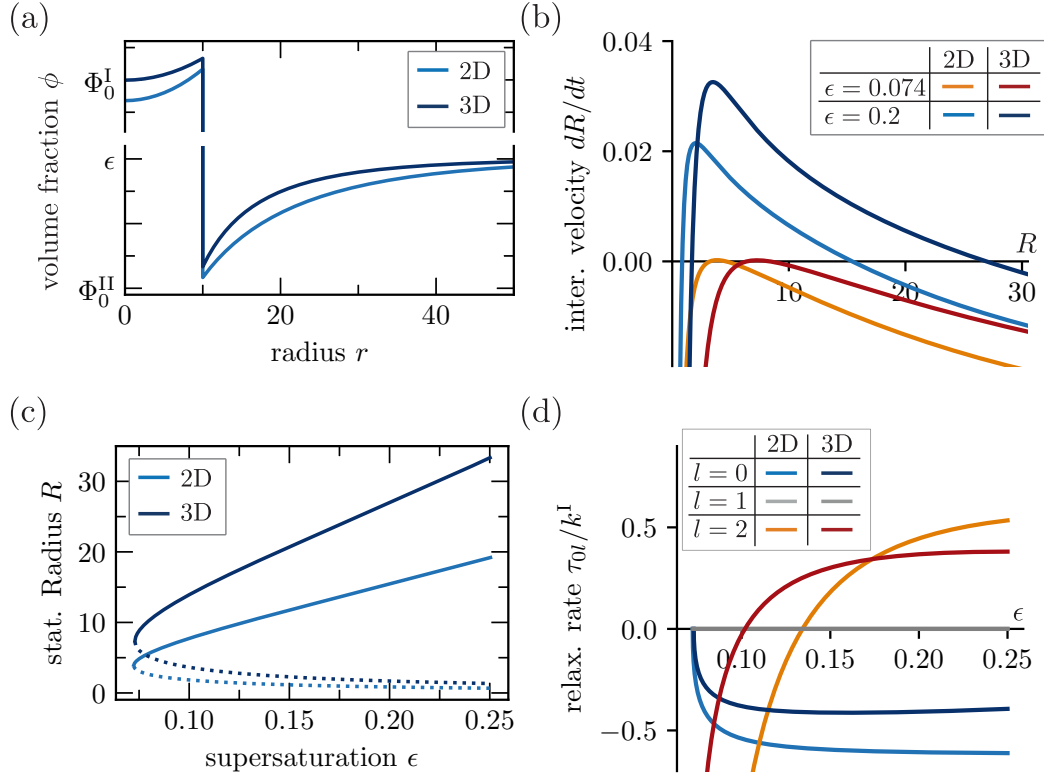


FIGURE 6.2: **2D vs. 3D - stable droplet radii and elongation instability:** We show radial profiles of the volume fraction ϕ in (a), in the sharp interface limit for spherical droplets (3D) or circular droplets (2D). For different interface positions, the droplet grows or shrinks, see (b), where we show dR/dt as a function of R . For large enough supersaturations ϵ , the dR/dt -curve has two roots, forming one stable and one unstable stationary radius appears, see (c). However, chemically active droplets with the stationary radius can still be shape unstable. We show the relaxation rate of the largest modes of form stated in Eq. 6.10 (3D) or Eq. 6.11 in (d). For $\tau_{0l} > 0$, any perturbation of this form will exponentially grow. see App. C.

in 3D, when $\varrho_l^I(r) = i_l(r)$ and $\varrho_l^{II}(r) = k_l(r)$ are the modified spherical Bessel function of first and second kind of order l . In 2D, we use

$$\begin{aligned} \delta\phi^{I/II}(r, \varphi, t) &= \sum_{n,l} \epsilon_{nl} A_{nl}^{I/II} \varrho_l^{I/II}(r/\lambda_{nl}^{I/II}) \cos(l\varphi) \exp(\tau_{nl}t) \quad , \\ \delta R(\varphi, t) &= \sum_{n,l} \epsilon_{nl} \cos(l\varphi) \exp(\tau_{nl}t) \quad , \end{aligned} \quad (6.11)$$

when $\varrho_l^I(r) = I_l(r)$ and $\varrho_l^{II}(r) = K_l(r)$ are the modified Bessel function of first and second kind of order l . In both solutions, $\lambda_n^{I/II} = \sqrt{D/(k^{I/II} + \tau_{nl})}$ and ϵ_{nlm} is the amplitude the mode corresponding to the indices n, l, m in 3D. In 2D the index m has to be dropped. The perturbation of the boundary conditions in Eq. 6.6 determine the coefficients $A_{nlm}^{I/II}$ via

$$\delta\phi^{I/II}(\hat{R}, \varphi, \vartheta, t) = \left(\beta\gamma\delta H - \partial_r \hat{\phi}(\hat{R}) \right) \delta R(\varphi, \vartheta, t) \quad (6.12)$$

for each mode n, l, m . Here, the change of mean curvature is $\delta H = (l^2 + l - 2)/\hat{R}^2$ in 3D and $\delta H = (l^2 - 1)/\hat{R}^2$ in 2D. In the latter case, the ϑ dependence vanishes

again. Thus, finally, the relaxation rate τ_{nl} can be computed from the condition

$$\tau_{nl} = -D \frac{\partial_r^2 \hat{\phi}^I(\hat{R}) + A_{nlm} \partial_r \rho^I(r/\lambda_{nl}^I) - \partial_r^2 \hat{\phi}^{II}(\hat{R}) - A_{nlm} \partial_r \rho^{II}(r/\lambda_{nl}^{II})}{\hat{\phi}^I(\hat{R}) - \hat{\phi}^{II}(\hat{R})} . \quad (6.13)$$

In FIG. 6.2(d), we show the the slowest ($n = 0$) relaxation rates τ_{nl} for $l = 0$, $l = 1$, and $l = 2$ for the two- and three-dimensional systems. Their shapes look qualitatively identical. The spherical symmetric perturbations with $l = 0$ are always stable when perturbing the stationary stable droplet. Both systems are translational symmetric. Thus, the relaxation rate of the mode $l = 1$ is always 0. For high enough supersaturations, the $l = 2$ modes become unstable. Thus, these chemically active droplets elongate. However, higher supersaturation levels are needed to see this elongation in the two-dimensional case.

6.1.3 Pinch-off instability

The pinch-off instability can be investigated when a cylinder in 3D or a rectangular shape in 2D of height L is perturbed in the z direction. These shapes represent the emerging neck when a chemically active droplet elongates. First, we solve for the stable radius or the cylinder in 3D, identical to the stable droplet radius of a 2D system², and for the width of the rectangular shape at which it becomes stable. We call the half of this width radius. Again, we search for the roots of the interface velocities. Due to the absence of a Laplace pressure of the flat interface, there is no critical nucleation radius, and a stable radius exists for supersaturations $\epsilon > 0$. To illustrate this, we show in FIG. 6.3(a) the interface velocity dR/dt as a function of its position R for $\epsilon = 0.2$ and in FIG. 6.3(b) the dependency of the roots of these functions on the supersaturation ϵ .

We perturb these cylindrical or rectangular shapes with stable radius \hat{R} with

$$\begin{aligned} \phi^{I/II}(r, \varphi, z, t) &= \hat{\phi}^{I/II}(r) + \delta\phi^{I/II}(r, \varphi, z, t) , \\ R(\varphi, z, t) &= \hat{R} + \delta R(\varphi, z, t) , \end{aligned} \quad (6.14)$$

where the φ dependency vanishes for the two-dimensional case, and $\hat{\phi}$ is the stationary volume fraction profile. The ansatz for the perturbation which solves the differential equation reads for the cylindrical shape

$$\begin{aligned} \delta\phi^{I/II}(r, \varphi, z, t) &= - \sum_{n,l,m} \epsilon_{nlm} A_{nlm}^{I/II} \rho_l^{I/II}(r/\lambda_{nlm}) \cos(l\varphi) \cos\left(\frac{2\pi mz}{L}\right) \exp(\tau_{nlm}t) , \\ \delta R(\varphi, z, t) &= - \sum_{n,l,m} \epsilon_{nlm} \cos(l\varphi) \cos\left(\frac{2\pi mz}{L}\right) \exp(\tau_{nlm}t) , \end{aligned} \quad (6.15)$$

²As seen already in FIG. 6.2(b), whenever a stable droplet radius exists in 3D, also in a two-dimensional system, a stable droplet can exist. Therefore, it cannot happen that a droplet in 3D elongates, and we cannot study the stability of the emerging neck.

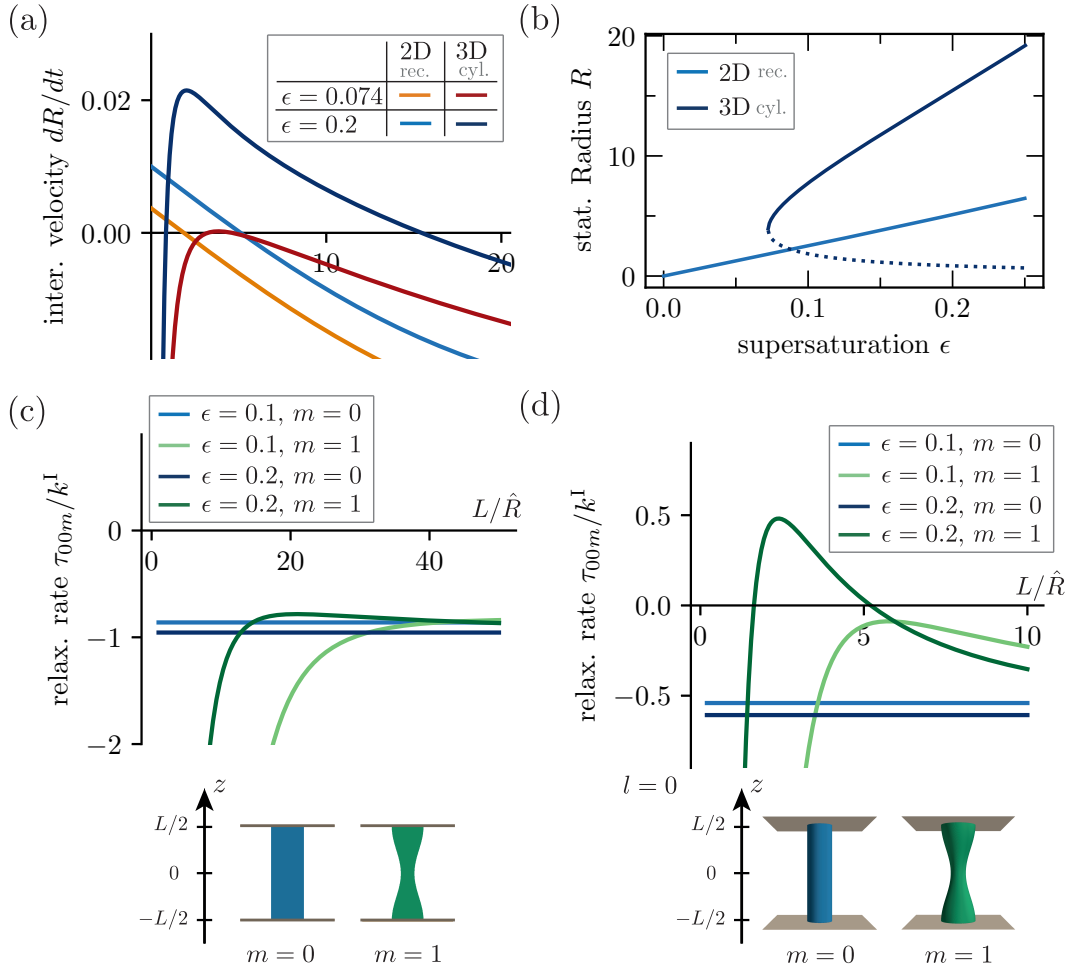


FIGURE 6.3: **2D vs. 3D - pinch-off stability:** In (a), the interface velocity dR/dt is shown as a function of R for cylindrical droplets in (3D) or rectangular droplets in (2D) between two parallel plates, see sketch at the bottom of (c) or (d) ($m = 0$). For cylindrical droplets, there exists a critical supersaturation ϵ below which no stationary cylinders can be found. However, in 2D, for any finite supersaturation ϵ , a stationary rectangular droplet can be formed, see (b). In (c) and (d), we show the relaxation rate of shape perturbations of rectangular droplets in 2D or cylindrical droplets in 3D of the stationary radius as a function of the distance of two plates (no-flux boundary condition) of distance L/\hat{R} , where \hat{R} is the stationary droplet radius (see sketch at the bottom with $m = 1$). For large supersaturations, perturbations to the cylindrical droplet can become shape unstable for $L \geq 2.5$. However, the perturbations of a rectangular droplet in 2D always decay. For further parameters, see App. C.

where $\varrho_l^I(r) = I_l(r)$ and $\varrho_l^{II}(r) = K_l(r)$ are the modified Bessel function of first and second kind of order l . For the rectangular shape, we use

$$\begin{aligned} \delta\phi^{I/II}(r, z, t) &= - \sum_{n,m} \epsilon_{nm} A_{nm}^{I/II} \varrho^{I/II}(r/\lambda_{nm}) \cos\left(\frac{2\pi mz}{L}\right) \exp(\tau_{nm}t) \quad , \\ \delta R(z, t) &= - \sum_{n,m} \epsilon_{nm} \cos\left(\frac{2\pi mz}{L}\right) \exp(\tau_{nm}t) \quad , \end{aligned} \quad (6.16)$$

where $\varrho^{\text{I}}(r) = \cosh(r)$ and $\varrho^{\text{II}}(r) = \exp(-r)$. In both cases, the reaction-diffusion length scale reads

$$\lambda_{nlm}^{\text{I/II}} = \sqrt{\frac{D}{k^{\text{I/II}} + \tau_{nlm} + \frac{4\pi^2 m^2 D}{L^2}}} \quad , \quad (6.17)$$

and ϵ_{nlm} is the amplitude this mode. The index l is dropped for the two-dimensional case. The coefficients $A_{nlm}^{\text{I/II}}$ are determined again by the boundary condition of the perturbation Eq. 6.12. Only the change of mean curvature differs for these perturbations. For the perturbed cylinder, it reads $\delta H = (l^2 - 1)/\hat{R}^2 + 4\pi^2 m^2/L^2$, while for the perturbed rectangle, it reduces to $\delta H = 4\pi^2 m^2/L^2$. The remaining τ_{nlm} can be most easily computed again via Eq. 6.13. The remaining τ_{nlm} can be most easily computed via Eq. 6.13, when $z = 0$. Here, the normal flux at the interface is only in the radial direction. Therefore, we can compute the relaxation rate of such perturbations for any given height L of the cylinder or the rectangle.

We show the slowest ($n = 0$) relaxation rates as a function of L for two different supersaturation levels in a FIG. 6.3(c) for a 2D system and in FIG. 6.3(d) for a 3D system. Here, the $m = 0$ modes are always stable and independent of L as expected from a radial symmetric stable droplet. However, the $m = 1$ mode can become unstable when the supersaturation is high enough in three-dimensional systems. Thus the cylinder becomes unstable depending on its length L . We find that this instability can occur approximately when $L > 2\hat{R}$. Then, the relaxation rates have a maximum around $L \approx 2.5\hat{R}$ and become stable for $L \gg \hat{R}$. However, here perturbations with higher m 's become unstable again.

In two-dimension systems, however, the rectangular shape is always stable. The main reason for this difference between 2D and 3D systems stems from the different mean curvature changes. For simplicity, let us compare the mean curvature change at $z = 0$, thus a minimum radius of the cylinder or rectangle $R = \hat{R} - \epsilon$, to positions $z = \pm L/2$, where the radius is maximal $R = \hat{R} + \epsilon$. In 2D, the only axis of principle curvature is in z direction, and the mean curvature has the same absolute value at all three positions. However, in 3D, the radial direction (in the $x - y$ plane) also contributes to the mean curvature. Here, the position at $z = 0$ has a higher absolute mean curvature due to its smaller radius.

Finally, we can draw the corresponding stability diagrams FIG. 6.4. For the two-dimensional system (FIG. 6.4(a)), we find an area where radial symmetric droplets can exist (blue) and an area in which the chemically active droplets always are unstable under small perturbations and elongate (orange). However, these droplets never divide due to the stable neck. This behavior is similar to that of the Plateau-Rayleigh instability, which leads to the formation of many small droplets when the radius of a liquid jet becomes to small. A two-dimensional jet does not pinch-off either, see [74]. In the three-dimensional case (FIG. 6.4(b)), the line of stable droplets (blue) is almost identical to the 2D case. However, the elongation instability already occurs for lower supersaturations (red).

Furthermore, we find a third area (green) at which the neck becomes unstable and the droplets can pinch off. Therefore, we find a large area in the stability diagram

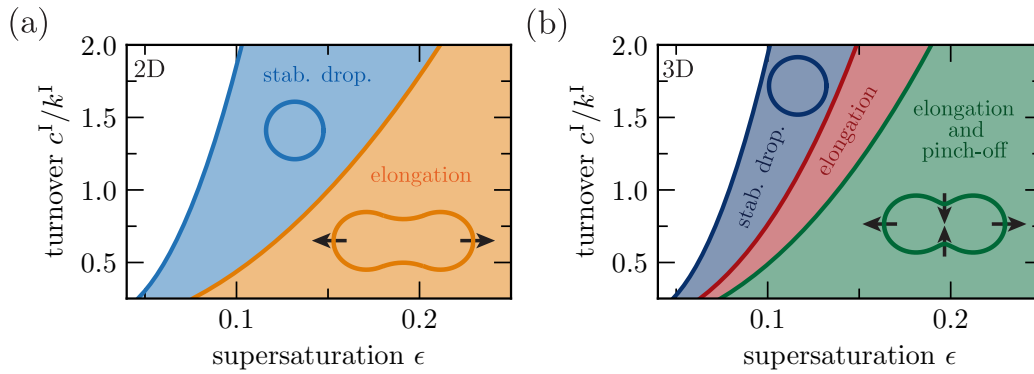


FIGURE 6.4: **Stability diagrams of chemically active droplets in 2D and 3D:** Given any turnover c^l , no chemically active droplets can exist for too low supersaturation values ϵ - white area in (a) (2D) or (b) (3D). When the supersaturation is increased, stable chemically active droplets can exist in both cases (blue area). A further increase of ϵ leads to an elongation instability of these droplets - orange area in (a) or red area in (b). Perturbations of the neck become unstable for even higher supersaturation values only in 3D systems - green area in (b). In 2D, no pinch-off instability can be found. For further parameter values, see App. C.

where the described cycle of growth and division can occur. Also, this line of pinch-off instability is presumably a lower bound in the area at which droplets can divide due to the more complex shape of a neck in an elongated droplet, thus leading to a bigger area of droplet division.

6.2 Pinch-off in 2D via curvature-dependent chemical reactions

As discussed above, bulk driven chemically active droplets can spontaneously elongate but do not divide in the introduced models in 2D. This section presents a mechanism that can lead to such divisions. For this, we allow additional chemical reactions at the interface of the droplets, depending on the mean curvature of the interface. When chemical reactions take place where the interface is bent outwards, the neck can be dissolved, leading to a division. To this end, we will first introduce a method of how the mean curvature of the droplet interface can be determined from the continuous field of volume fraction. Second, we will show how chemical reactions at the interface can be used to pinch off elongated droplets.

6.2.1 Determining the mean curvature of the droplet interface

In general, the mean curvature of a surface $G(x_1, x_2, \dots) = 0$ can be denoted as

$$H(x_1, x_2, \dots) = -\nabla \cdot \frac{\nabla G}{|\nabla G|}, \quad (6.18)$$

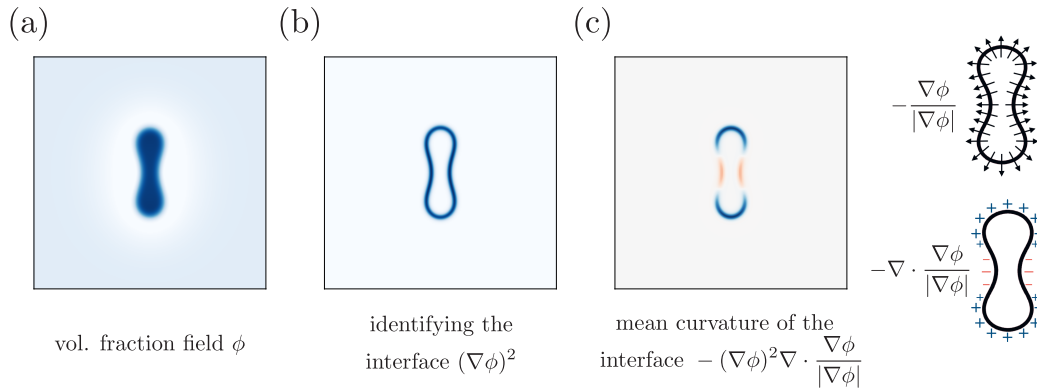


FIGURE 6.5: **Mean curvature of the droplet interface:** Given the volume fraction profile shown in (a), we identify the interface area where the term $(\nabla\phi)^2$ is large, see (b). The term $-(\nabla\phi)^2 \nabla \cdot \nabla\phi / (|\nabla\phi|)$ is positive where a sharp interface of a similar shape has positive mean curvature and negative vice versa, see the density plot in (c). Furthermore, we sketch the normalized gradient of ϕ and its divergence.

For details and the specific parameters, see App. C.

see [75]³. However, in our continuous system, we do not have a parameterization of the interface but a concentration field with strong gradient terms at the interface. Nevertheless, the divergence of the normalized gradient quantifies where the unit vectors parallel to the gradient diverge from each other or converge, see the sketch in FIG. 6.5(c). Due to the normalization, this quantity has finite values even for small gradients. Thus, the gradients caused by the chemical reaction will be measured by this term, too. To identify the interface, we multiply this term therefore by $(\nabla\phi)^2$. The latter quantity is substantial directly at the interface, where strong gradients occur. To measure the mean curvature of the droplet by having its continuous volume fraction profile, we use⁴

$$H' = -(\nabla\phi)^2 \nabla \cdot \frac{\nabla\phi}{|\nabla\phi|} . \quad (6.19)$$

The volume fraction profile ϕ in FIG. 6.5(a) occurs in the elongation dynamics of a slightly elongated droplet, identical to the example in FIG. 6.1. At this stage, two droplets can be identified, still connected via a neck. The mean curvature of a sharp interface would be positive at the two ends of the spherical droplets. However, in the neck area, the interface bends outwards. Thus the mean curvature of a sharp interface would be negative. To identify the interface area from continuous volume fraction field ϕ , we use $(\nabla\phi)^2$, see FIG. 6.5(b). The effective mean curvature, defined in Eq. 6.19, captures exactly the behavior of the mean curvature when a sharp interface is considered, see FIG. 6.5(c).

6.2.2 Chemical reactions at the interface

Again, we use Eq. 6.3 together with the reaction rate Eq. 6.4 for the dynamics of the volume fraction field in the bulk. The chemical reactions at the interface result in an

³Note, that in this reference, the mean curvature is defined with a factor 1/2. We follow the more classical definition in physics such that the mean curvature of a sphere in 3D is $2/R$.

⁴For numerical stability, we compute $\nabla\phi / (|\nabla\phi| + \epsilon)$, with $\epsilon = 0.0001$ in all the shown cases.

additional reaction sink or source term r_{int} . We use

$$\partial_t \phi = \gamma \nabla^2 \bar{\mu} + r + r_{\text{int}} \quad , \quad (6.20)$$

where

$$r_{\text{int}} = -c_{\text{int}} \text{sig} [H_{\text{tres}} - H'(\phi)] \quad , \quad (6.21)$$

with the degradation constant c_{int} . We choose $H_{\text{tres}} < 0$. Thus, the sigmoidal function⁵ $\text{sig} [H_{\text{tres}} - H'(\phi)]$ has non-vanishing contributions only in areas where H' is comparable to H_{tres} , or smaller. Outside the interface area, H' vanishes due to its dependency on $(\nabla \phi)^2$. Thus, $r_{\text{int}} = 0$ and no additional chemical reactions place in the bulk when $H_{\text{tres}} < 0$. At the interface, H' has large negative values at positions where the interface is bent inwards. Therefore, the neck between two droplets after elongation becomes destabilized due to the chemical reactions. However, the remaining dynamics, like the elongation of droplets or the stationarity of spherical droplets, are not affected by these additional chemical reactions modeled by r_{int} .

In FIG. 6.5, we show the dynamics for three different parameter settings of the degradation constant c_{int} . We start with one slightly elongated droplet in all three settings. In the beginning, the mean curvature of the droplet interface is positive everywhere. Thus, the initial dynamics are identical. However, when the droplet has elongated, a neck is formed with negative mean curvature. The degradation constant c_{int} now controls how much material is lost at these positions.

We choose $c_{\text{int}}/(k^I \phi^I) = 0.1$, for FIG. 6.5(a). For this setting, the degradation at the interface is too weak to lead to a division. Long bands are formed similar to cases without any additional chemical reactions at the interface. Only after $t \approx 600$, a single division takes place, and the structure separates once for this parameter setting. In FIG. 6.5(b), we show the dynamics of a system with $c_{\text{int}}/(k^I \phi^I) = 0.3$. Here, the degradation at the interface is strong enough to pinch off formed necks. However, the degradation is not strong enough to pinch off all necks robustly. Thus, in the dynamics, some stripes are formed. Once these interfaces are straight, the mean curvature is zero, and no degradation occurs. When the degradation constant is $c_{\text{int}}/(k^I \phi^I) > 0.5$, we show the case of $c_{\text{int}}/(k^I \phi^I) = 0.8$ in FIG. 6.5(c), every formed neck becomes unstable and chemically active droplets divide robustly in 2D. Only for too large degradation rates $c_{\text{int}}/(k^I \phi^I) \approx 50$, the reaction at the interface is so large during the pinch off, that some droplets dissolve during the pinch off (not shown). Thus, for degradation constants in the range $0.5 < c_{\text{int}}/(k^I \phi^I) < 50$, our proposed mechanism leads to a robust droplet division in 2D, and cycles of droplet growth and droplet division can occur.

⁵We choose $\text{sig}(x) = 1/(1 + \exp(-x))$.

6.3 Discussion

In this chapter, we used the model from Zwicker et al. [20] of a phase-separating binary mixture with chemical reactions. In 3D, chemically active droplets can divide under these dynamics. At the beginning of this chapter, we showed why division does not occur in two-dimensional systems. The chemically active droplets still elongate, but no pinch-off occurs. This is because, in two-dimensional systems, the interface of a formed neck between the two sides of an elongated droplet becomes flat in the center. Thus, this interface has a vanishing mean curvature and, therefore, no Laplace pressure exists. However, a cylinder forms the neck between the two sides of an elongated droplet in three-dimensional systems. Still, the principal curvature along the elongation vanishes. However, the principal curvature orthogonal to this direction has a finite value, resulting in a Laplace pressure. This behavior is similar to the Plateau-Rayleigh instability, which describes the break up of a fluid jet when the jet radius becomes too small. In 2D, fluid jets also do not break up independent of the jet radius due to the same absence of Laplace pressure in 2D [74].

In the second part of this chapter, we introduced a model with additional chemical reactions at the interface. Dependent on the mean curvature of the interface, the droplet forming material also degrades. These chemical reactions destabilize the neck area after an active chemical droplet has elongated. For this mechanism, we showed how the mean curvature of the droplet interface can be defined by just knowing the continuous volume fraction field. The numerical complexity of these additional terms is more costly than the initial dynamics. However, it is still much more efficient than solving a qualitatively similar system in 3D. Therefore, we can solve the dynamics of systems large enough to accommodate several hundreds of droplets.

More complex models can be simulated with this numerical advantage, where different chemically active droplets interact. With this, simple models of 'ecosystems' of chemically active droplets, with, for example, predator-prey dynamics of different droplet types, will be investigated in the future.

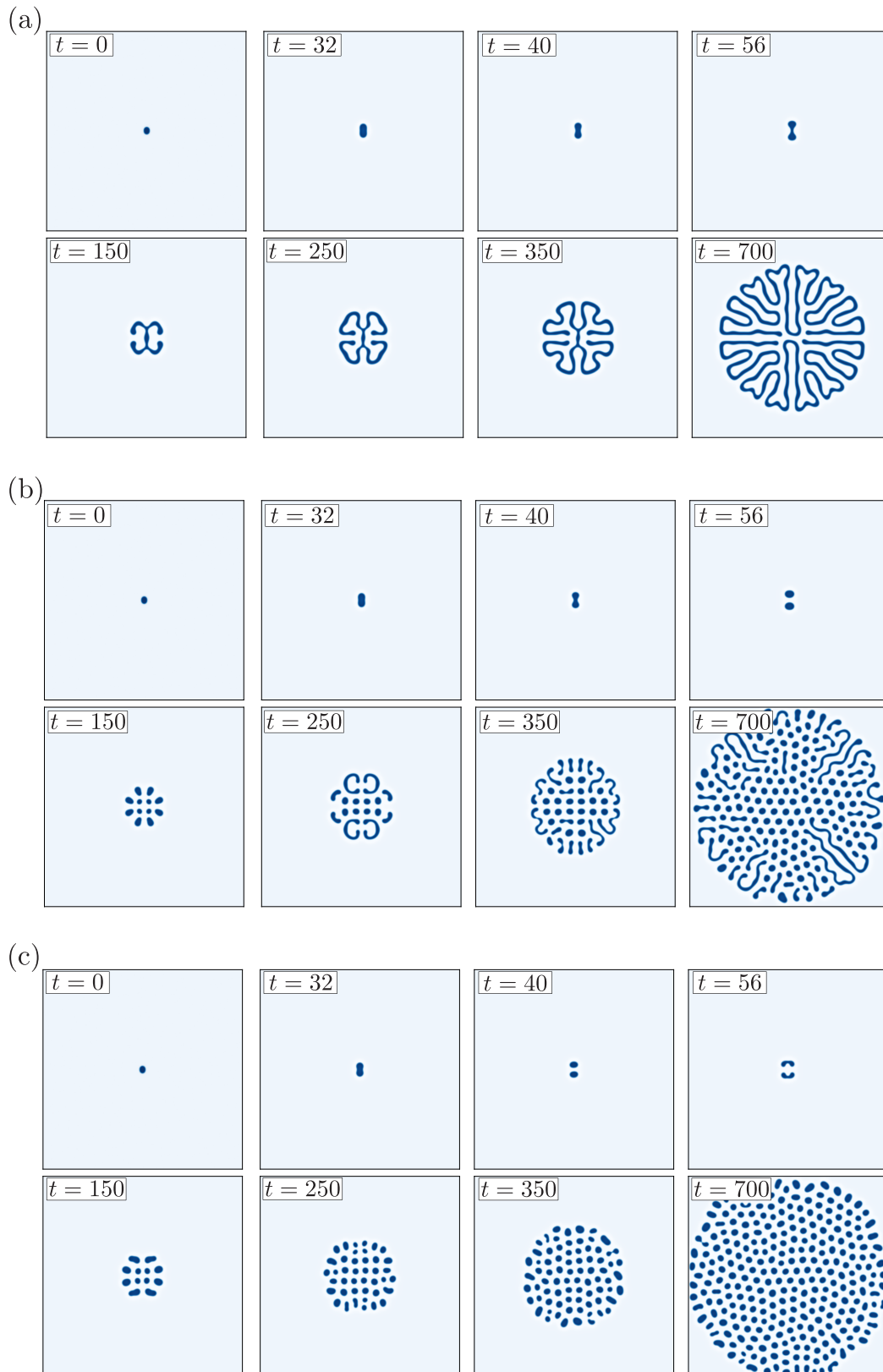


FIGURE 6.6: **Pinch-off in 2D systems via reactions at the interface:** Snapshots of volume fraction fields in the dynamics of three systems with different degradation constants c_{int} at the interface and identical initial conditions. In (a), $c_{\text{int}}/(k^I \phi^I) = 0.1$ and almost no division occurs. In (b), $c_{\text{int}}/(k^I \phi^I) = 0.3$ and pinch-off occurs. For some cases, however, still stripes are formed. In (c), $c_{\text{int}}/(k^I \phi^I) = 0.8$ and droplet division occurs robustly. For details and further parameter settings, see App. C.

Chapter 7

Conclusion and Outlook

In this thesis, we studied the consequences of the spatial organization of chemical reactions via phase separation. Therefore, we generalized the mass-action kinetics for systems of homogeneous compartments at phase equilibrium. We derived dynamical equations in spatially continuous, multi-component systems that can lead to the thermodynamic equilibrium, defined by the simultaneous equilibrium of phases and chemical reactions. Furthermore, we discussed two ways of maintaining these systems out of equilibrium: driving chemical reactions differently in phases or coupling the system to reservoirs over its boundaries. The droplet dynamics found in both scenarios is absent in equilibrium systems. We introduced an effective description of such multi-component chemically active droplets for a quantitative study of this dynamics. Next, we used this description to study the energy and matter supply in a protocell model of a chemically active droplet. Finally, we showed that chemically active droplets with driven reactions do not divide spontaneously in 2D. However, we introduced a simple model with mean-curvature-dependent chemical reactions at the droplet interface, which can lead to a robust droplet division in 2D. In the following, we highlight the main results of each chapter and point to possible future work.

In Chapter 2, we introduced dynamical equations for the densities of components and phase volumes in compartmentalized systems with chemical reactions. These compartments are formed in phase-separating systems with fast diffusion where we can consider homogeneous phases at phase equilibrium. In this framework, diffusion gets reduced to an exchange between compartments that can grow and shrink. Thus, ordinary differential equations are sufficient for describing systems with diffusion and chemical reaction. Especially for small experimental systems where chemical reactions are not diffusion limited, this framework can provide a simple description. Hopefully, the theoretical predictions of these dynamics will be tested in experimental systems such as coacervates with enzymatic reactions [76, 77, 78, 79]. However, these equations reveal also why a pure enrichment of components inside compartments does not necessarily lead to an increased reaction rate, as expected

from mass-action laws in dilute systems. In other words, the increased local concentration of a reactive component due to phase separation does not necessarily increase the rates of reactions in which it participates. The reaction rate coefficients solely determine the speed-up or slow-down of reactions in each compartment, which can also decrease upon condensation. These insights might be relevant for explaining recent observations in coacervate emulsions with enzymatic reactions [80, 81, 82, 83]. Furthermore, we show how non-equilibrium steady states can exist in these systems when chemical reactions are driven differently between compartments. To depict these non-equilibrium states in the phase diagram, we introduce the tie line selecting curve, which translates between conserved quantities in the system and the chosen phase equilibrium. Future work can be done by performing the dilute limit for all reacting components, while the compartments are formed by the phase separation of two non-dilute components. This would further reduce the complexity and corresponds to a setting often found in experiments.

Chapter 3 discusses spatially continuous systems. Here, non-linear fourth-order partial differential equations govern the dynamics in phase-separating systems with chemical reactions. These dynamics were derived by minimizing the free energy. Thus, we can study the relaxation kinetics toward the simultaneous equilibrium of phases and chemical reactions. We compare these relaxation kinetics to the temporal evolution in homogeneous compartments and explore their differences in systems with fast chemical reactions and spatial inhomogeneities.

Furthermore, we study active systems with driven chemical reactions by explicitly breaking detailed balance of the rates. We show that droplets initialized in the nucleation-and-growth regime can undergo shape instabilities and deform while growing. Whereas in systems with many droplets, ripening can be suppressed. Both processes were previously described in binary mixtures without conserved densities [19, 20]. We explore how in multi-component mixtures, the dynamics of conserved densities can differ from equilibrium situations, although detailed balance is only broken within the dynamics of the reaction extents. Additionally, we introduce active systems that are maintained away from equilibrium via concentration boundary conditions. Here, detailed balance is satisfied everywhere within the system and only broken at the system boundaries. In contrast to equilibrium settings, droplets of stationary size can exist in open systems and can even elongate and divide for strong enough driving.

To quantitatively study chemically active droplets in multi-component mixtures, we introduce an effective description of droplets in a sharp interface limit in Chapter 4. Here, linear reaction-diffusion equations are coupled via a moving interface. Only here do non-linear equations have to be solved to determine the boundary values at the interface. We assume the local equilibrium of phase separation. However, this does not fix these boundary conditions fully in multi-component mixtures. The continuity of fluxes selects the remaining constraints. In closed systems, also global

conservation laws have to be taken into account. With this, we revisit systems previously studied only numerically in Chapter 3, and perform a linear stability analysis to understand the shape instabilities. The here developed method is a generalization of the effective description of chemically active droplets introduced by Zwicker et al. [20] for multi-component mixtures, where multiple phase equilibria exist, and conservation laws have to be taken into account. Possible future work includes solving these moving boundary problems numerically under non-linearized dynamics and considering dynamical solutions of the volume fraction profiles outside the quasi-static limit.

Chemically active droplets have been proposed as models for protocells [20], which are prebiotic, cell-like objects that could have emerged at the origin of life [64, 63, 67, 84], and first experimental systems have been designed [85]. Following these ideas, we introduce models of chemically active droplets, kept away from equilibrium by the supply of nutrients and the removal of waste, in Chapter 5. With this, we obtain protocell models where we can understand the chemical reactions inside the droplets as a simple form of their metabolism. For these models, we discuss two cases of breaking detailed balance. First, in a boundary-driven case, droplets are coupled to external reservoirs at the system boundary, supplying nutrient and removing waste. Second, in the bulk-driven case, detailed balance of an additional chemical reaction outside the droplets is broken, effectively regenerating waste into nutrient. For both scenarios, we study the dynamics and find similar non-equilibrium droplet dynamics in the form of shrinkage, non-equilibrium steady states, elongation, and division, as previously discussed in Chapter 3 and Chapter 4. Thus, these protocell models show similar behavior to living cells. They dissolve with too little nutrient supply, can exist at a steady state, or even grow and divide when the nutrient supply is increased.

Furthermore, we can study the simple form metabolism of these objects. Studying metabolism is necessarily related to the study of fluxes of energy and matter. Therefore, we discuss the energetics of chemically active droplets. We show that the growth or shrinkage of a chemically active droplet is governed by fluxes of the conserved quantities at the droplet surface and that the maintenance of non-equilibrium steady states is enabled by fluxes of the non-conserved reaction extents. In biology, metabolic processes are classified as anabolic or catabolic. Similarly, to conserved and non-conserved densities, anabolism and catabolism can be related to growth and maintenance, respectively. Additionally, we can study the balance of energy and the related heat release. We show that protocells can be classified into four different cases. Protocells can be based on endothermic or exothermic reactions and release or absorb latent heat at the droplet interface. The latter shows that a measurement of overall heat absorption by an organism does not necessarily imply endothermic biochemistry. This is related to the measurements in bacteria [70, 71]. Possible future work can be done by modeling biological metabolic processes within droplets. The results of these models could be compared to recent experimental studies of the

energetics in living objects [69]. Comparing the theoretical work with experimental results could shine further light on the energetic costs and constraints of specific cellular processes [86].

In the previous chapters, we have shown examples of chemically active droplets undergoing shape instabilities, leading to droplet elongation and potentially division. However, in closed two-dimensional systems with driven chemical reactions, chemically active droplets can elongate but do not spontaneously divide. In Chapter 6, we perform the linear stability analysis of a minimal binary model. We show the similarities of the elongation instabilities but the differences in the pinch-off instabilities between 2D and 3D systems. This linear stability analysis reveals that the absence of Laplace pressure of a formed neck in 2D leads to the stable neck form. This difference between dimensions is similar to the Plateau-Rayleigh instability, which describes the break up of a fluid jet for small neck radii in 3D but does not exist in 2D [74].

In the second part of the chapter, we show how chemical reactions that are localized at the interface can lead to stable droplet division in 2D when these reactions have reaction rates proportional to the mean curvature of the interface. We numerically solve the corresponding equations and show that in the absence of conservation laws in a binary mixture, cycles of droplet growth and division can lead to hundreds of droplets in a closed box. The primary motivation of this chapter was to obtain a minimal model of dividing chemically active droplets in 2D. While division occurs naturally in 3D, the numerical cost of solving the underlying fourth-order partial differential equations limits the system size and, thus, the total number of droplets. We hope that this 2D system opens the door for future work on droplet systems with several different droplet species competing and cooperating in a simple form of an ecosystem and allowing models for evolution. Furthermore, we introduced a model with chemical reactions at the droplet interface. However, the primary shape instability of droplet elongation is still caused by chemical reactions in the bulk. However, similar terms of mean curvature-dependent chemical reactions at the droplet interface could potentially lead to shape instabilities themselves, similar to the growth of interfaces modeled mainly by the KPZ-equation [87]. Therefore, analyzing the consequences of chemical reactions at the droplet interface on the shape stability of droplets is a further possible research direction.

Appendix A

Free energy considerations

Flory-Huggins free energy density

The exchange chemical potentials given in Eq. 1.2 are derived from the free energy

$$F = \int d^3x \left[f(\phi) + \sum_{i=1}^M \frac{\kappa_i}{2\nu_i} (\nabla\phi_i)^2 \right] , \quad (\text{A.1})$$

with the Flory-Huggins type of free energy density

$$f = \sum_{i=0}^M \frac{k_B T}{\nu_i} \phi_i \log(\phi_i) + \sum_{\langle i,j \rangle} \chi_{ij} \phi_i \phi_j + \sum_{i=0}^M \omega_i^0 \phi_i , \quad (\text{A.2})$$

where $\phi_0 = 1 - \sum_{i=1}^M \phi_i$, and the sum over the pairs $\langle i, j \rangle$ include all possible combinations of different i and j , including the solvent. For simplicity, we have neglected contribution related to gradient in solvent volume fraction. Moreover, χ_{ij} is a matrix describing the molecular interactions with $\chi_{ii} = 0$ and ω_i^0 are the internal free energies. After replacing the solvent volume fraction and using the definition $\bar{\mu}_i = \nu_i \delta F / \delta \phi_i$, we obtain

$$\begin{aligned} \bar{\mu}_i &= k_B T \log \left(\phi_i \phi_0^{-\nu_i/\nu_0} \right) + 1 - \frac{\nu_i}{\nu_0} - \kappa_i \nabla^2 \phi_i \\ &+ \nu_i \sum_{j=1}^M (\chi_{ij} - \chi_{i0} - \chi_{j0}) \phi_j + \nu_i \chi_{i0} + \nu_i \omega_i^0 - \nu_i \omega_0^0 . \end{aligned} \quad (\text{A.3})$$

We can now identify the composition independent reference chemical potential

$$\omega_i = 1 - \frac{\nu_i}{\nu_0} + \nu_i \chi_{i0} + \nu_i \omega_i^0 - \nu_i \omega_0^0 , \quad (\text{A.4})$$

in Eq. 1.2 and the exchange activity coefficient as stated in Eq. 1.3.

Appendix B

Surface tension in multi-component mixtures

A interface between two phases comes with a cost in free energy. It is proportional the dimension of the interface (area in 3D, line in 2D, point in 1D) and the so called surface tension γ . Formally, γ is defined in the limit of infinite systems, therefore flat surfaces and 1D systems effectively. For the separation of two phases we minimize

$$F(\phi) = \int_{-\infty}^{\infty} dx \left(f(\phi) + \sum_i \frac{\kappa_i}{2} (\partial_x \phi_i)^2 \right) , \quad (\text{B.1})$$

where $f(\phi)$ is the free energy density dependent on the whole set of volume fractions ϕ_i , $i = 1, \dots, N$. Thats consider an interface at position $x = 0$. Far away from the interface, the bulk concentrations $\phi_i(\pm\infty) = \phi_i^{\text{I/II}}$ obey

$$f^{\text{I}} - f^{\text{II}} = \mu_i^{\text{I/II}} (\phi_i^{\text{I}} - \phi_i^{\text{II}}) , \quad (\text{B.2})$$

$$\mu_i^{\text{I}} = \mu_i^{\text{II}} , \quad (\text{B.3})$$

with $\mu_i^{\text{I/II}} = \partial f^{\text{I/II}} / \partial \phi_i$. However, these equations are invariant under changes up to linear contributions in $f(\phi)$. Following the lines of de Gennes, we can therefore define a linearly adjusted potential

$$W(\phi) = f(\phi) - f^{\text{I}} - \mu_i^{\text{I/II}} (\phi_i - \phi_i^{\text{I}}) , \quad (\text{B.4})$$

which is still minimal at equilibrium. Furthermore, W vanishes in the bulk. With this, we can compute the cost of the interface

$$\gamma = \int_{-\infty}^{\infty} dx \left(W(\phi) + \sum_i \frac{\kappa_i}{2} (\partial_x \phi_i)^2 \right) , \quad (\text{B.5})$$

which equals to the surface tension in 1D. Clearly, γ depends on the κ_i 's and the $\phi_i^{\text{I/II}}$'s and can be numerically computed by solving the spacial problem and integrating over x . However, this is costly and not always necessary. From the minimum

of F , we find

$$\kappa_i \partial_x^2 \phi_i = \frac{\partial W}{\partial \phi_i} . \quad (\text{B.6})$$

Multiplying Eq. B.6 with $\partial_x \phi_i$, summing over i and integrating, we find

$$\frac{\kappa_i}{2} (\partial_x \phi_i)^2 = W(\phi) . \quad (\text{B.7})$$

Here, no integration constant appears because both sides vanishes for $x \rightarrow \pm\infty$. The surface tension can therefore be written as an integral along the path \mathcal{C} from one phase to the other

$$\gamma = \int_{\mathcal{C}} d\phi_i \kappa_i \partial_x \phi_i . \quad (\text{B.8})$$

The path \mathcal{C} is defined by Eq. B.6¹. We can solve this integral for the case that all but one $\kappa_i = 0$. Eq. B.6 for all these other components are defining then (algebraic) equations how these $N - 1$ components vary along the path. Lets assume $\kappa_1 \neq 0$, and $\kappa_i = 0$, for $2 \leq i \leq N$. From Eq. B.7 we can follow $\partial \phi_1 / \partial x = \sqrt{2W/\kappa_1}$. Therefore Eq. B.8 reduces to

$$\gamma = \int_{\phi_1^I}^{\phi_1^{II}} d\phi_1 \sqrt{2\kappa_1 W(\phi_1, \phi_i(\phi_1))} . \quad (\text{B.9})$$

Example of two-phase coexistence in a ternary mixture

Consider a system with a droplet forming component B and an additional component A dispersed in a solvent S . As usually, we use a Flory-Huggins type-off free energy density. For a two-phase coexistence, we assume χ_{BS} has to be high enough, such that the B phase separates from the solvent S . Consider a system with a droplet forming component B and an additional component A dispersed in a solvent S . As usual, we use a Flory-Huggins type-off free energy density. For a two-phase coexistence, we assume χ_{BS} has to be high enough such that the B phase separates from the solvent S . Component A only partitions unequally into the two phases. We show an exemplary phase diagram in FIG. B.1(d).

In FIG. B.1(a), we show the spatial profile of this system in a one-dimensional system, zoomed at the interface area, for average volume fractions corresponding to the red tie line in FIG. B.1(d). While component B runs monotonically from ϕ_B^I towards ϕ_B^{II} , A is locally enriched at the interface. This enrichment becomes obvious when ϕ_A is plotted against ϕ_B , see FIG. B.1(b). Here, the blue line is the solution of the algebraic Eq. B.6, for $\kappa_A = 0$, given a ϕ_B value between ϕ_B^I and ϕ_B^{II} . The red dots correspond to the grid points on which the numerical solution shown FIG. B.1(a) was computed. Having the functional form of ϕ_A in respect of ϕ_B allows expressing the local energy cost $\sqrt{2W}$, thus, the integrand in Eq. B.9, as a function of ϕ_B , shown in FIG. B.1(c).

¹For all κ being identical, the problem can be understood as the motion of a particle in a potential. The mass of the particle is given by κ . Eq. B.6 connects the acceleration to the derivative of a potential $-W$. Eq. B.7 states the conservation of energy. The kinetic energy $\kappa/2(\partial_x \phi)^2$ equals the potential energy $-W$, where its usually undefined offset is fixed to 0.

Integrating over this quantity leads to the surface tension γ . We show the surface tension as a function of the equilibrium volume fraction ϕ_A^{II} (along the left branch of the binodal line from 0 to the critical point) in FIG. B.1(e,f). The surface tension is the highest for the binary mixture of component B and the solvent and decays almost exponentially to zero the closer the mixture comes to the critical point. Furthermore, we compare it with numerical results obtained by solving the spatial profiles and using Eq. B.5. This comparison reveals that the numerical and analytical results agree well even for non-vanishing κ_A contributions. However, a detailed analysis of which interactions this is valid is still to come.

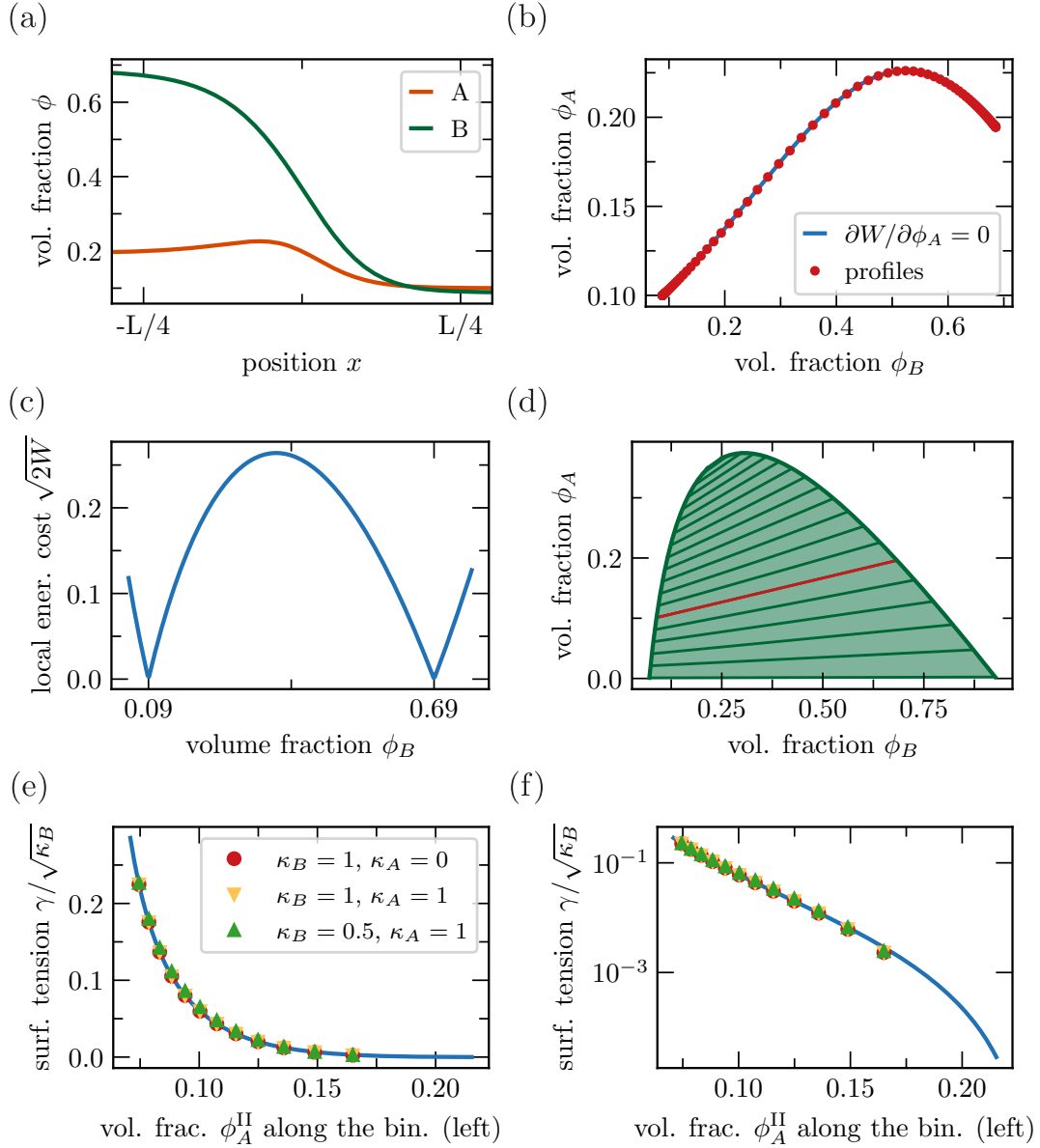


FIGURE B.1: **Surface tension in multi-component mixtures:** We show the spatial profiles of the volume fractions ϕ_A and ϕ_B of a ternary mixture in a 1D system in (a). We highlight the equilibrium with the red tie line in the phase diagram of this system, shown in (d). In (b), we plot these volume fractions against each other and compare it with the solution of Eq. B.6. The integrand of Eq. B.9 as a function of ϕ_B is shown in (c). Integrating over it leads to the surface tension shown in (e,f) as a function of ϕ_A^{II} (linear and logarithmic), thus, running along the left branch of the binodal line from the binary mixture of B with S towards the critical point.

Appendix C

Figure details

All numerical solutions were obtained by a spectral implicit-explicit of Runge-Kutta algorithm of third order, see [88].

FIGURE 1.1: "Common tangent" construction for a binary (M=1) mixture:

Binary mixture with free energy density following Eq. A.2, $i = S, A$ and parameters $\chi_{AS} = 2.3$, $\omega_A^0 = 0.03$, $\omega_S^0 = 0$, $\nu_A/\nu_S = 1$, $k_B T = 1$, $2\gamma/R = 0.016$ (for the orange dots).

FIGURE 1.2: Nucleation-and-growth regime vs. spinodal decomposition:

Binary mixture with free energy density following Eq. A.2, $i = S, A$ and parameters $\chi_{AS} = 2.3$, $\omega_A^0 = 0.03$, $\omega_S^0 = 0$, $\nu_A/\nu_S = 1$, $k_B T = 1$, $\kappa_A = 1$, $\kappa_S = 0$, $\Gamma = 1$, and average composition as indicated. (b): 2D system (grid points $N = 128$, system size $L = 140$) with no-flux boundary conditions. Initialization: homogeneous with small fluctuations. In the upper row spherical perturbation of $R = 4$ was added to nucleate.

FIGURE 1.3: Partial and thermodynamic equilibrium in a ternary mixtures:

Ternary mixture with free energy density following Eq. A.2, $i = S, A, B$ and parameters $\chi_{AS} = -1$, $\chi_{BS} = 3$, $\chi_{AB} = 0$, $\omega_A^0 = 2$, $\omega_B^0 = 0$, $\omega_S^0 = 0$, $\nu_i/\nu_S = 1$, $k_B T = 1$. For (d), we vary ω_B^0 according to the inset.

FIGURE 1.4: Thermodynamic equilibrium for quaternary mixtures:

Quaternary mixture with free energy density following Eq. A.2, $i = S, A, B, C$ and parameters $\chi_{AS} = 1.25$, $\chi_{BS} = 0$, $\chi_{CS} = 3.2$, $\chi_{AB} = 0$, $\chi_{AC} = -1.25$, $\chi_{BC} = 0$, $\omega_A^0 = 3$, $\omega_B^0 = 3$, $\omega_C^0 = 0$, $\omega_S^0 = 0$, $\nu_i/\nu_S = 1$, $k_B T = 1$.

FIGURE 2.1: Unimolecular reaction kinetics:

Same parameters as in FIG. 1.3 were chosen. For (a,b), we use the rates $k^{I/II} = 1$. For (c,d), we adjust k^{II} according to the inset.

FIGURE 2.2: Average reaction flux and acceleration:

Same parameters as in FIG. 2.1 were chosen.

FIGURE 2.4: Tie line selecting curve:

Ternary mixture with free energy density following Eq. A.2, $i = S, A, B$ and parameters $\chi_{AS} = 1.85$, $\chi_{BS} = 2.8$, $\chi_{AB} = -0.5$, $\omega_S^0 = 0$, $\nu_i/\nu_S = 1$, $k_B T = 1$, $k^{I/II} = 1$. The reference chemical potentials of A, B are composition dependent with $\omega_i^0 = \omega_i^1 + \omega_i^2 \text{sig}[(\phi_A + \phi_B - \psi_{\text{crit}})/0.1]$ with $\text{sig}(x) = (1 + \tanh(x))/2$. We have chosen for (a,b) $\omega_A^1 = 2$, $\omega_A^2 = -2$, $\omega_B^1 = 0$, $\omega_B^2 = 1.2$. In (c), we keep ω_i^1 identical to (a,b) but vary: $\omega_i^2 = 0$ (first plot); $\omega_A^2 = -0.66$, $\omega_B^2 = 0.4$ (second plot); $\omega_A^2 = -1.33$, $\omega_B^2 = 0.8$ (third plot); $\omega_A^2 = -2$, $\omega_B^2 = 1.2$ (fourth plot).

FIGURE 3.1: Relaxation dynamics with instantaneous phases equilibrium vs. spatial systems with fast diffusion:

Same parameters as in FIG. 2.1 were chosen. Numerical solutions of the 2D periodic systems (grid points $N = 128$, system size $L = 100$), with $\kappa_i = 1$, $\Gamma = 1$. The binning of two-dimensional composition space was done with $\delta\phi_B = 0.0087$, $\delta\phi_A = 0.0039$.

FIGURE 3.2: Relaxation dynamics - slow and intermediate diffusion:

Same parameters as in FIG. 2.1 were chosen. The numerical solutions were obtained with an implicit-explicit of Runge-Kutta algorithm of third order, in a 1D system (grid points $N = 256$, system size $L = 100$) with no-flux boundary conditions. We used $\kappa_i = 2$, $\Gamma = 1$. The time-scale is given in terms of $k^I = 1$ for $\lambda_{\text{RD}} = 0.6$, thus $k^I = 100$ for $\lambda_{\text{RD}} = 0.06$.

FIGURE 3.3: Phase-specific driving and fast diffusion:

Same parameters as in FIG. 2.4 were chosen. Numerical solutions of a 2D system (grid points $N = 128$, system size $L = 100$) with periodic boundary conditions, with $\kappa_i = 1$, $\Gamma = 1$. The time-scale is given in terms of a constant rate $k = 1 \cdot 10^{-5}$.

FIGURE 3.4: Non-equilibrium steady states for different kinetic coefficients:

Same parameters as in FIG. 2.4 were chosen. Numerical solutions in a 1D system (grid points $N = 256$, system size $L = 100$) with no-flux boundary conditions, with $\kappa_i = 2$, $\Gamma = 1$. Constant rates k were chosen according to the reaction-diffusion length scales.

FIGURE 3.5: Ripening of chemically active droplets:

Ternary mixture with free energy density following Eq. A.2, $i = S, A, B$ and parameters $\chi_{AS} = 2.5$, $\chi_{BS} = 2.5$, $\chi_{AB} = 0$, $\omega_S^0 = 0$, $\nu_i/\nu_S = 1$, $k_B T = 1$, $\omega_A = 2.4$. The reference chemical potential of B is composition dependent with $\omega_B^0 = 1.2 + 2.4 \text{sig}[(\phi_A + \phi_B - 0.5)/0.1]$ with $\text{sig}(x) = (1 + \tanh(x))/2$. (b): Numerical solutions of 2D system (grid points $N = 256$, system size $L = 200$) with periodic boundary conditions, with $\kappa_i = 2$, $\Gamma = 1$. The time-scale is given in terms of a constant rate $k = 5 \cdot 10^{-3}$. Init.: $\phi_i = 0.4$ (c-d): Numerical solutions of 1D system (grid points $N = 512$, system size $L = 90$) with no-flux boundary conditions, with $\kappa_i = 0.5$, $\Gamma = 1$, $k = 5 \cdot 10^{-3}$.

FIGURE 3.6: Decoupled conserved and non-conserved variables:

Ternary mixture with free energy density following Eq. A.2, $i = S, A, B$ and parameters $\chi_{AS} = 0, \chi_{BS} = 0, \chi_{AB} = 3, \omega_S^0 = 0, \nu_i/\nu_S = 1, k_B T = 1, \omega_A = 0$. The reference chemical potential of B is composition dependent with $\omega_B^0 = 0.5 - 1.2\phi_A^2 \text{sig}[(\phi_A + \phi_B - 0.5)/0.4]$ with $\text{sig}(x) = (1 + \tanh(x))/2$. (b): Numerical solutions of 2D system (grid points $N = 128$, system size $L = 100$) with periodic boundary conditions, with $\kappa_i = 2, \Gamma = 1$. The time-scale is given in terms of a constant rate $k = 4 \cdot 10^{-4}$. Init.: $\phi_A = 0.8, \phi_B = 0.1$ with a pert. at the center (nuc. regime), $\phi_i = 0.45$ (spin. regime) (c-d): Numerical solutions of 2D system (grid points $N = 512$, system size $L = 90$) with no-flux boundary conditions, with $\kappa_i = 0.5, \Gamma = 1, k = 3.5 \cdot 10^{-4}$.

FIGURE 3.7: Coupled conserved and non-conserved variables:

Ternary mixture with free energy density following Eq. A.2, $i = S, A, B$ and parameters $\chi_{AS} = 2.1, \chi_{BS} = 2.8, \chi_{AB} = 0, \omega_S^0 = 0, \nu_i/\nu_S = 1, k_B T = 1, \omega_A = 2.4$. The reference chemical potential of B is composition dependent with $\omega_B^0 = 1.2 + 2.4\text{sig}[(\phi_A + \phi_B - 0.5)/0.1]$ with $\text{sig}(x) = (1 + \tanh(x))/2$. (b): Numerical solutions of 1D system (grid points $N = 512$, system size $L = 90$) with no-flux boundary conditions, with $\kappa_i = 0.5, \Gamma = 1$. The time-scale is given in terms of a constant rate $k = 5 \cdot 10^{-3}$.

FIGURE 3.8: Dynamics of coupled conserved and non-conserved variables:

Same parameters as in FIG. 3.7 were chosen. Numerical solutions of 2D system (grid points $N = 256$, system size $L = 200$) with no-flux boundary conditions, with $\kappa_i = 1, \Gamma = 1$. The time-scale is given in terms of a constant rate $k = 5 \cdot 10^{-3}$. Init.: (b) $\phi_A = 0.1, \phi_B = 0.16$ with a pert. at the center; (b) $\phi_A = 0.02, \phi_B = 0.24$; (c) $\phi_A = 0.00001, \phi_B = 0.26$. The time-scale is given in terms of a constant rate $k = 5 \cdot 10^{-3}$. Furthermore, the chem. reaction was not allowed in the early dynamics in (b,c).

FIGURE 3.10: Droplet growth and shrinkage in open systems without reactions:

Ternary mixture with free energy density following Eq. A.2, $i = S, A, B$ and parameters $\chi_{AS} = 0, \chi_{BS} = 2.8, \chi_{AB} = -1, \omega_S^0 = 0, \nu_i/\nu_S = 1, k_B T = 1, \omega_A = 2, \omega_B = 0$. Numerical solutions of 1D system (grid points $N = 512$, system size $L = 90$) with concentration boundary conditions (indicated in (a)), with $\Gamma = 1, \kappa = 1.5$.

FIGURE 3.11: Stationary chemically boundary driven droplet in 1D:

Same parameters as in FIG. 3.10 where chosen, with additional reaction with rate $k(\phi_B) = 2 \cdot 10^{-5} \text{sig}[(\phi_B - 0.33)/0.1]$ with $\text{sig}(x) = (1 + \tanh(x))/2, \Gamma = 3, \kappa = 1.5$.

FIGURE 3.12: Stationary chemically boundary driven droplet in 2D:

Ternary mixture with free energy density following Eq. A.2, $i = S, A, B$ and parameters $\chi_{AS} = 0, \chi_{BS} = 2.8, \chi_{AB} = 1, \omega_S^0 = 0, \nu_i/\nu_S = 1, k_B T = 1, \omega_A = 3, \omega_B = 2$. Numerical solutions of 1D system (grid points $N = 128$,

system size $L = 150$) with concentration boundary conditions (indicated in (a)), with $\Gamma = 1$, $\kappa = 1.5$. Reaction rate $k(\phi_B) = 2 \cdot 10^{-4} \text{sig}[(\phi_B - 0.33)/0.1]$ with $\text{sig}(x) = (1 + \tanh(x))/2$, $\Gamma = 3$, $\kappa = 1.5$. Init.: (b) droplet with $R = 12$ at the center; (c) slightly elongated droplet with $R = 12$.

FIGURE 4.1: Comparison of continuous profiles and the effective description for different kinetic coefficients:

Same parameters as in FIG. 3.4 were chosen.

FIGURE 4.2: Growth and shrinkage of a droplet in an open system without chemical reactions:

Same parameters as in FIG. 3.10 were chosen.

FIGURE 4.3: Stationary chemically active droplets in a boundary driven system:

Same parameters as in FIG. 3.12 were chosen.

FIGURE 4.4: Stationary chemically active droplets for different phase diagrams:

For (a,c,e), the same parameters as in FIG. 3.10 were chosen, except the reference chemical potentials $\omega_A = 3.7$, $\omega_B = 2$. In (b,d,f), ternary mixture with free energy density following Eq. A.2, $i = S, A, B$ and parameters $\chi_{AS} = 2.1$, $\chi_{BS} = 2.8$, $\chi_{AB} = -1$, $\omega_S^0 = 0$, $\nu_i/\nu_S = 1$, $k_B T = 1$, $\omega_A = 2$, $\omega_B = 2$.

FIGURE 4.5: Shape stability of chemically active droplets:

Same parameters as in FIG. 3.10 were chosen.

FIGURE 5.3: Numerical study of a boundary driven chemically active droplet:

Quaternary mixture with free energy density following Eq. A.2, $i = S, D, N, W$ and parameters $\chi_{DS} = 3$, $\chi_{NS} = 1$, $\chi_{WS} = 0$, $\chi_{DN} = 0$, $\chi_{DW} = 1$, $\chi_{NW} = 0$, $\omega_S^0 = 0$, $\omega_D^0 = 10$, $\omega_N^0 = 20$, $\omega_W^0 = 0$, $\nu_i/\nu_S = 1$, $k_B T = 1$, $\kappa_D = 1$. Composition-dependency of the reactions via $k_\alpha = K_\alpha \text{sig}[(\phi_D - 0.33)/0.01]$ with $\text{sig}(x) = (1 + \tanh(x))/2$, $K_1/\exp(-\omega_N^0) = 0.025$, $K_2/\exp(-\omega_D^0) = 0.001$. Num. solution of a 3D system with concentration boundary conditions: grid points $N = 128$ $L = 120$; Init.: slightly perturbed droplet at the center. Time scales are given in units of K_2^{-1} .

FIGURE 5.4: Stationary protocells:

Quaternary mixture with free energy density following Eq. A.2, $i = S, D, N, W$ and common parameters for (a-d): $\chi_{DS} = 3$, $\chi_{NS} = -0.5$, $\chi_{WS} = 0.5$, $\chi_{DN} = 0$, $\chi_{DW} = 0$, $\chi_{NW} = 0$, $\omega_S^0 = 0$, $\omega_D^0 = 3$, $\omega_N^0 = 8$, $\omega_W^0 = 0$, $\nu_i/\nu_S = 1$, $k_B T = 1$, $\kappa_D = 1$. Composition-dependency of the reactions via $k_\alpha = K_\alpha \text{sig}[(\phi_D - 0.33)/\epsilon]$ with $\text{sig}(x) = (1 + \tanh(x))/2$, $\epsilon = 0.01$ (for $\alpha = 1, 2$), $\epsilon = -0.01$ (for $\alpha = 3$) $K_1/\exp(-\omega_N^0) = 0.3$, $K_2/\exp(-\omega_D^0) = 0.0088$. For (a): $\phi_D^\infty = 0.08$, $\phi_N^\infty = 0.15$, $\phi_W^\infty = 0.001$. For (b): $\phi_W^\infty = 0.001$. For (c): $\Delta\tilde{\mu} = 9$, $\bar{\psi} = 0.25$, $K_3/\exp(-\Delta\tilde{\mu}) = 0.008$.

FIGURE 5.5: Shape stability of protocells:

Same parameters as in FIG. 5.4 were chosen, except for all the parameters indicated on the axes.

FIGURE 5.6: Matter balance at the stationary state:

Same parameters as in FIG. 5.4 were chosen.

FIGURE 5.7: Heat flux in stationary protocells:

Quaternary mixture with free energy density following Eq. A.2, $i = S, D, N, W$ and common parameters for (a-d): $\chi_{DS} = 3, \chi_{NW} = 0, \omega_S^0 = 0, \chi_{DW} = 0, \phi_W^\infty = 0.0001, \nu_i/\nu_S = 1, k_B T = 1, \kappa_D = 1$, with identical reaction rates as in FIG. 5.4. For (a): $\chi_{NS} = 1, \chi_{WS} = 0, \chi_{DN} = -1, \omega_D^0 = -0.8, \omega_N^0 = 4, \omega_W^0 = 1, \phi_D^\infty = 0.11, \phi_N^\infty = 0.08$. For (b): $\chi_{NS} = -1, \chi_{WS} = 0.5, \chi_{DN} = 0, \omega_D^0 = -0.6, \omega_N^0 = 3, \omega_W^0 = 2.5, \phi_D^\infty = 0.1, \phi_N^\infty = 0.11$. For (c): $\chi_{NS} = 1, \chi_{WS} = 0, \chi_{DN} = -1, \omega_D^0 = -0.8, \omega_N^0 = 1, \omega_W^0 = 1, \phi_D^\infty = 0.12, \phi_N^\infty = 0.16$. For (d): $\chi_{NS} = -1, \chi_{WS} = 0.5, \chi_{DN} = 0, \omega_D^0 = -0.6, \omega_N^0 = 2, \omega_W^0 = 2.5, \phi_D^\infty = 0.12, \phi_N^\infty = 0.18$.

FIGURE 6.1: 3D vs. 2D - elongation and division:

Binary mixture with free energy density following Eq. 6.1, with $b = 1, \Phi_0^I = 1, \Phi_0^{II} = 0, \kappa = 1, \gamma = 1$. Numerical sim. with $N = 128$ grid points of a 3D (a) or 2D (b) system with size $L = 130$, and no-flux boundary conditions. Reaction rates for (a): $c^{II} = 0.00050, c^I = 0.00325, k^{I/II} = 0.00250$. Reaction rates for (b): $c^{II} = 0.0005, c^I = 0.00175, k^{I/II} = 0.00250$ (b), leading to the supersaturation $\epsilon = 0.2$ for both cases.

FIGURE 6.2: 2D vs. 3D - stable droplet radii and elongation instability:

Binary mixture with free energy density following Eq. 6.1, with $b = 1, \Phi_0^I = 1, \Phi_0^{II} = 0, \kappa = 1, c^I = 0.002, k^{I/II} = 0.0025, \gamma = 1$. For (a): $c^{II} = 0.0005$, leading to $\epsilon = 0.2$. For (b,c,d): varying c^{II} for the corresponding supersaturation values.

FIGURE 6.3: 2D vs. 3D - pinch-off stability:

Same parameters as in FIG. 6.2 were chosen.

FIGURE 6.4: Stability diagrams of chemically active droplets in 2D and 3D:

All parameters as in FIG. 6.2, except $c^{I/II}$. They are chosen to match the axes labels.

FIGURE 6.5: Mean curvature of the droplet interface:

A time point in the dynamics of a 2D system shown in FIG. 6.1, with $N = 256$.

FIGURE 6.6: Pinch-off in 2D systems via reactions at the interface:

Binary mixture with free energy density following Eq. 6.1, with $b = 1, \Phi_0^I = 1, \Phi_0^{II} = 0, \kappa = 1, \gamma = 1$. Numerical sim. with $N = 512$ grid points of a 3D (a) or 2D (b) system with size $L = 640$, and no-flux boundary condition. $c^{II} = 0.0014, c^I = 0.008, k^{I/II} = 0.01$, thus $\epsilon = 0.14$. Interface reactions: $c_{\text{int}} = 0.001, c_{\text{int}} = 0.003, c_{\text{int}} = 0.008$. Time scales are given in inverse units of $k^{I/II}$.

FIGURE B.1: Surface tension in multi-component mixtures:

Ternary mixture with free energy density following Eq. A.2, $i = S, A, B$ and parameters $\chi_{AS} = 1, \chi_{BS} = 3, \chi_{AB} = 0, \omega_i^0 = 0, \nu_i/\nu_S = 1, k_B T = 1, \Gamma = 100$. Num. simulation: 1D system with $N = 128$ grid points and system size $L = 1$.

Bibliography

- [1] Clifford P. Brangwynne, Christian R. Eckmann, David S. Courson, Agata Rybarska, Carsten Hoege, Jöbin Gharakhani, Frank Jülicher, and Anthony A. Hyman. Germline P Granules Are Liquid Droplets That Localize by Controlled Dissolution/Condensation. *Science*, 324(5935):1729–1732, June 2009.
- [2] Steven Boeynaems, Simon Alberti, Nicolas L. Fawzi, Tanja Mittag, Magdalini Polymenidou, Frederic Rousseau, Joost Schymkowitz, James Shorter, Benjamin Wolozin, Ludo Van Den Bosch, Peter Tompa, and Monika Fuxreiter. Protein Phase Separation: A New Phase in Cell Biology. *Trends in Cell Biology*, 28(6):420–435, June 2018.
- [3] Yongdae Shin and Clifford P. Brangwynne. Liquid phase condensation in cell physiology and disease. *Science*, 357(6357):eaaf4382, September 2017.
- [4] Salman F. Banani, Hyun O. Lee, Anthony A. Hyman, and Michael K. Rosen. Biomolecular condensates: Organizers of cellular biochemistry. *Nature Reviews Molecular Cell Biology*, 18(5):285–298, May 2017.
- [5] Simon Alberti, Amy Gladfelter, and Tanja Mittag. Considerations and Challenges in Studying Liquid-Liquid Phase Separation and Biomolecular Condensates. *Cell*, 176(3):419–434, January 2019.
- [6] Maria Hondele, Stephanie Heinrich, Paolo De Los Rios, and Karsten Weis. Membraneless organelles: Phasing out of equilibrium. *Emerging Topics in Life Sciences*, 4(3):343–354, December 2020.
- [7] Christoph A. Weber and Christoph Zechner. Drops in cells. *Physics Today*, 74(6):38–43, June 2021.
- [8] Terrell L. Hill. *Free Energy Transduction and Biochemical Cycle Kinetics*. Springer-Verlag, New York, 1989.
- [9] James D. Murray. *Mathematical Biology*. Interdisciplinary Applied Mathematics. Springer, New York, 3rd ed edition, 2002.
- [10] Yoshiki Kuramoto. *Chemical Oscillations, Waves, and Turbulence*, volume 19 of *Springer Series in Synergetics*. Springer Berlin Heidelberg, Berlin, Heidelberg, 1984.

- [11] Michael C. Cross and Pierre C. Hohenberg. Pattern formation outside of equilibrium. *Reviews of Modern Physics*, 65(3):851–1112, July 1993.
- [12] Pierre C. Hohenberg and Bertrand I. Halperin. Theory of dynamic critical phenomena. *Reviews of Modern Physics*, 49(3):435–479, July 1977.
- [13] Sam M. Allen and John W. Cahn. Ground state structures in ordered binary alloys with second neighbor interactions. *Acta Metallurgica*, 20(3):423–433, March 1972.
- [14] J. D. Gunton. The dynamics of random interfaces in phase transitions. *Journal of Statistical Physics*, 34(5-6):1019–1037, March 1984.
- [15] John W. Cahn and John E. Hilliard. Free Energy of a Nonuniform System. I. Interfacial Free Energy. *The Journal of Chemical Physics*, 28(2):258–267, February 1958.
- [16] Nicolas Rashevsky. Some Theoretical Aspects of the Biological Applications of Physics of Disperse Systems. *Physics*, 1(3):143–153, September 1931.
- [17] Nicolas Rashevsky. The Mechanism of Division of Small Liquid Systems Which Are the Seats of Physico-Chemical Reactions. *Physics*, 5(12):374–379, December 1934.
- [18] Sharon C. Glotzer, Dietrich Stauffer, and Naeem Jan. Monte Carlo simulations of phase separation in chemically reactive binary mixtures. *Physical Review Letters*, 72(26):4109–4112, June 1994.
- [19] David Zwicker, Anthony A. Hyman, and Frank Jülicher. Suppression of Ostwald ripening in active emulsions. *Physical Review E*, 92(1):012317, July 2015.
- [20] David Zwicker, Rabea Seyboldt, Christoph A. Weber, Anthony A. Hyman, and Frank Jülicher. Growth and division of active droplets provides a model for protocells. *Nature Physics*, 13(4):408–413, April 2017.
- [21] Pulat K. Khabibullaev and Abdulla A. Saidov. *Phase Separation in Soft Matter Physics*, volume 138 of *Springer Series in Solid-State Sciences*. Springer Berlin Heidelberg, Berlin, Heidelberg, 2003.
- [22] Samuel Safran. *Statistical Thermodynamics of Surfaces, Interfaces, and Membranes*. Frontiers in Physics. Westview Press, Boulder, Co, 2003.
- [23] Mehran Kardar. *Statistical Physics of Fields*. Cambridge University Press, Cambridge; New York, 2007.
- [24] John S. Rowlinson. Translation of J. D. van der Waals' "The thermodynamik theory of capillarity under the hypothesis of a continuous variation of density". *Journal of Statistical Physics*, 20(2):197–200, February 1979.

- [25] Pierre C. Hohenberg and Alexei P. Krekhov. An introduction to the Ginzburg–Landau theory of phase transitions and nonequilibrium patterns. *Physics Reports*, 572:1–42, April 2015.
- [26] Maurice L. Huggins. Solutions of Long Chain Compounds. *The Journal of Chemical Physics*, 9(5):440–440, May 1941.
- [27] Paul J. Flory. Thermodynamics of High Polymer Solutions. *The Journal of Chemical Physics*, 10(1):51–61, January 1942.
- [28] Nigel Goldenfeld. *Lectures on Phase Transitions and the Renormalization Group*. Number v. 85 in *Frontiers in Physics*. Addison-Wesley, Advanced Book Program, Reading, Mass, 1992.
- [29] William M. Jacobs and Daan Frenkel. Phase Transitions in Biological Systems with Many Components. *Biophysical Journal*, 112(4):683–691, February 2017.
- [30] Stefano Bo, Lars Hubatsch, Jonathan Bauermann, Christoph A. Weber, and Frank Jülicher. Stochastic dynamics of single molecules across phase boundaries. *Physical Review Research*, 3(4):043150, December 2021.
- [31] Sheng Mao, Derek Kuldinow, Mikko P. Haataja, and Andrej Košmrlj. Phase behavior and morphology of multicomponent liquid mixtures. *Soft Matter*, 15(6):1297–1311, 2019.
- [32] Charles M. Elliott and Zheng Songmu. On the Cahn-Hilliard equation. *Archive for Rational Mechanics and Analysis*, 96(4):339–357, December 1986.
- [33] K. Binder and D. Stauffer. Statistical theory of nucleation, condensation and coagulation. *Advances in Physics*, 25(4):343–396, July 1976.
- [34] Pierre Papon, Jacques Leblond, and Paul H. E. Meijer. *The Physics of Phase Transitions*. Advanced Texts in Physics. Springer Berlin Heidelberg, Berlin, Heidelberg, 2002.
- [35] Wilhelm Ostwald. Studien über die Bildung und Umwandlung fester Körper: 1. Abhandlung: Übersättigung und Überkaltung. *Zeitschrift für Physikalische Chemie*, 22U(1):289–330, February 1897.
- [36] Gerold Adam, Peter Läger, and Günther Stark. *Physikalische Chemie Und Biophysik*. Springer-Lehrbuch. Springer Berlin Heidelberg, Berlin, Heidelberg, 2009.
- [37] Robert A. Alberty. *Thermodynamics of Biochemical Reactions*. Wiley-Interscience, Hoboken, N.J, 2003.
- [38] Bernhard Palsson. *Systems Biology: Properties of Reconstructed Networks*. Cambridge University Press, Cambridge ; New York, 2006.

- [39] Francesco Avanzini, Emanuele Penocchio, Gianmaria Falasco, and Massimiliano Esposito. Nonequilibrium thermodynamics of non-ideal chemical reaction networks. *The Journal of Chemical Physics*, 154(9):094114, March 2021.
- [40] Frederick Reif. *Fundamentals of Statistical and Thermal Physics*. Waveland Press, Long Grove, Ill, reiss edition, 2009.
- [41] Crispin W. Gardiner. *Stochastic Methods: A Handbook for the Natural and Social Sciences*. Number 13 in Springer Series in Synergetics. Springer, Berlin Heidelberg, 4th ed edition, 2009.
- [42] Peter Hänggi, Peter Talkner, and Michal Borkovec. Reaction-rate theory: Fifty years after Kramers. *Reviews of Modern Physics*, 62(2):251–341, April 1990.
- [43] P. W. Atkins and Loretta Jones. *Chemical Principles: The Quest for Insight*. W.H. Freeman, New York, 5th ed edition, 2010.
- [44] Lew D. Landau, Jewgeni M. Lifshitz, and Lev P. Pitaevskij. *Statistical physics*. Number v. 5, 9 in Pergamon international library of science, technology, engineering, and social studies. Pergamon Press, Oxford ; New York, 1980.
- [45] Elsen Tjhung, Cesare Nardini, and Michael E. Cates. Cluster Phases and Bubbly Phase Separation in Active Fluids: Reversal of the Ostwald Process. *Physical Review X*, 8(3):031080, September 2018.
- [46] Suropriya Saha, Jaime Agudo-Canalejo, and Ramin Golestanian. Scalar Active Mixtures: The Nonreciprocal Cahn-Hilliard Model. *Physical Review X*, 10(4):041009, October 2020.
- [47] Bruce Alberts. *Essential Cell Biology*. Garland Science, New York, NY, fourth edition edition, 2013.
- [48] R. Dean Astumian. Thermodynamics and Kinetics of a Brownian Motor. *Science*, 276(5314):917–922, May 1997.
- [49] Frank Jülicher, Armand Ajdari, and Jacques Prost. Modeling molecular motors. *Reviews of Modern Physics*, 69(4):1269–1282, October 1997.
- [50] Omar Adame-Arana, Christoph A. Weber, Vasily Zaburdaev, Jacques Prost, and Frank Jülicher. Liquid Phase Separation Controlled by pH. *Biophysical Journal*, 119(8):1590–1605, October 2020.
- [51] Jonathan Bauermann, Sudarshana Laha, Patrick M. McCall, Frank Jülicher, and Christoph A. Weber. Chemical Kinetics and Mass Action in Coexisting Phases. *Arxiv (Preprint)*, December 2021.
- [52] Arren Bar-Even, Elad Noor, Yonatan Savir, Wolfram Liebermeister, Dan Davidi, Dan S. Tawfik, and Ron Milo. The Moderately Efficient Enzyme: Evolutionary and Physicochemical Trends Shaping Enzyme Parameters. *Biochemistry*, 50(21):4402–4410, May 2011.

- [53] Ron Milo and Rob Phillips. *Cell Biology by the Numbers*. Garland Science, Taylor & Francis Group, New York, NY, 2016.
- [54] Alan Mathison Turing. The chemical basis of morphogenesis. *Philosophical Transactions of the Royal Society of London. Series B, Biological Sciences*, 237(641):37–72, August 1952.
- [55] Roman Cherniha and Vasyly Davydovych. *Nonlinear Reaction-Diffusion Systems*, volume 2196 of *Lecture Notes in Mathematics*. Springer International Publishing, Cham, 2017.
- [56] G. Nicolis and I. Prigogine. *Self-Organization in Nonequilibrium Systems: From Dissipative Structures to Order through Fluctuations*. Wiley, New York, 1977.
- [57] Giacomo Bartolucci, Omar Adame-Arana, Xueping Zhao, and Christoph A. Weber. Controlling composition of coexisting phases via molecular transitions. *Biophysical Journal*, 120(21):4682–4697, November 2021.
- [58] Jan Kirschbaum and David Zwicker. Controlling biomolecular condensates via chemical reactions. *Journal of The Royal Society Interface*, 18(179):20210255, June 2021.
- [59] Dan Deviri and Samuel A. Safran. Physical theory of biological noise buffering by multicomponent phase separation. *Proceedings of the National Academy of Sciences*, 118(25):e2100099118, June 2021.
- [60] C. Vuik. Some historical notes about the Stefan problem. *NASA STI/Recon Technical Report N*, 93:32397, January 1993.
- [61] Ou-Yang Zhong-can and W. Helfrich. Instability and Deformation of a Spherical Vesicle by Pressure. *Physical Review Letters*, 59(21):2486–2488, November 1987.
- [62] Markus Deserno. *Notes on Differential Geometry*. 2004.
- [63] Aleksandr I. Oparin. Proiskhozhdenie zhizni (The origin of life). *Voennoe Izd. Ministerstva Obrony Sojuza SSR*, 1924.
- [64] John Burdon Sanderson Haldane. The origin of life. *Rationalist Annual*, 148:3–10, 1929.
- [65] Stéphane Tirard. J. B. S. Haldane and the origin of life. *Journal of Genetics*, 96(5):735–739, November 2017.
- [66] Jonathan Bauermann, Christoph A. Weber, and Frank Jülicher. Energy and Matter Supply for Active Droplets. *Arxiv (Preprint)*, March 2022.
- [67] Aleksandr I. Oparin, Alexander Pasyanskiy, and Alexander E. Braunschtein. *Origin of Life on the Earth*. Pergamon, 1959.
- [68] Sybren Ruurds de Groot and Peter Mazur. *Non-Equilibrium Thermodynamics*. Dover Publ, New York, NY, unabridged, corrected republication edition, 1984.

- [69] Jonathan Rodenfels, Karla M. Neugebauer, and Jonathon Howard. Heat Oscillations Driven by the Embryonic Cell Cycle Reveal the Energetic Costs of Signaling. *Developmental Cell*, 48(5):646–658.e6, March 2019.
- [70] J. J. Heijnen and J. P. Van Dijken. In search of a thermodynamic description of biomass yields for the chemotrophic growth of microorganisms. *Biotechnology and Bioengineering*, 39(8):833–858, April 1992.
- [71] J.-S. Liu, I. W. Marison, and U. von Stockar. Microbial growth by a net heat uptake: A calorimetric and thermodynamic study on acetotrophic methanogenesis by *Methanosarcina barkeri*. *Biotechnology and Bioengineering*, 75(2):170–180, October 2001.
- [72] Yuting I Li and Michael E Cates. Non-equilibrium phase separation with reactions: A canonical model and its behaviour. *Journal of Statistical Mechanics: Theory and Experiment*, 2020(5):053206, May 2020.
- [73] Christoph A Weber, David Zwicker, Frank Jülicher, and Chiu Fan Lee. Physics of active emulsions. *Reports on Progress in Physics*, 82(6):064601, June 2019.
- [74] Jens Eggers and Marco Antonio Fontelos. *Singularities: Formation, Structure, and Propagation*. Cambridge Texts in Applied Mathematics. Cambridge university press, Cambridge, 2015.
- [75] Ron Goldman. Curvature formulas for implicit curves and surfaces. *Computer Aided Geometric Design*, 22(7):632–658, October 2005.
- [76] Celina Love, Jan Steinkühler, David T. Gonzales, Naresh Yandrapalli, Tom Robinson, Rumiana Dimova, and T.-Y. Dora Tang. Reversible pH-Responsive Coacervate Formation in Lipid Vesicles Activates Dormant Enzymatic Reactions. *Angewandte Chemie International Edition*, 59(15):5950–5957, April 2020.
- [77] Karina K. Nakashima, Jochem F. Baaij, and Evan Spruijt. Reversible generation of coacervate droplets in an enzymatic network. *Soft Matter*, 14(3):361–367, 2018.
- [78] Wiggert J. Altenburg, N. Amy Yewdall, Daan F. M. Vervoort, Marleen H. M. E. van Stevendaal, Alexander F. Mason, and Jan C. M. van Hest. Programmed spatial organization of biomacromolecules into discrete, coacervate-based protocells. *Nature Communications*, 11(1):6282, December 2020.
- [79] Yufeng Chen, Min Yuan, Yanwen Zhang, Songyang Liu, Xiaohai Yang, Kemin Wang, and Jianbo Liu. Construction of coacervate-in-coacervate multi-compartment protocells for spatial organization of enzymatic reactions. *Chemical Science*, 11(32):8617–8625, 2020.

- [80] Björn Drobot, Juan M. Iglesias-Artola, Kristian Le Vay, Viktoria Mayr, Mrityunjoy Kar, Moritz Kreysing, Hannes Mutschler, and T-Y Dora Tang. Compartmentalised RNA catalysis in membrane-free coacervate protocells. *Nature Communications*, 9(1):3643, December 2018.
- [81] Shogo Koga, David S. Williams, Adam W. Perriman, and Stephen Mann. Peptide–nucleotide microdroplets as a step towards a membrane-free protocell model. *Nature Chemistry*, 3(9):720–724, September 2011.
- [82] Taisuke Kojima and Shuichi Takayama. Membraneless Compartmentalization Facilitates Enzymatic Cascade Reactions and Reduces Substrate Inhibition. *ACS Applied Materials & Interfaces*, 10(38):32782–32791, September 2018.
- [83] Wylie Stroberg and Santiago Schnell. Do Cellular Condensates Accelerate Biochemical Reactions? Lessons from Microdroplet Chemistry. *Biophysical Journal*, 115(1):3–8, July 2018.
- [84] Tony Hyman and Cliff Brangwynne. In Retrospect: The Origin of Life. *Nature*, 491(7425):524–525, November 2012.
- [85] Carsten Donau, Fabian Späth, Marilyne Sosson, Brigitte A. K. Kriebisch, Fabian Schnitter, Marta Tena-Solsona, Hyun-Seo Kang, Elia Salibi, Michael Sattler, Hannes Mutschler, and Job Boekhoven. Active coacervate droplets as a model for membraneless organelles and protocells. *Nature Communications*, 11(1):5167, December 2020.
- [86] Xingbo Yang, Matthias Heinemann, Jonathon Howard, Greg Huber, Srividya Iyer-Biswas, Guillaume Le Treut, Michael Lynch, Kristi L. Montooth, Daniel J. Needleman, Simone Pigolotti, Jonathan Rodenfels, Pierre Ronceray, Sadasivan Shankar, Iman Tavassoly, Shashi Thutupalli, Denis V. Titov, Jin Wang, and Peter J. Foster. Physical bioenergetics: Energy fluxes, budgets, and constraints in cells. *Proceedings of the National Academy of Sciences*, 118(26):e2026786118, June 2021.
- [87] Mehran Kardar, Giorgio Parisi, and Yi-Cheng Zhang. Dynamic Scaling of Growing Interfaces. *Physical Review Letters*, 56(9):889–892, March 1986.
- [88] Uri M. Ascher, Steven J. Ruuth, and Raymond J. Spiteri. Implicit-explicit Runge-Kutta methods for time-dependent partial differential equations. *Applied Numerical Mathematics*, 25(2-3):151–167, November 1997.

Selbständigkeitserklärung

Hiermit versichere ich, dass ich die vorliegende Arbeit ohne unzulässige Hilfe Dritter und ohne Benutzung anderer als der angegebenen Hilfsmittel angefertigt habe; die aus fremden Quellen direkt oder indirekt übernommenen Gedanken sind als solche kenntlich gemacht. Die Arbeit wurde bisher weder im Inland noch im Ausland in gleicher oder ähnlicher Form einer anderen Prüfungsbehörde vorgelegt. Die Arbeit wurde in Dresden am Max-Planck-Institut für Physik komplexer Systeme unter der Betreuung von Prof. Dr. Frank Jülicher angefertigt.

Jonathan Bauermann
Dresden, Mai 2022